

INFORMATION TO USERS

This manuscript has been reproduced from the microfilm master. UMI films the text directly from the original or copy submitted. Thus, some thesis and dissertation copies are in typewriter face, while others may be from any type of computer printer.

The quality of this reproduction is dependent upon the quality of the copy submitted. Broken or indistinct print, colored or poor quality illustrations and photographs, print bleedthrough, substandard margins, and improper alignment can adversely affect reproduction.

In the unlikely event that the author did not send UMI a complete manuscript and there are missing pages, these will be noted. Also, if unauthorized copyright material had to be removed, a note will indicate the deletion.

Oversize materials (e.g., maps, drawings, charts) are reproduced by sectioning the original, beginning at the upper left-hand corner and continuing from left to right in equal sections with small overlaps. Each original is also photographed in one exposure and is included in reduced form at the back of the book.

Photographs included in the original manuscript have been reproduced xerographically in this copy. Higher quality 6" x 9" black and white photographic prints are available for any photographs or illustrations appearing in this copy for an additional charge. Contact UMI directly to order.

UMI

A Bell & Howell Information Company
300 North Zeeb Road, Ann Arbor MI 48106-1346 USA
313/761-4700 800/521-0600

cuu duong than cong . com

NOTE TO USERS

The original manuscript received by UMI contains pages with indistinct and slanted print. Pages were microfilmed as received.

This reproduction is the best copy available

UMI

cuu duong than cong . com

PROPERTIES OF ZnO THIN FILMS GROWN ON R-PLANE Al₂O₃ BY
METAL ORGANIC CHEMICAL VAPOR DEPOSITION

by

CHANDRASEKHAR R. GORLA

A Dissertation submitted to the
Graduate School – New Brunswick
Rutgers, The State University of New Jersey
in partial fulfillment of the requirements

for the degree of

Doctor of Philosophy

Graduate Program in

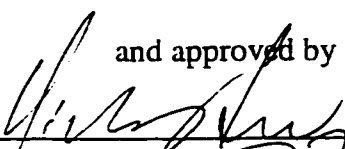
Materials Science and Engineering

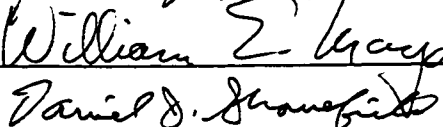
written under the direction of


Professor. Yicheng Lu

Professor. William E. Mayo

and approved by







New Brunswick, New Jersey

January, 1999

UMI Number: 9918320

**Copyright 1999 by
Gorla, Chandrasekhar Reddy**

All rights reserved.

**UMI Microform 9918320
Copyright 1999, by UMI Company. All rights reserved.**

**This microform edition is protected against unauthorized
copying under Title 17, United States Code.**

UMI
300 North Zeeb Road
Ann Arbor, MI 48103

© 1999

CHANDRASEKHAR R. GORLA

ALL RIGHTS RESERVED

ABSTRACT OF THE DISSERTATION

PROPERTIES OF EPITAXIAL ZnO THIN FILMS GROWN ON R-PLANE Al_2O_3 BY METAL ORGANIC CHEMICAL VAPOR DEPOSITION

By Chandrasekhar R. Gorla

Dissertation Directors

Professor Yicheng Lu

and

Professor William E. Mayo

High-quality ZnO films are desired for applications such as buffer layers for III-nitride growth, low-loss high-frequency surface acoustic wave devices, and UV lasers. In this project, ZnO thin films were epitaxially grown on R-plane sapphire substrates by metalorganic chemical vapor deposition at temperatures between 350 to 500 °C. The MOCVD reactor was redesigned by introducing separate injectors for DiEthyl Zinc and O_2 , which reduced the gas-phase reactions between the reactants. The orientation relationship between the ZnO films and the R-plane sapphire substrates was determined to be $(11\bar{2}0) \text{ ZnO} // (01\bar{1}2) \text{ Al}_2\text{O}_3$, and $[0001] \text{ ZnO} // [0\bar{1}11] \text{ Al}_2\text{O}_3$. The films had a smooth surface morphology without showing grain boundaries. The ZnO/ Al_2O_3 interface was investigated by high resolution transmission electron microscopy and it was found to be atomically sharp and semicoherent. The strain due to the 18.3% lattice mismatch along

the $[1\bar{1}00]$ direction of ZnO was relieved by a regular array of misfit dislocations. On average, the misfit dislocations had a separation of 1.4 nm, which corresponds to five $(1\bar{1}00)$ ZnO planes.

The surface acoustic wave (SAW) properties of the piezoelectric ZnO films were studied by fabricating SAW testing devices with the propagation direction parallel to the c-axis of ZnO. A maximum effective electromechanical coupling coefficient (k_{eff}^2) of 6 % was obtained for a 10 μm wavelength device fabricated on a 1.5 μm thick ZnO film, which is close to the k_{eff}^2 value for bulk single crystal ZnO, indicating the high quality of the film. The achieved results are promising for the fabrication of low-loss surface acoustic wave devices operating in the giga hertz (GHz) frequency range. The low temperature (11 K) photoluminescence spectra consisted of a sharp excitonic peak at 3.363 eV with a full width at half maximum of about 6 meV, which is comparable to the values for bulk ZnO. The anisotropic absorption characteristics for light polarized parallel to and perpendicular to the c-axis of ZnO were also evaluated.

In order to investigate the thermal stability of the as-grown ZnO films, annealing in an O_2+N_2 atmosphere was conducted. While the crystal quality of the films improved on high temperature annealing, ZnO reacted with Al_2O_3 forming a spinel (ZnAl_2O_4) layer at the interface. The thickness of the spinel layer formed was 15 nm and 35 nm on annealing the films for 30 min at 850°C and 1000°C respectively. Since this layer is confined to the interface between sapphire and ZnO, it is not expected to affect the use of ZnO as a buffer layer for the deposition of III-Nitrides. The kinetics of the solid state reaction between ZnO and Al_2O_3 was also investigated and the structures of the $\text{ZnO}/\text{ZnAl}_2\text{O}_4$ and $\text{ZnAl}_2\text{O}_4/\text{Al}_2\text{O}_3$ interfaces were evaluated. It was found that the

reaction was interface-controlled. It was determined that the $\text{ZnO}/\text{Al}_2\text{O}_3$ interface is stable if annealing is carried out below 750°C .

**Dedicated to
my parents
Indira and Eshwara Reddy**

ACKNOWLEDGEMENTS

I take this opportunity to express my sincere gratitude to my advisors, Prof. Yicheng Lu and Prof. William E. Mayo, for their invaluable guidance during my research work. They took an active interest in my professional development throughout my graduate studies and nurtured in me a deep interest in science and technology.

I greatly thank the members of my dissertation committee, Professor. D. J. Shanefield and Dr. Paul H. Shen, for devoting their time and expertise to reviewing the dissertation. In addition, I thank Dr. Shen and Dr. Wraback for carrying out the optical measurements, the results of which I am presenting in this thesis.

I would like to thank Professor Frederick Cosandey for constantly advising and helping me with various electron microscopy techniques, and Dr. Kalman for his help with regarding x-ray diffraction techniques.

My special thanks are due to Dr. Shaohua Liang, who has been of constant help in setting up and maintaining the MOCVD system and also for his advice through out my graduate work. I would also like to thank Nuri Emanetoglu and Dr. Liu for their assistance in fabricating and testing the surface acoustic wave devices.

TABLE OF CONTENTS

ABSTRACT	ii
DEDICATION	v
ACKNOWLEDGEMENTS	vi
TABLE OF CONTENTS	vii
LIST OF ILLUSTRATIONS	x
LIST OF TABLES	xiv
CHAPTER 1: INTRODUCTION	I
1.1 Motivation	I
1.2 Objectives	4
1.3 Dissertation Organization	5
CHAPTER 2: TECHNICAL BACKGROUND	7
2.1 Crystal Structure	7
2.2 Non-Stoichiometry and Resistivity	15
2.3 Optical Properties	19
2.4 Piezoelectricity and Surface Acoustic Wave Devices	22
2.4.1 Surface Acoustic Waves	24
2.4.2 Piezoelectric Materials	27
2.4.3 ZnO based Acoustic Devices	31
2.5 Thin Film Growth Techniques	35
2.6 Summary	39

CHAPTER 3: MOCVD GROWTH OF ZnO FILMS ON Al₂O₃	40
3.1 MOCVD Technology	40
3.2 MOCVD System	44
3.3 Substrate Selection	49
3.4 Growth Optimization	50
CHAPTER 4: STRUCTURAL CHARACTERIZATION	59
4.1 Epitaxial Relationships	59
4.2 Surface Morphology	63
4.3 Structure of the ZnO/R-Al ₂ O ₃ interface	67
CHAPTER 5: SURFACE ACOUSTIC WAVE AND OPTICAL PROPERTIES	69
5.1 Surface Acoustic Wave Devices	69
5.1.1 SAW Device Design	69
5.1.2 SAW Device Fabrication	72
5.1.3 SAW Device Characterization	74
5.2 Optical Properties	78
5.2.1 Introduction	78
5.2.2 Photoluminescence Characterization	84
5.2.3 Anisotropic Properties	86
CHAPTER 6: THERMAL STABILITY OF ZnO/R-Al₂O₃	90
6.1 Introduction to solid state reaction kinetics	92
6.2 Results and Discussion	101
6.2.1 Reaction Kinetics	101

6.2.2 Thermal Stability	120
CHAPTER 7: CONCLUSIONS	121
APPENDIX A: ELASTIC, PIEZOELECTRIC AND DIELECTRIC CONSTANTS OF ZnO	125
APPENDIX B: BASIC MICROWAVE CIRCUIT ANALYSIS AND S-PARAMETER MODEL	128
APPENDIX C: X-RAY ϕ -SCAN MEASUREMENTS	134
REFERENCES	141
CURRICULUM VITA	149

LIST OF ILLUSTRATIONS

Figure 2-1: Schematic diagrams of (a). Crystal structure of ZnO (Wurtzite) and (b). The projection of the wurtzite structure along the $[\bar{2}110]$ direction.	9
Figure 2-2: Schematic representation of three types of surfaces in ionic crystals.....	11
Figure 2-3: Interaction processes between the electrical, mechanical and thermal systems.	23
Figure 2-4: (a). Schematic representation of a Rayleigh wave (b). The variation with depth of the velocity components parallel to and perpendicular to the propagation direction.	25
Figure 2-5: (a). Coupling of an electrical signal to the acoustic wave through the use of Interdigital Transducers (b) Typical frequency response of a pass-band SAW filter.	28
Figure 2-6: Effect of ' kh ' on the SAW velocity in a layered medium (thin film on substrate).	33
Figure 3-1: A schematic diagram of the MOCVD system	45
Figure 3-2: A schematic diagram of the flow patterns in a Rotating-disc vertical flow MOCVD reactor.....	46
Figure 3-3: A schematic diagram of our MOCVD reactor. (a) Side view and (b) Top view.....	48
Figure 3-5: Effect of growth temperature on the x-ray $\theta-2\theta$ intensities of ZnO films grown on (100) Si.	51
Figure 3-6: SEM images of ZnO films grown on C-sapphire at (a) 585°C and (b) 400°C.....	52

Figure 3-7: SEM images of ZnO film on R-plane Al_2O_3 grown under different growth rates..	54
Figure 3-8: SEM images of other surface morphologies obtained under un-optimized growth conditions. (a) on C-plane Al_2O_3 , (b) on (100) Si, and (c) on R-plane Al_2O_3 .	55
Figure 3-9: TEM images of whiskers observed under spurious growth conditions.	57
Figure 4-1 X-ray θ - 2θ scans of ZnO grown on (a) R-plane Al_2O_3 and (b) C-plane sapphire.	60
Figure 4-2 (a). x-ray ϕ -scans of ZnO on R- Al_2O_3 (b). x-ray ϕ -scans of ZnO on C- Al_2O_3 .	61
Figure 4-3 (a). SEM image of ZnO on R- Al_2O_3 (b). SEM image of ZnO on C- Al_2O_3 .	65
Figure 4-4 The possible origin of the two types of grains seen in Figure 4-3(b).	66
Figure 4-5 (a). HR-TEM image of the interface between ZnO and R-sapphire. (b). Fourier-Filtered image corresponding to image in (a).	68
Figure 5-1: (a).Schematic diagram of a SAW filter fabricated on ZnO/R- Al_2O_3 (b). Design parameters of the IDT.	71
Figure 5-2: Schematic representation of the steps involved during the fabrication of the IDTs and the SAW devices..	73
Figure 5-3 (a). Frequency spectra of 10 μm SAW device on 1.5 μm ZnO film (b). Frequency spectra of 10 μm SAW device on 0.5 μm ZnO film	75
Figure 5-4 Schematic diagram of the valence band splitting due to spin-orbit coupling and crystal-field splitting in ZnO .	79

Figure 5-5	Reflectance spectra of ZnO at 1.6 K near the fundamental band gap	
	(a) $E \perp c$ and (b) $E // c$	82
Figure 5-6	(a). Room temperature Photoluminescence from ZnO/R-sapphire	
	(b). Photoluminescence from ZnO/R- Al_2O_3 at 11 K	85
Figure 5-7	Transmission and Reflectivity of ZnO on R-plane sapphire as a function of photon energy for light polarized parallel and perpendicular to the c-axis of the ZnO.....	87
Figure 5-8	(a). Schematic diagram showing the effect of the anisotropic transmission properties of ZnO on the polarization	
	(b) Polarization rotation as a function of photon energy for normal incident light linearly polarized at 45° with respect to the c-axis.	89
Figure 6-1:	Schematic representation of the variation of the chemical potential of A during the solid state reaction $A + B = AB$. (a). Diffusion controlled	
	(b). Interface controlled (c). Simultaneous interface and diffusion controlled	
	(d) rate control by rearrangement (relaxation) of A in B.	99
Figure 6-2:	Image of the spinel layer between ZnO and R-plane sapphire	103
Figure 6-3	(a). Electron Diffraction pattern of ZnO + spinel viewed along the $[0001]$ axis of ZnO	
	(b). Electron Diffraction pattern of ZnO + spinel viewed along the $[\bar{1}100]$ direction of ZnO.....	104
Figure 6-4.	Schematic diagrams of the spinel and sapphire crystals which have the epitaxial relationship 'A' given in Table 6-1	108
Figure 6-5.	Region near a grain boundary between two spinel grains.	110

Figure 6-6 Schematic representation of the mechanism involved during the solid state reaction between ZnO and Al ₂ O ₃	112
Figure 6-7. TEM image of two adjacent grains with different growth rates..	114
Figure 6-8: TEM images of two types of ZnO/Al ₂ ZnO ₄ interfaces observed.	117
Figure 6-9: High resolution TEM image of the Al ₂ ZnO ₄ /Al ₂ O ₃ interface.....	119

LIST OF TABLES

Table 2-1: Crystal structure, lattice constants and thermal expansion coefficients of ZnO, GaN, and Al ₂ O ₃	13
Table 4-1: Epitaxial relationships between ZnO and R- and C- sapphire	63
Table 5-1: Design parameters for the fabricated SAW filters	70
Table 5-2. SAW properties of the tested devices.....	76
Table 5-3: Comparison of the SAW properties of various material systems	77
Table 6-1: Observed epitaxial relationships between ZnAl ₂ O ₄ and ZnO/Al ₂ O ₃	106
Table 6-2: Volume changes occurring during the formation of ZnAl ₂ O ₄ at the ZnO/Al ₂ O ₃ interface.....	113

Chapter 1 : Introduction

1.1 Motivation

ZnO as a multifunctional material has been intensively investigated for many years in applications such as, surface acoustic wave (SAW)¹ and bulk acoustic wave (BAW)² devices (utilizing its piezoelectric properties) and, as transparent electrodes in solar cells³ and displays⁴ (as it can be made conducting by appropriate doping). Recently, there has been increasing interest in high quality epitaxial ZnO films for several new applications.

The III-Nitride family of direct wide-band-gap semiconducting materials (GaN, InGaN etc..) are of great technological importance as they can be used in optoelectronic devices (LEDs, lasers, detectors) which operate in the blue and UV regions of the optical spectrum. ZnO is a promising substrate material for GaN since it has small lattice mismatch with GaN. Hamdani et al., have grown high-quality GaN films on ZnO single crystal substrates by reactive MBE⁵. They reported that the structural properties of GaN thin films grown on ZnO were better compared to those grown on SiC and Sapphire. However, the cost of ZnO substrates is very high and large-area ZnO substrates are not commercially available at the present time. Hence, high-quality ZnO films grown on sapphire and other substrates are highly desirable. For the growth of III-Nitride films on a ZnO buffer layer, defects (such as threading dislocation) in the ZnO buffer layer will be transmitted into the growing nitride film; therefore, the defect density has to be minimized.

There has been an explosive development in wireless communication. The advance in communication technology would require a large bandwidth to deliver data, voice and images. The future communication systems, therefore, must operate at much higher frequencies (GHz range), correspondingly it will increasingly rely on research and development of materials and devices. Low-loss high-frequency filters are key devices for the transceiver modules of these communication systems. When high quality piezoelectric ZnO thin films with high electromechanical coupling coefficient are deposited on substrates possessing high acoustic velocity, such as sapphire or diamond, the structure can be used as high frequency and low loss surface acoustic wave (SAW) filters. Two important parameters for SAW devices are the insertion loss and the electromechanical coupling coefficient. Insertion loss is a combination of the losses at the interdigital transducer (IDT)/ZnO interface and the attenuation loss which occurs while the SAW travels from the input IDT to the receiving IDT. Attenuation loss can be caused by poor transfer of acoustic energy from one grain to another or between ZnO and the substrate (sapphire). Scattering can also occur at defects and grain boundaries, and by conversion of the SAW to bulk modes and other SAW modes at irregularities on the surface. The reduction in the electromechanical coupling coefficient is due to mis-aligned grains and to the presence of Inversion Domain Boundaries (IDB), which are adjoining grains with opposite polarity. As a result, good structural and epitaxial quality, and a sharp ZnO/sapphire interface are thus found to be essential for developing low loss SAW operating at high frequencies.

Another driving force for this research comes from the promising application of ZnO for UV lasers. A new type of ZnO based laser that generates UV light has been

reported recently. If such optically pumped experimental lasers can be turned into a practical device, it would find many important applications in this information age. The significant advantage of ZnO over the most popular wide band-gap material, GaN, is that ZnO can be grown on various substrates at about 500°C, hundreds of degrees lower than GaN. ZnO has a direct band gap of 3.37 eV at room temperature, and an exciton binding energy (E_b) of 60 meV which is 2.4 times the thermal energy at room temperature. The large E_b implies that electron-hole pairs are well bound even at room temperature. Hence, efficient radiative recombination is possible if the non-radiative recombination sites, such as point defects and dislocations, can be reduced and the structural quality of the film improved. Optically pumped stimulated emission has been observed at room temperature, but only at high excitation rates. Improvements in the stimulated emission characteristics will directly mirror the improvements made to the structure of ZnO films.

In all the above mentioned emerging application areas, there is a need for epitaxial ZnO films of good structural quality. To date, Pulsed Laser Ablation (PLD) and sputtering (DC, RF, Magnetron, ECR etc..) have been the popular growth techniques for growing ZnO films. PLD is a simple process, but due to the formation and incorporation of macroparticles into the film, it is not a very attractive growth technique for depositing high quality films. The sputtering systems have one main drawback due to the oxygen ion and neutral atom bombardment that generates point defects and local stresses, which degrades the film properties. Hence, the full potential of ZnO might not be achievable through sputtering.

1.2 Objectives

This thesis addresses the Metal-organic Chemical Vapor Deposition (MOCVD) of high-quality ZnO films grown on R-plane sapphire substrates. The structural properties will be studied in detail in order to correlate them to the piezoelectric and optical properties. The unique SAW properties and optical anisotropy in the ZnO/R-Al₂O₃ structure will be investigated for device applications.

Our first goal is to grow high-quality ZnO films on R-plane sapphire substrates by MOCVD and to evaluate their structural properties. In MOCVD, the sources, DiEthyl Zinc (DEZn) and O₂, diffuse through a boundary layer, adsorb on to the surface of the substrate, and then react with each other, forming ZnO while the organic groups are eliminated. The effect of energetic species is limited while thermodynamics plays a major role, and hence under optimum growth conditions, films of high structural quality are expected. These aspects of growth made us chose Metal Organic Chemical Vapor Deposition (MOCVD. DEZn and O₂ react even at room temperature, which makes it imperative to design the reactor such that pre-reaction in the gaseous phase does not occur. Conventional MOCVD reactor designs are not suitable for the present system, hence we will choose a more suitable design for the DEZn + O₂ system. The optimum growth conditions, epitaxial relationships between ZnO and R-sapphire, and the structure of the ZnO/Al₂O₃ interface will be evaluated.

Our second goal is to study and correlate the SAW and optical properties of ZnO/R-sapphire with the structural properties. Prototype SAW devices will be fabricated and the device parameters such as, center frequency, insertion loss and electromechanical coupling coefficient, will be evaluated. The optical properties of ZnO/R-sapphire, such as

the photo-luminescence (PL) spectra at room temperature and at 11 K, and the anisotropic absorption spectra of ZnO when light is polarized with $E//c$ -axis and with $E\perp c$ -axis of ZnO, will be evaluated. These properties will be correlated with the structural properties.

Our third goal is to study the thermal stability of ZnO/sapphire films. Annealing ZnO is one way of further improving the structural quality of the film. Unfortunately, at high temperatures, ZnO reacts with Al_2O_3 , forming a spinel, ZnAl_2O_4 . Hence an upper temperature limit for annealing has to be established which on one hand improves the crystal quality, while at the same time maintains the integrity of the ZnO/ Al_2O_3 interface. The kinetics of the solid state reaction between ZnO and Al_2O_3 , along with the structure of the ZnO/ ZnAl_2O_4 and $\text{ZnAl}_2\text{O}_4/\text{Al}_2\text{O}_3$ interfaces will be studied in detail, and the limits for thermal stability will be established.

1.3 Dissertation Organization

After establishing the motivation and goals for the present dissertation (Chapter 1), background information regarding the properties and corresponding applications of ZnO are reviewed in Chapter 2. The main topics covered are: crystal structure, non-stoichiometry and doping, optical properties, surface acoustic wave properties, and the basic growth techniques that can be used for depositing ZnO thin films. In Chapter 3 the MOCVD growth technique is reviewed, followed by our design and modifications of the MOCVD system in order to limit the gas phase reactions. In Chapter 4, we evaluate the optimum growth conditions, surface morphology, epitaxial relationships between ZnO and R-plane sapphire, and the interfacial structure between ZnO and the Al_2O_3 substrates. In Chapter 5, prototype SAW devices are fabricated and the device

characteristics (SAW velocity, electromechanical coupling coefficient, and insertion loss) are measured. The anisotropic absorption spectrum of the ZnO film, and the photoluminescence spectra at low temperature and at room temperature are also evaluated in this chapter. In Chapter 6, the thermal stability of the films and the kinetics of the solid state reaction between ZnO and R-plane sapphire are studied in more detail. An upper annealing temperature limit, below which the integrity of the ZnO/sapphire interface is maintained, is determined. Finally, conclusions and recommendations for future work are presented in Chapter 7.

Chapter 2 : Technical Background

ZnO as a multifunctional material has been extensively investigated in diverse applications such as, surface acoustic wave (SAW) and bulk acoustic wave (BAW) devices (utilizing its piezoelectric properties) and, as transparent electrodes in solar cells and displays (as it can be made conducting by appropriate doping), as a wave guide (transparent at visible wavelengths), as an acousto-optic Bragg reflector (combining the acoustic and optical properties), as a substrate for GaN (due to a low lattice mismatch), and as the active layer in UV lasers (3.37 eV bandgap and a 60 meV exciton binding energy). In this chapter the important properties of ZnO are reviewed with the emphasis on understanding the materials parameters which affect and control its properties.

2.1 Crystal Structure

ZnO is on the border between a semiconductor and an ionic material. It has a Wurtzite structure (hexagonal symmetry). Under most growth conditions, it displays an n-type semiconducting behavior. Even though it is tetrahedrally bonded, similar to other semiconductors, the bonds have a partial ionic character. It has been proposed that a formal charge distribution of $\text{Zn}^{1.2+}\text{O}^{1.2-}$ be assigned to ZnO.^{6,7} It belongs to the $P6_3mc$ space group with lattice parameters, $a = 0.324982$ nm and $c = 0.520661$ nm. The c/a ratio is 1.602, which is slightly less than the ideal value of 1.633 for the ideal hexagonal close packed structures. The Zn-O distance is 0.1992 nm parallel to the c -axis and 0.1973 nm in the other three directions of the tetrahedral arrangement of nearest neighbors. The lattice consists of two interpenetrating hexagonal-close-packed lattices, separated along

the c-axis by 0.3825 (fractional coordinates). While oxygen (by convention) occupies the $(0\ 0\ 0)$ and $(0.6667, 0.3333, 0.5)$ positions, zinc occupies the $(0, 0, 0.3825)$ and $(0.6667, 0.3333, 0.8825)$ positions^{8,9}. The crystal structure and its projection along the $[11\bar{2}0]$ direction are shown in Figure 2-1.

The close-packed (0001) planes are made up of two subplanes (A & a), each consisting of either the cationic (Zn) or the anionic (O) species. The crystal can be considered to have the stacking sequenceAaBbAaBb.... (Figure 2-1(b)) as compared toAaBbCcAaBbCc.... in diamond cubic (such as silicon) and sphalerite (such as GaAs) crystal structures. This results in marked differences in the properties between the (0001) and $(000\bar{1})$ planes, the former being Zn terminated and the later being O terminated. This structure does not possess a center of symmetry. These two characteristics are responsible for some of the most important properties of ZnO. The lack of inversion symmetry leads to ZnO being a piezoelectric material and the polarity of the c-axis causes the Zn-terminated and O-terminated planes to display vastly different properties.

For Si, a non-polar semiconductor with the diamond cubic structure, the close packed (111) planes have the lowest surface energy since only one bond per atom is broken when a surface is created. Other factors (mentioned below) play an important role in the case of ionic or partially ionic crystals such as NiO, ZnO, MgO, and Al_2O_3 .

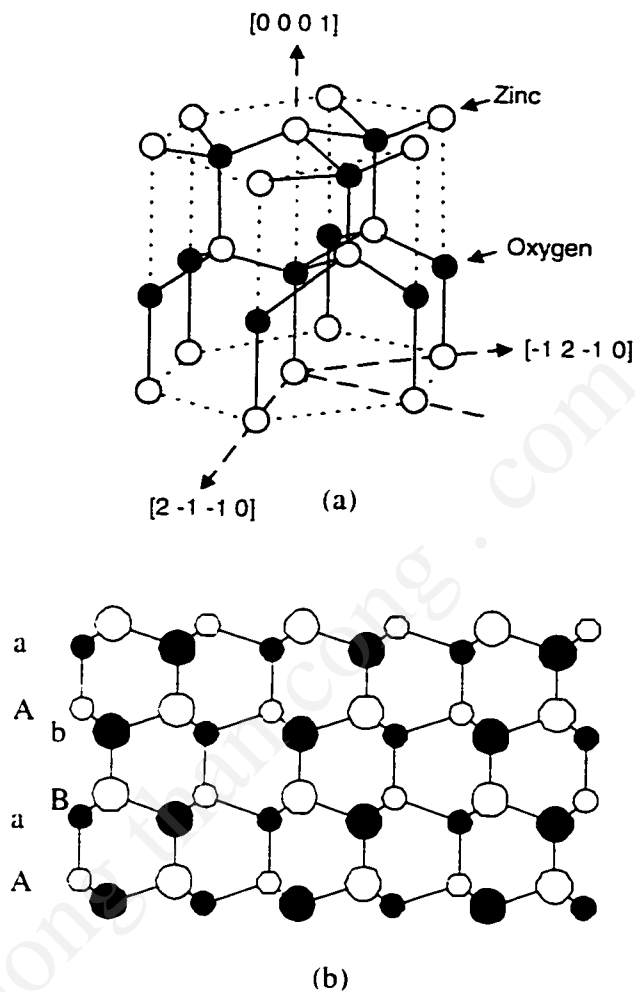


Figure 2-1 Schematic diagrams of (a). Crystal structure of ZnO (Wurtzite) and (b). The projection of the wurtzite structure along the $[2\bar{1}10]$ direction. It can be seen that the ZnO can be constructed by arranging close packed planes of Zn (A and B) and O (a and b) in the sequenceAaBbAaBb.....

There are three types of planes in ionic crystals (Figure 2-2). In a Type I surface, the cations and anions are in their stoichiometric ratio, resulting in a zero net charge on the surface. Type II surfaces occur when the crystal is cut in such a way that the subplanes have a repeat unit, B-A-B. An example for such a surface is the (0001) plane of Al_2O_3 . If the surface is cleaved between the B atomic layers, a B-A-B arrangement is generated resulting in a zero dipole moment. If cleaved in any other way, such as B-B-A or A-B-B, a net dipole is created. Type III surfaces, such as the (111) planes in NiO, and the (0001) planes in ZnO have alternating layers of cations and anions, which result in a dipole moment perpendicular to the surface. In the event that the surface has a net dipole moment, the surface energy diverges and is infinite^{10,11}, which in turn makes the surface unstable. The (0001) plane in ZnO is a polar plane and hence, with no reconstruction or passivation, should have the maximum surface energy amongst the low-index planes. This is in fact observed under most conditions during vapor phase growth. Crystals grown via the vapor phase method are usually needle shaped with a hexagonal cross-section. The crystals are elongated in the [0001] direction and the prismatic sides of the crystals are usually the $\{10\bar{1}0\}$ or $\{11\bar{2}0\}$ planes. This implies that the (0001) plane has the highest energy, as a result of which, the growth rate along the c-direction is the highest. Thus, it is very easy to obtain c-axis oriented films on almost any substrate, even under non-epitaxial conditions. Under certain growth conditions, whiskers have been observed to grow along the c-axis. This results in a rough surface morphology.

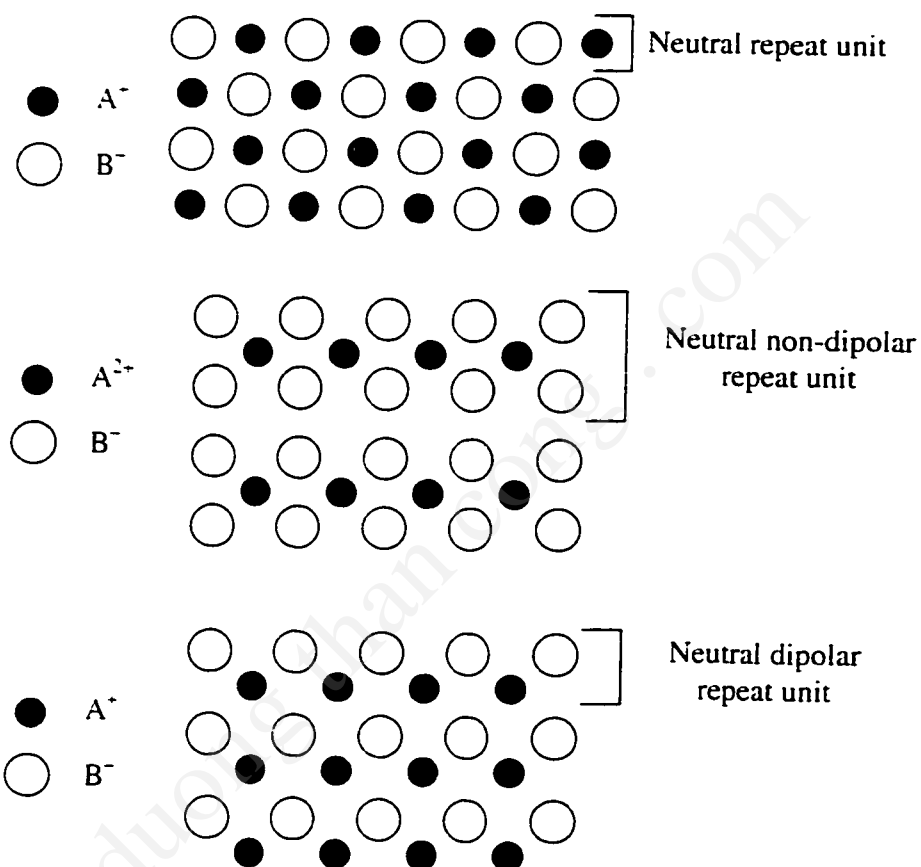


Figure 2-2: Schematic representation of three types of surfaces in ionic crystals.

(a) type I, (b) Type II and (c) Type III surfaces (see text for explanation).

Recent developments in III-V Nitride thin film technology have produced significant advances in high-performance optoelectronic devices operating in the blue-green range of the visible spectrum.^{12,13,14} GaN films are usually grown by Molecular Beam Epitaxy (MBE)^{15,16} or Metalorganic Chemical Vapor Deposition (MOCVD).¹⁷ To date, nonisomorphic substrates such as Al_2O_3 and 6H-SiC have been the most popular substrates for the growth of GaN films since Al_2O_3 is available in large sizes (75 mm diam.), while SiC has a very small lattice mismatch with GaN. However, when using 6H SiC as the substrate material, stacking mismatch boundaries (SMBs)¹⁸ and Double Positioning Boundaries (DPBs)¹⁹ arise due to steps on the substrate surface. GaN growth on Al_2O_3 is more complex because it has a different coordination of atoms than GaN as indicated by their different space groups. If the top surface of Al_2O_3 is nitrided, i.e. the first layer of nitrogen atoms (in GaN) attach in the same way to each uppermost Al atom of the substrate, there is a high probability that every step on the substrate also produces a SMB due to the position change of Al atoms in successive basal planes of the Al_2O_3 lattice. Hence, the use of isomorphic substrates such as ZnO has been suggested. Some of the material parameters of ZnO are given in table 1, along with those for GaN and Al_2O_3 . As indicated from the table, the lattice mismatch between GaN and ZnO is relatively small, which suggests that high quality films may be possible. ZnO has a 2.2 % lattice mismatch with GaN and is perfectly matched for $\text{In}_{0.22}\text{Ga}_{0.78}\text{N}$.²⁰

Table 2-1: Crystal structure, lattice constants and thermal expansion coefficients of ZnO, GaN, and Al₂O₃.

	ZnO	GaN	α -Al ₂ O ₃
Crystal Structure	Wurtzite	Wurtzite	Corundum
(space group)	(P ₆ 3mc)	(P ₆ 3mc)	(R $\bar{3}c$)
Lattice Constants	a = 0.3249	a = 0.3186	a = 0.4758
(nm)	c = 0.5206	c = 5.178	c = 1.299
Thermal Expansion	6.51 (\perp c)	5.59 (\perp c)	7.5 (\perp c)
Coefficient (10^{-6} /°K)	3.02 (\parallel c)	7.75 (\parallel c)	8.5 (\parallel c)

Recently, the role of a ZnO buffer layer (grown on C-Al₂O₃) on III-Nitride growth has been investigated,²¹ and ZnO/GaN heterostructures that can be used for fabrication of hybrid opto-electronic devices were successfully grown.²² InGaN grown by MOVPE on the Zn-terminated (0001) surface of ZnO substrates was shown to have a better structural quality than films grown on sapphire²⁰. X-ray diffraction line widths of InGaN grown on ZnO were 20 % smaller than that of films grown on sapphire. However, under reducing conditions (H₂ and NH₃) surface damage of the ZnO substrate was observed and hence care has to be taken to keep the substrate in a non reducing atmosphere until growth.

The effect of ZnO substrates on the properties of III-V nitrides grown by Reactive Molecular Beam Epitaxy⁵ has been studied. It has been found that the best quality GaN films obtained were the ones grown on the O-terminated (0001) surface. The characteristic yellow photoluminescence peak normally observed in GaN on Al₂O₃,

which is produced due to defects in the film, was absent or was very weak in the GaN films grown on ZnO.

As mentioned earlier, improvements in the crystalline quality of III-V nitrides have been observed when they are grown on ZnO substrates. At the present time, large area ZnO substrates are not available, and hence growth on ZnO substrates is not very cost-effective. Hence, the use of ZnO buffer layers on other substrates is a viable alternative as described below.

Hydride VPE grown GaN also showed considerable improvement when grown on sapphire with an RF sputtered ZnO buffer layer compared to a bare sapphire substrate.^{23,24,25,26} Sputtering of ZnO in an O₂ atmosphere instead of an Ar atmosphere was also shown to improve the quality of the GaN films. GaN films were grown on (0 0 0 1) (C-oriented) and (11 $\bar{2}$ 0) (A-oriented) sapphire substrates with ZnO buffer layers. It was suggested that thin ZnO buffer layers should be used since this will reduce the amount of Zn that diffuses into GaN. ZnO buffer layers have also been shown to improve the quality of GaN grown by liquid-target pulsed laser deposition on sapphire²⁷ and fused SiO₂.²⁸

ZnO buffer layers have been shown to be a promising candidate for III-Nitride epitaxy. But to further improve the quality of the nitride films, even higher quality ZnO buffer layers are required. Otherwise, there is a likelihood that defects (such as threading dislocations) in the ZnO buffer layers can grow into the deposited nitride film.

2.2 Non-stoichiometry and Resistivity

Binary or ternary oxides are usually non-stoichiometric compounds. For example, ZnO is obtained under most growth conditions with an excess of Zn, which can vary with the oxygen and/or Zn partial pressure. Since the ratio of Zn and O lattice sites is the same whether the compound is stoichiometric or not, any compositional variation implies a change in the concentration of point defects in one of the sublattices.

Note that in the following discussion, the defect notation S_M^x , of Kroger and Vink²⁹ is employed, wherein 'S' represents the species occupying the lattice site M . The superscript represents the charge of the species *relative to normal site occupancy* with a prime (') indicating a negative charge, and a dot representing a positive charge. For example Li_{Zn} represents a Li atom in the position which would normally be occupied by Zn, and V_O represents a vacancy in the oxygen sublattice. The subscript 'i' represents an interstitial position.

Excess Zn in ZnO i.e., $Zn_{1+\delta}O$, can be accommodated by forming zinc interstitials or by forming compensating oxygen vacancies. In the presence of Zn vapor, the process can take place according to



The interstitial Zn has a very low activation energy (0.04 eV)³⁰ for ionization, and acts as a donor resulting in



Alternately, we can write an equation wherein a pair of Zn and O lattice sites are added, but only the Zn site is filled resulting in an oxygen vacancy.



Metal excess can also be obtained by a loss of oxygen resulting in activated oxygen vacancies.

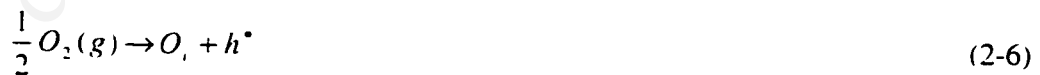


or by a loss of one pair of Zn and O lattice sites with Zn going into the interstitial site and vaporization of oxygen.



The activation energy for both Zn interstitials and O vacancies is 0.05 eV^{31,32} and hence there is some controversy over whether Zn_i (equations 2 and 5) or V_O (equations 3 and 4) are responsible for the observed conductivities in un-doped ZnO. While Harrison³³ assumed the existence of oxygen vacancies, Thomas³⁴ attributed the high conductivity of Zn-pretreated samples to Zn_i . Hagemark³⁵ discussed the coexistence of two different donors in the form of Zn interstitials and frozen-in oxygen vacancies. These concepts have been reviewed by Hirschwald et.al.³⁶

A metal deficit $Zn_{1-\delta}O$ composition can be accommodated by the formation of oxygen interstitials according to,



or by the formation of Zn vacancies according to,





It is seen that semiconducting oxides with metal excess contain free electrons, i.e., they are n-type, whereas a metal deficiency is associated with the presence of positive holes, i.e., with p-type behavior. While Zn deficiency is expected to produce p-type ZnO, it has not been achieved experimentally. This has been attributed to the requirement of extremely high pressures of O₂ necessary to produce an O-rich material. The n-type conductivity of ZnO heated at 1400–1700°C in oxygen pressures varying from 0–40 atm was found to decrease with increasing pressure, but never became p-type in the measured range.³⁷ An alternate method for introducing excess oxygen was studied by Nikitenko et al.^{38,39} They implanted oxygen ions into a ZnO crystal grown hydrothermally and doped with Li, followed by annealing under a protective film of gold, which effectively extracts Zn. Annealing at 670 K reduces but does not eliminate the damage caused by ion-implantation, and p-type doping was achieved under specific annealing treatments.

Another technique is to dope the sample with a mono-valent ion such as Li⁺ from Li₂O. Li is amphoteric i.e., it can act as a donor or as an acceptor. Li acts as a donor when it occupies the interstitial sites (*Li_i*), and acts as an acceptor when it occupies a lattice Zn site (*Li_{Zn}*). The addition of Li₂O to n-type ZnO results in



or



resulting in a decrease in the conductivity. Interstitial Li, introduced by heating a LiOH-covered crystal in Zn vapor, was found to increase the conductivity.⁴⁰ The conductivity

was observed to reach a maximum and then decrease as a function of time. The decrease was associated with the conversion of interstitial Li to substitutional Li, according to



Thus it was concluded that occupation of the substitutional sites is the equilibrium position of Li ions. Consequently, during diffusion, sufficient time has to be given for equilibration of the Li ions.

The typical range of resistivities observed are (a) 1-100 Ω -cm for undoped n-type ZnO, (b) 10^6 Ω -cm for Li doped ZnO in an oxygen atmosphere, and (c) 10^{11} Ω -cm for O ion-implanted Li-doped ZnO. Even though the resistivity is high in (c), structural damage is introduced, which is deleterious for other properties such as SAW velocity, SAW attenuation (eg., in Ar^+ implantated $LiNbO_3$)⁴¹ and optical properties. Alternate doping schemes, such as N incorporation by the addition of NH_3 during growth,⁴² have been used to produce p-type films of resistivity in the 100 Ω -cm range.

Higher n-conductivities are also required for some applications, for example as a transparent conductor in solar cells and flat panel display technology. In order to achieve higher conductivities in the range of $10^6 - 10^8$ (Ω -cm)⁻¹, ZnO is doped with a trivalent metal (Al, In, Ga etc.). The reactions involving incorporation of the dopant (In form In_2O_3) can be written as



and



There are probably other reactions which occur, such as



Thus, the resistivity (or conductivity) of ZnO can be controlled over a very wide range by doping with appropriate dopants, thus permitting use in applications requiring either insulating properties (piezoelectric devices) or conductive properties (transparent conductor). Limited success has been achieved in p-type doping. With further improvements the use of ZnO in new applications which require p-n junctions (such as bipolar junction transistors and UV photodetector) should be possible.

2.3 Optical Properties

The refractive index of ZnO varies (with wavelength below the band gap) between 1.96 and 2.1⁴³ and it has a direct band gap (≈ 3.37 eV at room temperature) at the Γ position of the Brillouin Zone. The conduction band is predominantly *s* like, and the valence band is *p* like (6 fold degenerate). Details of the band splitting, free excitons and bound excitons in ZnO are given in Chapter 5. In brief, the valence band splits into three doubly degenerate sub-bands (called A, B and C bands). Free excitons with a binding energy of 63 meV, 50 meV and 49 meV are associated with the A, B and C valence bands respectively. Optical anisotropy exists in the excitation of these excitons by light polarized either parallel to or perpendicular to the *c*-axis of ZnO. The C-excitons are preferentially excited when $\mathbf{E} \parallel \text{c-axis}$ and the A and B excitons are preferentially excited when $\mathbf{E} \perp \text{c-axis}$. The high binding energy of the excitons and the optical anisotropy can result in many useful applications.

Due to the large band gap of ZnO and its transparency at visible wave lengths, and a large refractive index, it can be used as an optical wave-guide.⁴⁴ Guided Optical Wave (GOW) losses of 0.55 dB/cm (for a TE_0 mode of a 0.6328 μm He-Ne laser) in

sputtered films on sapphire,⁴⁴ and as low as 0.01 – 0.03 dB/cm for sputtered ZnO films on oxidized silicon followed by laser annealing⁴⁵ have been reported. The material parameters which contribute the most to the propagation loss have been identified as the grain boundaries between adjacent ZnO grains and the interface between ZnO and the substrate.⁴⁶ Hence, ZnO films with a high structural quality and a sharp film/substrate interface are required to fabricate low loss optical wave-guides.

Acoustooptic Bragg Modulators⁴⁷ are used as tunable filters and switches for wavelength division multiplexing, spectrum analyzers, collinear and noncollinear modulators, convolvers, and correlators. These Modulators, which reflect light at a so called "thick" grating caused by acoustical wavefronts, can be fabricated utilizing the piezoelectric properties of ZnO (to generate the surface acoustic wave) combined with its optical waveguiding ability.⁴⁸ In certain cases where its refractive index is not suitable for integration with glass fibers, ZnO can be deposited onto an SiO₂ waveguide, and used for generating surface acoustic waves in the waveguide structure.⁴⁹ Design and analysis of a ZnO/GaAs/AlGaAs based structure has also been carried out recently.⁵⁰

Another type of optical modulator, an optically addressed normal incidence ultraviolet light modulator, which exploits the optical anisotropy inherent in ZnO epitaxially grown on R-plane sapphire has been demonstrated recently.⁵¹ An ultrafast dynamic polarization rotation of $\sim 12^\circ$ created by anisotropic bleaching of the anisotropic absorption, and concomitant ultrafast polarization rotation near the lowest exciton resonances produced by femtosecond ultraviolet pulses is employed in attaining a contrast ratio of 70:1.

Some of the more recent advances in ZnO film quality has led to stimulated emission in the UV range. Optically pumped lasing from vapor phase grown platelets at 2 K was observed by Reynolds et. al.⁵² Room temperature optically pumped stimulated emission (at 3.18 eV) from microwave plasma-enhanced Molecular Beam Epitaxially grown^{53,54} and laser assisted MBE grown⁵⁵ ZnO films on sapphire substrates has been observed recently. Lasing persisted up to a temperature of 550 K.⁵⁴ The 60 meV A-exciton binding energy in ZnO, which corresponds to 2.4 times the effective thermal energy at room temperature, results in the persistence of stimulated emission even above room temperature. By reducing the dimensions of the active layer, the exciton binding energy and the oscillator strength can be greatly enhanced, which should further improve the lasing characteristics. The energy position of the stimulated emission was in accordance with that expected from an inelastic collision between excitons.⁵⁶ The result of such a collision is an exciton in a higher state ($n = 2, 3, 4, \dots, \infty$), and a photon (P_n) with energy given by

$$P_n = E_{ex} - E_{ex}^n \left(1 - \frac{1}{n^2} \right) - \frac{3}{2} kT \quad (2-16)$$

where P_n is the photon energy, E_{ex} is the free exciton emission energy, E_{ex}^n is the binding energy of the exciton, n is the quantum number of the envelope function, and kT is the thermal energy. While the above mentioned studies have shown the feasibility of stimulated emission from ZnO, further improvements in the quality of the films, realization of p-type ZnO layers, and quantum structures with ZnO active layers still have to be accomplished in order to obtain laser diodes.

2.4 Piezoelectricity and Surface Acoustic Wave devices

Piezoelectricity is a linear interaction between electrical and mechanical systems. The direct piezoelectric effect involves the production of an electric polarization by mechanical strains in the system. Closely related to it is the converse effect, whereby a crystal becomes strained when an electric field is applied. Interaction processes possible between any two of the three systems - electrical, mechanical, and thermal - are illustrated in Figure 2-3.⁵⁷ The constitutive equations relating the electric and mechanical variables are:

$$T_{ij} = c_{ijkl} S_{kl} - e_{kij} E_k \quad (2-17)$$

$$D_i = e_{ikl} S_{kl} + \epsilon_{ik} E_k \quad (2-18)$$

where T_{ij} is the stress tensor (Nm^{-2}),

S_{kl} is the strain tensor,

c_{ijkl} is the stiffness tensor (Nm^{-2}),

e_{kij} is the piezoelectric coefficient tensor (Cm^{-2})

ϵ_{ik} is the permittivity or dielectric constant tensor (Fm^{-1})

D_i is the electric displacement (Cm^{-2}), and

E_k is the electric field intensity (Vm^{-1})

Centrosymmetric classes are always inactive in piezoelectricity. Out of the 32 point groups, only crystals belonging to 20 of them can show piezoelectricity. 6mm, the point group of wurtzite (ZnO), is one of them. Crystals with the diamond cubic structure (Si, diamond, Ge) do not show piezoelectricity.

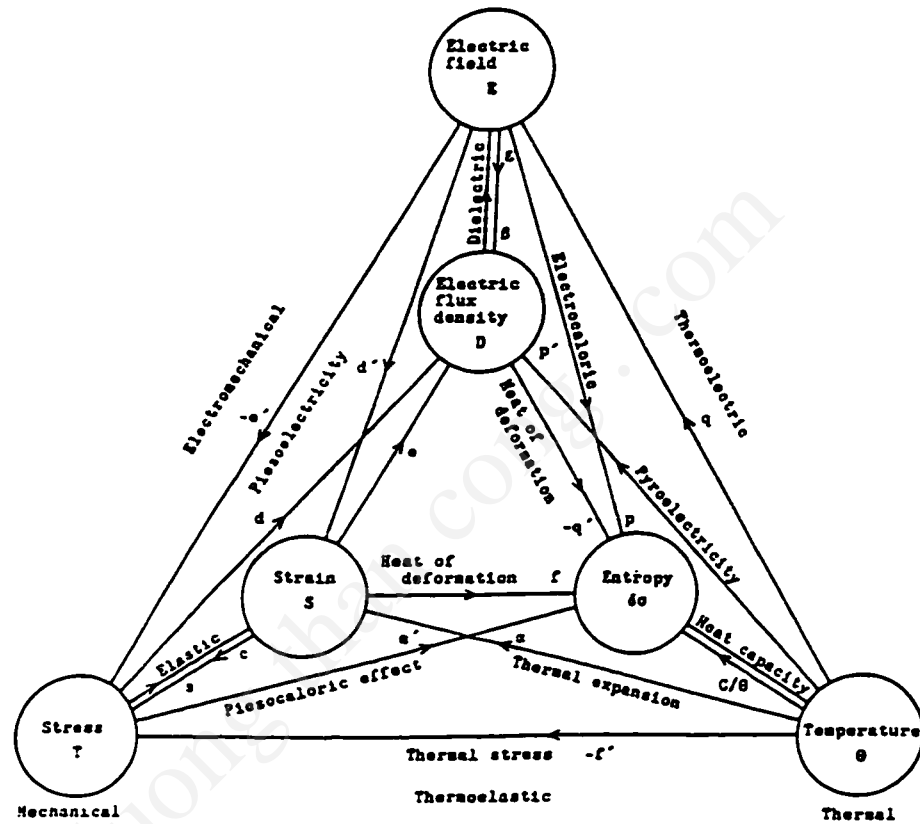


Figure 2-3: Interaction processes between the electrical, mechanical and thermal systems.[57]

The electromechanical coupling in piezoelectric materials leads to a form of Newton's equation

$$\rho \frac{\partial^2 u}{\partial t^2} = c \frac{\partial^2 u}{\partial x^2} + e \frac{\partial E}{\partial x} \quad (2-19)$$

where u is the material displacement at position x and at time t , E is the electric field and e is the piezoelectric coefficient. Thus an alternating field will generate an elastic wave of the same frequency and, conversely, the elastic wave will give rise to a varying polarization.

2.4.1 Surface Acoustic Waves

Acoustic waves are of two main types: bulk acoustic waves, which travel through the bulk of the specimen, and surface acoustic waves, which travel on a free surface with a limited penetration depth into the specimen.

Surface Elastic Waves,⁵⁸ were first discovered by Lord Rayleigh,⁵⁹ while studying the properties of seismic waves which propagate along the crust of the earth. The particles in the path of a Rayleigh wave have an elliptical motion in the sagittal plane (plane which includes the propagation direction and the surface normal), which is shown in Figure 2-4(a). The velocity of the particles in the mutually perpendicular directions is also shown in Figure 2-4(b). The Rayleigh wave motion reverses its sense at depths greater than approximately one-fifth of a wave length, and the wave is limited to a depth of the order of one to two wavelengths. There are other modes of waves – leaky SAWs, surface-skimming bulk waves (SSBW) – which are not true surface waves and hence are known as pseudo surface waves.

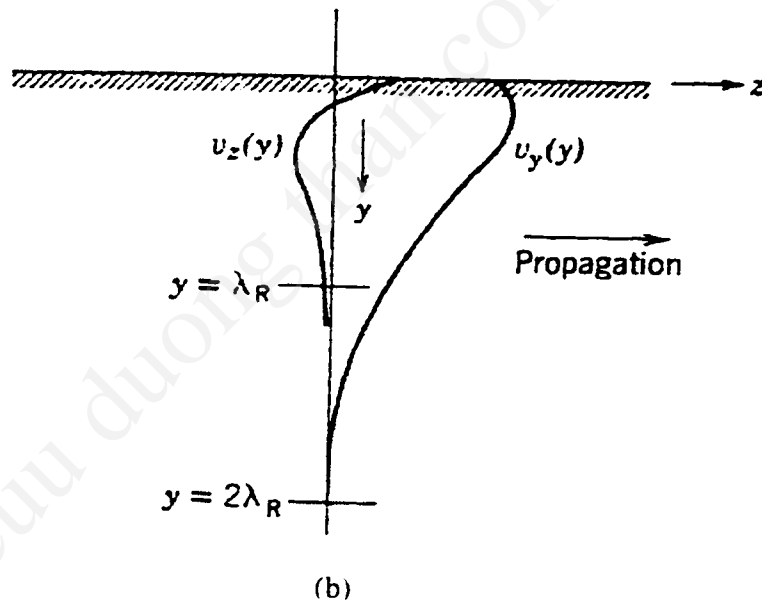
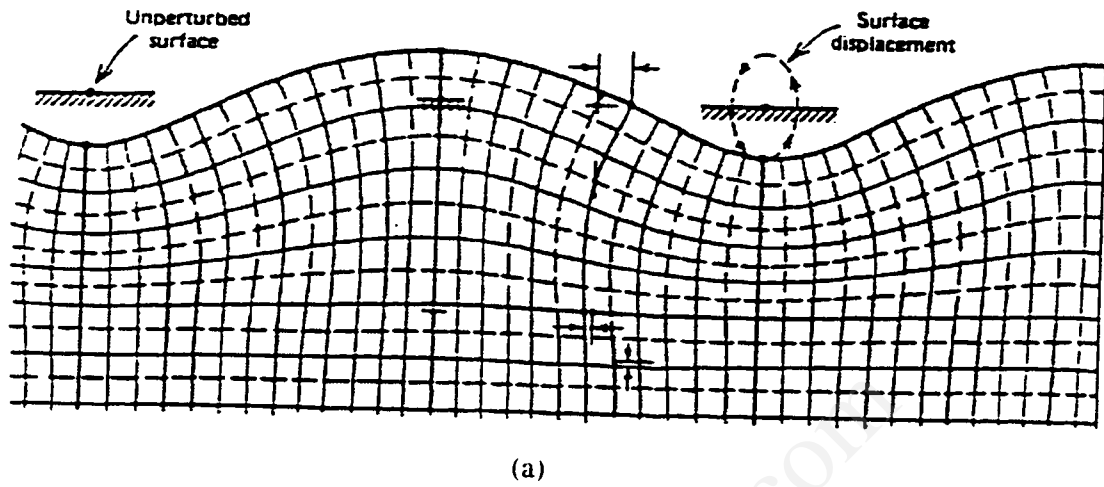


Figure 2-4: (a). Schematic representation of a Rayleigh wave.
 (b). The variation with depth of the velocity components parallel to and perpendicular to the propagation direction. [60]

Surface acoustic waves have one clear advantage over bulk waves in device applications: they are always accessible as they travel along the surface. This geometrical freedom for having access to the surface wave – for sampling it, modifying it, interacting with it at the surface – permits one to realize a wider range of devices than with bulk waves. This accessibility means that one can generate and detect surface waves with surface structures, and with the development of planar processing techniques, a wide variety of devices can be fabricated. The accessibility also means that any physical process or signal (mass loading by absorption of gases, changes in the conductivity of the surface, electromagnetic fields etc..) which interacts with and/or modifies the surface can affect the propagation velocity and properties of the surface wave. Hence surface acoustic wave devices can be used to detect and quantify the interacting physical process, for example as chemical sensors.

The reason for the large interest in acoustic devices for electronic applications is due to the low velocity of acoustic waves (10^5 times smaller) compared to electromagnetic waves (most interested in Microwaves - frequencies between 300 MHz and 300 GHz, with a corresponding electrical wave length between 1 m and 1 mm respectively). Acoustic wave devices are extremely useful in microwave signal processing because by converting the electromagnetic waves into acoustic waves (which have a much smaller wave length), they can be manipulated and processed in devices with manageable dimensions. Typical applications include delay lines in signal processing, filters, resonators etc.

Coupling between surface waves and electrical signals is usually achieved by metal interdigital transducers (IDT). In their simplest form, IDTs consist of many parallel

fingers alternately connected to opposite electrodes to which the signal is applied (Figure 2-5(a)). The wavelength of the generated elastic wave is equal to the transducer periodicity p , defined as the center to center distance between two consecutive fingers of one comb of the IDT. Therefore the synchronous frequency of a given SAW device on a given plate material is $f = v/p$, where v is the SAW velocity. A typical SAW filter consists of two sets of IDTs. The input electrical signal is coupled to a surface acoustic wave in the ZnO film through one IDT. The surface wave after reaching the second IDT is transformed back into an electrical signal. The SAW filter acts as a band-pass filter, with a typical response as shown in Figure 2-5(b). The response function can be approximately represented by

$$(\sin x / x)^2$$

where $x = N\pi(f-f_c)/f_c$ and N is the number of electrode pairs.

2.4.2 Piezoelectric Materials

Three of the most important parameters which determine the applicability of a piezoelectric material in acoustic devices are the Electromechanical Coupling Coefficient (k), the Temperature Coefficient of Frequency (TCF), and the attenuation of acoustic waves or loss mechanisms.

(i) Electromechanical Coupling Coefficient (k): Three definitions that are normally used for k are given below.

a. Mason⁶¹ defined the electromechanical coupling coefficient as

$$k^2 = \frac{\text{stored mechanical energy}}{\text{supplied electrical energy}} \quad (2-20)$$

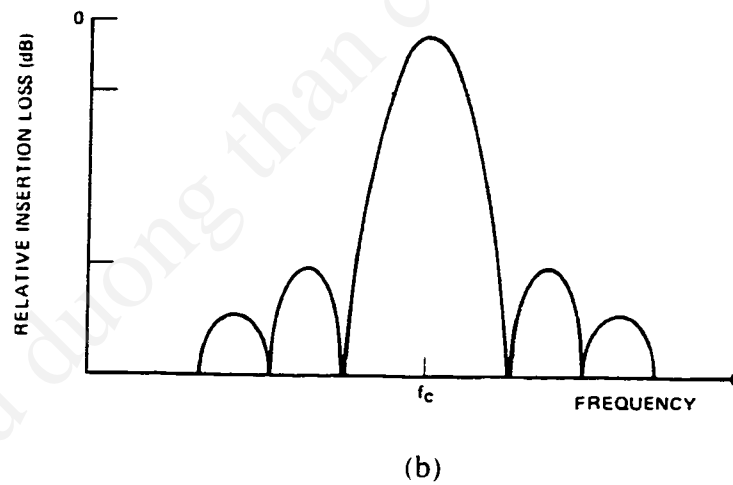
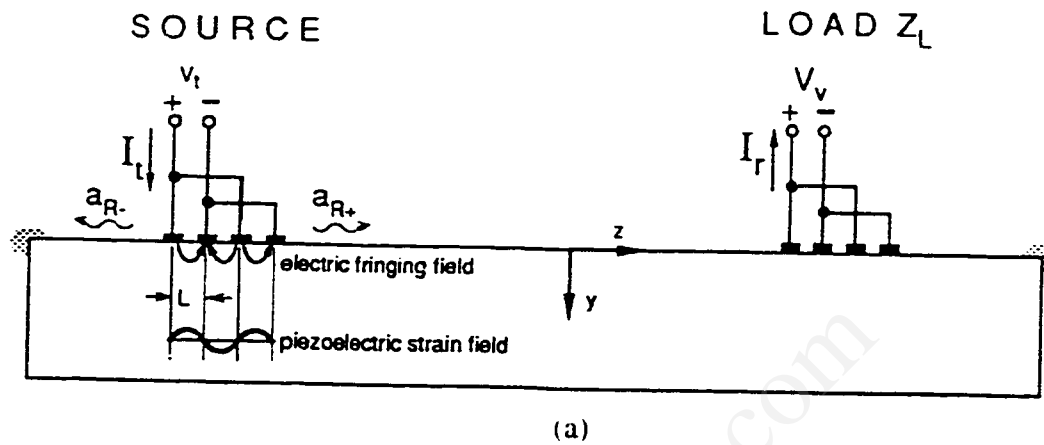


Figure 2-5: (a). Coupling of an electrical signal to the acoustic wave through the use of Interdigital Transducers [60].
(b) Typical frequency response of a pass-band SAW filter.

A similar definition, but one which is more easily applicable to practical devices has been adopted by the IEEE.⁶²

- b. As a consequence of equations 2-17 to 2-19, the wave velocity depends on the elastic, piezoelectric and dielectric properties. The medium behaves as if it were more stiff because of the additional potential energy resulting from the piezoelectric coupling, and the velocities are higher than without the coupling as a result of the "piezoelectric stiffening". The effective elastic stiffness is increased to the value

$$c_{stiffened} = c(1 + k^2) \quad (2-21)$$

with

$$k^2 = \frac{e^2}{c\epsilon}$$

where the components of e , c , and ϵ used depend on the propagation direction. The term k , called the electromechanical coupling coefficient, is a convenient measure of the strength of piezoelectric coupling.

- c. The electromechanical coupling coefficient defined above is a material constant. For Surface Acoustic Wave devices, k is not always given on a theoretical basis. It is given semi-empirically⁶³ by determining the velocity (v_s) of the surface wave when the surface of the film between the two interdigital transducers (IDTs) is shorted by a metallic coating, and the velocity (v_b) in a bare device (no shorting). Then the effective coupling coefficient (k_{eff}) is given by

$$k_{eff}^2 = 2(v_b - v_s)/v_b$$

- d. Another method for evaluating the effective electromechanical coefficient of a transducer is based on calculating the Radiation Conductance of the IDT and

Coupling-of Modes (COM) simulations.^{64,65} This technique takes into account the effect of energy transfer and conversion at the input and output IDTs in addition to the material properties of the film and substrate.

(ii). Temperature Coefficient of Frequency (TCF): As the elastic, piezoelectric and dielectric constants of a material vary with temperature, the frequency response of practical resonators and filters also changes with temperature. For practical devices, the variation in frequency with temperature, which is given by the TCF, should be as low as possible.

(iii). Attenuation: Surface wave attenuation in a crystal may result due to a number of different causes: lattice attenuation due to the intrinsic loss (phonons) in the crystal; scattering of energy and mode conversion at surface cracks, surface roughness, and elastic discontinuities at grain boundaries; and electronic loss in a conducting or semiconducting crystal. These effects contribute to the "Insertion Loss" in practical devices.

The most commonly used piezoelectric materials for SAW devices are LiNbO_3 , LiTaO_3 , Quartz and ZnO . The ST cut of Quartz has a very low TCF, but has a very small electromechanical coupling coefficient. There are other cuts with $0.3\% k^2$, but unfortunately their TCF is not zero. Hence the ST cut is almost exclusively used in quartz devices. LiNbO_3 and LiTaO_3 crystals have a higher k^2 , but have inferior temperature characteristics. In addition, the attenuation constants are high for these cuts as the wave mode is leaky SAW or surface-skimming bulk waves. (SSBW). Hence these substrates

are not suitable for low-loss SAW filters as they have substantial propagation losses (attenuation).

While ZnO substrates are not widely available, c-axis oriented ZnO films can be deposited onto almost any substrate, which makes it the preferred piezoelectric layer wherever integration with other devices is necessary. The feasibility of using ZnO films deposited on GaAs⁶⁶ and InP⁶⁷ substrates for SAW device applications have been investigated recently. Such devices will create the opportunity for integrating SAW devices with GaAs electronics or with InP based optical devices. The SAW properties of ZnO films are examined in greater detail in the next section.

2.4.3 ZnO based Acoustic Devices

Piezoelectric thin films of ZnO were first used as the transducer material for driving bulk acoustic waves into any propagating medium.^{68,69} The reason for the increasing popularity of ZnO films were that it had a high coupling coefficient and that c-axis oriented films could easily be deposited. Bulk acoustic wave devices are typically used as oscillators, filters and delay lines.

Thin Film Bulk Acoustic Wave resonators were later developed due to the advantages it provided in terms of monolithic integration with semiconductor devices leading to small size and low cost, and because they could be used up to 2 GHz frequencies.^{2,70,71} The basic structure involves ZnO deposition onto a metal coated membrane (Si etc.,) that has been formed by anisotropic etching of the substrate.

SAW devices with operating frequencies in the 1 – 4 GHz range are required for wireless communications in the present and the future. The inter-electrode spacing for a SAW device operating at 2.5 GHz is close to 0.5 μm (SAW velocity is close to 2600

m/sec). This results in a line width of $0.25\text{ }\mu\text{m}$, which is close to the fabrication limit for ZnO devices. Hence the SAW velocity has to be increased in order to obtain higher operating frequencies. This is possible by depositing ZnO on to a substrate with a much higher SAW velocity.

Rayleigh wave velocity on a layered structure i.e. a piezoelectric film on a substrate, is modified due to the different elastic stiffness constants of the film and substrate. For films with thickness less than the wavelength of the Rayleigh wave, a portion of the wave penetrates or is transferred into the substrate and travels along the substrate surface, thus affecting the velocity of the Rayleigh wave.⁷² If the substrate has a higher shear wave velocity (higher stiffness), the coupling increases the velocity of the Rayleigh-like wave is increased in contrast to a decrease if the substrate has a lower shear wave velocity. The phase velocity of the first Rayleigh-like mode is equal to the Rayleigh velocity of the substrate for small ' kh ' (i.e. either small ZnO thickness or large λ). As ' kh ' increases, the phase velocity continues to decrease (Figure 2-6), until for layer thickness large compared to the wavelength ($kh \gg 1$), it becomes asymptotic to the Rayleigh velocity appropriate to a free surface of the layer material i.e. ZnO. Consequently, for high frequency SAW filters, the thickness of the ZnO films has to be as small as possible. But the efficiency of electromechanical coupling between the input electrical signal and the generated surface acoustic wave decreases with decreasing ZnO film thickness (volume of piezoelectric material decreases). For a high-frequency and low-loss SAW device design, a trade-off between operating frequency and coupling coefficient has to be taken into account.

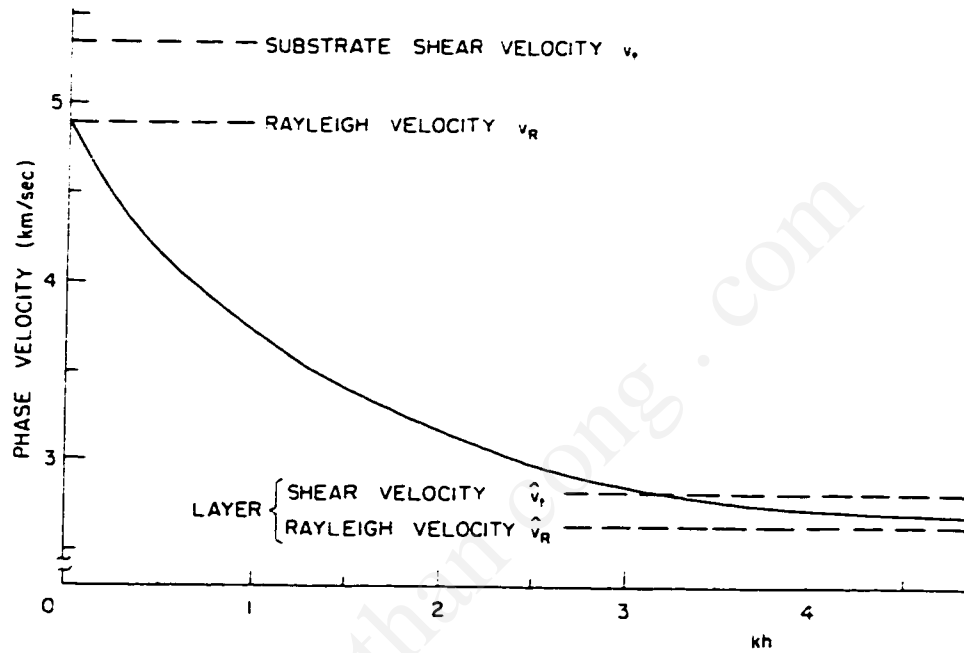


Figure 2-6: Effect of ' kh ' on the SAW velocity in a layered medium (thin film on substrate). ' k ' is the wave number and ' h ' is the film thickness. [72]

The electromechanical coupling coefficient for the (0001) plane of ZnO is much lower than that of the $(11\bar{2}0)$ plane. Hence for high efficiency devices, the $(11\bar{2}0)$ plane has to be used. ZnO/R-sapphire SAW devices have been fabricated with a coupled velocity of 5200 ms^{-1} . Another approach is to use the higher order Rayleigh wave, also known as the Sezawa wave.^{73,74,75,76,77} The Sezawa wave also has a higher electromechanical coupling coefficient, and hence devices operating at higher frequencies can be fabricated with a low insertion loss. The Sezawa wave properties in a $(11\bar{2}0)$ ZnO film on $(01\bar{1}2) \text{ Al}_2\text{O}_3$ have been studied in more detail,⁷⁸ and it has been established that the optimum direction for SAW propagation is along the $[0001]$ direction of ZnO, where the phase velocity is high and there is strong electromechanical coupling.

Diamond, which does not show piezoelectricity has amongst the highest elastic stiffness constants, and hence the acoustic velocities are very high (11000 ms^{-1}). Thus by depositing ZnO on diamond films, the SAW can be coupled from the ZnO film to the diamond films, which will result in high frequency SAW devices.⁷⁹

For low-loss high-frequency SAW devices, more stringent requirements are placed on the electromechanical coupling coefficient, insertion loss, and attenuation or transmission loss. All of these parameters are affected by the material properties of ZnO.^{80,81,82} The quality of the film determines the insertion loss (loss in amplitude) of the signal and the coupling coefficient between energy transfer between the electrical and the mechanical signals. The coherency and structure of the interface between ZnO and the substrate determines the efficiency of acoustic energy transfer to the substrate. Thus ZnO films of high-quality are needed for such devices.

2.5 Thin film growth techniques

Many growth techniques have been used to deposit ZnO films on various substrates. Some of the more popular techniques – pulsed laser ablation,^{83,84,85,86} DC-sputtering,⁸⁷ RF sputtering,^{78, 88} Magnetron sputtering,⁷⁷ ECR plasma sputtering^{64,89,90} – will be discussed in this section. A brief introduction to each growth technique is given below.

(i) Pulsed Laser Deposition (PLD): In PLD, a ZnO target (usually obtained by sintering of ZnO powders) is irradiated with a pulsed laser, which results in local heating and vaporization of the target. While the energy of the individual photons might not be enough for evaporation, absorption of multiple photons (from a high intensity beam) by the same atom can result in evaporation. The evaporant is directed in a narrow lobe, called the plasma plume, oriented closely perpendicular to the target. The substrate onto which the film has to be deposited is placed close to the target in the path of the plasma plume, whereby the atoms and molecules deposit onto the substrate. The plasma plume usually consists of macroparticles in addition to the vapor atoms or molecules, which when incorporated into the growing film will degrade the film's properties. While certain measures can be taken to limit macroparticle incorporation in to the film, it cannot be completely eliminated. Other drawbacks such as lack of uniformity, difficulty in controlled doping, difficulty in producing smooth multi-layer films etc., limit the effectiveness of using PLD for the deposition of high-quality films on a large scale.

(ii) Sputtering Techniques: DC sputtering, RF sputtering, Magnetron sputtering and ECR plasma sputtering have the same operating principle. The positive ions generated in

the plasma (Ar^+ ions in an Ar plasma) are accelerated towards the cathode (which is the source for the material to be deposited onto a substrate) and collide with the atoms of the cathode. Momentum transfer results in the emission of the cathode atoms, which are then transported across the plasma by diffusion, and are deposited onto the anode (substrate). A fraction of the emitted atoms redeposit onto the cathode. Thus matter is constantly transferred from the cathode to the substrate resulting in film growth. The main difference between the different techniques is the way the plasma is generated, which has an effect on some of the plasma and deposition parameters. Thus the quality of the film depends on the deposition technique.

A plasma is a collection of free charged particles formed by the dissociation and ionization of molecules or atoms either by sufficiently high thermal energy or electric fields. It is a dynamic state of matter where the ionization process (of atoms) and the recombination process (of ions with electrons forming neutral species) are constantly occurring. In order to maintain a plasma, power has to be constantly input into the system to ionize the neutral species. In almost all plasma deposition techniques, the ionization of the gaseous species is carried out by either creating large electric fields in the chamber or through coupling with electromagnetic radiation.

Plasmas, are joined to wall surfaces (or any other surface in contact with the plasma) across thin positively charged layers called *sheaths*. Sheaths are formed due to a net loss of electrons to the surface compared to positive ions, resulting in a local increase in positive ion concentration. The potential drop across the sheath results in a retarding force on electrons (in the plasma) moving towards the walls, and accelerates positive ions towards the walls. Under the right conditions, sputtering of the walls (or cathode) can

occur. When the energy of the ions is lower, they will not have enough momentum to dislodge an atom from the cathode, instead the impinging ion will get implanted into the surface. This process is known as ion-implantation.

In *DC sputtering* systems, the anode is at ground and a negative DC voltage is applied to the cathode. The bulk of the plasma floats above ground by the plasma potential, and has little voltage drop across it because of the high conductivity relative to that of the sheaths. Hence, essentially all the applied voltage appears across the cathode sheath. This voltage drop results in high-energy ion bombardment and sputtering of the cathode. DC plasmas require the electrodes to be conducting, hence only metallic targets have to be used. For the deposition of ZnO, a Zn target can be used in an Oxygen plasma.

In *RF sputtering* systems, an RF voltage is applied to the cathode. Insulating materials can be used as the cathode and anode as power will be transmitted through the material through capacitive coupling. In RF plasma systems, the sheath voltages are not as high as in the DC systems, which results in lower ion damage.

In *Magnetron sputtering*, an additional magnetic field is introduced to trap the electrons in orbits about the magnetic field lines. This increases the electron path lengths before they escape to the anode by collisional scattering. Consequences of this are – much lower pressures can be used, deposition rate can be increased, lower voltages can be used resulting in lower sheath voltages, and hence lower damage due to negative ions.

In Microwave plasma systems, the electric field generated by a resonant standing microwave ionizes the atoms in the gaseous phase, forming a plasma.

In an *Electron Cyclotron Resonance (ECR)* plasma system, a magnetic field is established parallel to the direction of the microwave beam and thus perpendicular to the

electric field. Electrons accelerated perpendicular to B and E will orbit in a plane perpendicular to B with a cyclotron radius, and at the right combination of B and E , the electrons will always be in phase with E , resulting in high energy electrons. More efficient transfer of power is possible in this system and lower pressures can be employed.

In a compound target, when one element has a low ionization potential (zinc) and the other has a high electron affinity (oxygen), it is likely that the latter element will be sputtered as a negative ion rather than as a neutral atom. Negative ions get accelerated into the plasma by the cathode sheath field. Under low pressures, these ions can cross the plasma to the depositing film and bombard it with enough energy to damage it or erode it. Negative Oxygen ion bombardment effects during deposition have been to increase the attenuation coefficient and decrease the SAW velocity of ZnO films.^{82,91} Similar effects have been found after Ar^+ ion implantation in Lithium Niobate.⁴¹ Under typical growth conditions, sputtering produces ZnO films with high resistivity while films grown by MOCVD or bulk samples grown by vapor deposition techniques result in low resistivity. It has also been shown that oxygen ion-implantation results in an increase in resistivity.³⁸ We can surmise that there is a connection between these two observations and say that considerable oxygen ion-implantation or bombardment occurs during most sputtering processes. SAW devices with good characteristics have been grown by ECR sputtering techniques, but the effect of oxygen ion bombardment has not been evaluated. Emerging new device applications, such as low-loss filters operating in the GHz range and ZnO based UV lasers, need high quality epitaxial films, which cannot be achieved through sputter deposition, and hence in the present work, we use MOCVD grown ZnO films.

2.6 Summary

From a review of the properties of ZnO given in this section, we can see that ZnO is a versatile material which has many important applications. For devices of improved performance, films of high structural quality are required. Moreover a better understanding and correlation between the properties (such as SAW and optical) and the structure of the films is required. In this dissertation, we address some of these issues. MOCVD will be used to deposit epitaxial ZnO films on R-sapphire and the unique SAW properties and optical anisotropy in the ZnO/R-Al₂O₃ structure will be investigated for device applications.

Chapter 3 : MOCVD Growth of ZnO films on Al_2O_3

3.1 MOCVD Technology

Chemical Vapor Deposition (CVD) is defined as the formation of a nonvolatile solid film on a substrate by the reaction of vapor-phase chemicals (reactants) that contain the required constituents. Most elements can be converted to chemical vapors by reacting them with functional groups (H , CH_3 , C_2H_5 etc.,) which have only one dangling bond. The resulting molecules ($(\text{CH}_3)_3\text{Ga}$, $(\text{C}_2\text{H}_5)_2\text{Zn}$ etc.,), known as metal-organics, do not chemically bond to each other and hence have a high vapor pressure. In Metal-Organic CVD (MOCVD), one or more of the reactants is a metal-organic compound.

The main steps involved in MOCVD or CVD growth are

- a. Convective transport of source gases/metalorganics from the injected or entry point to the substrate.
- b. Diffusional transport of the gases through the relatively stationary "boundary layer" formed at the substrate surface due to viscous friction to gaseous flow close to the substrate surface.
- c. Adsorption of the gaseous species onto the substrate surface.
- d. Diffusion and chemical reaction of the various species on the surface resulting in deposition
- e. Desorption of product organic species such as CH_4 , H_2 etc.,

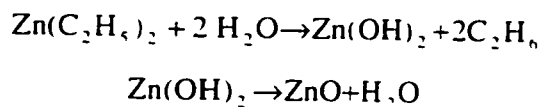
There can be two rate limiting steps based on the above sequence of events. At low temperatures, the rate of the surface reactions is reduced and the deposition is *surface-*

reaction-rate-limited. At higher temperatures, transport of the gaseous species through the boundary layer is rate limiting, and hence deposition is *mass-transport-limited*.

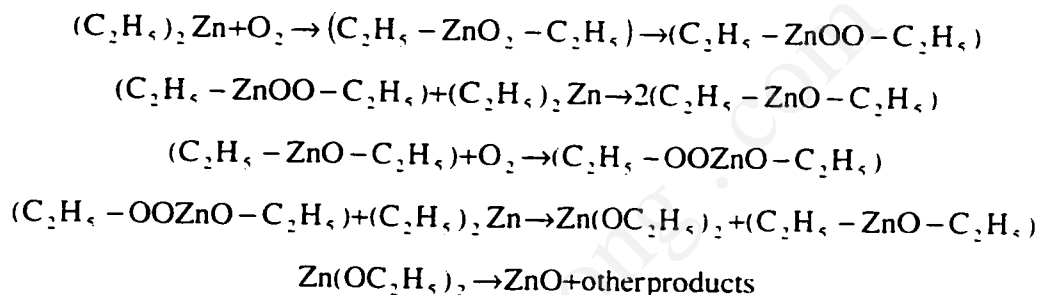
An advantage of using metal-organics instead of metal vapors is that they do not condense on the chamber walls at room temperatures. Hence the "line-of-sight" geometry that is required for metal vapors (i.e. the substrate should be in the direct line of sight of the vapor source) is not necessary when using metalorganics. Moreover, while direct condensation is the growth method when using metal vapors, in MOCVD the reactants adsorb on to the substrate surface and chemically react with one another. Thus additional control of the growth process is possible through the chemical interactions amongst the sources as well as due to interaction between the sources and the substrate.

Di-Methyl Zinc [DMZn : $(\text{CH}_3)_2\text{Zn}$] and Di-Ethyl Zinc [DEZn : $(\text{C}_2\text{H}_5)_2\text{Zn}$] are the most commonly used zinc metalorganic sources. CO_2 , O_2 , N_2O , and H_2O have been used as the oxygen source. A brief review of the relevant properties of the metalorganic compounds is given below.⁹² In the organozinc compounds the Zn–C bond is predominantly covalent and the C–Zn–C group is linear as a result of *sp*–hybridization. In agreement with their non-polar character, these compounds are among the most volatile organometallic compounds. The melting point of DEZn is -28°C , and its boiling point is 117°C and 30°C at pressures of 760 mm Hg and 27 mm Hg respectively. The strongly electrophilic (accepts an electron) character of zinc largely determines the chemical behavior of these compounds. They are electron deficient compounds in that the number of low lying orbitals available for bonding (four) is greater than the number of bonding electron pairs (two). This presence of vacant orbitals for bonding explains the tendency of DEZn to form complexes with compounds containing hetero atoms with free

electron pairs (O, N, P, S etc.,). At the same time this serves to explain the great chemical reactivity of DEZn. DEZn is highly susceptible to attack by oxygen and water. The reaction with water is



while the reaction with oxygen is more complicated. A probable path is⁹³



While a higher growth rate can be obtained by using DMZn instead of DEZn due to the higher vapor pressure of DMZn, it has two main shortcomings,

- Both DMZn and DEZn dissociatively adsorb^{94,95} onto most substrates at temperatures above 400 K, resulting in zinc metal and adsorbed methyl and ethyl groups respectively. Unlike methyl groups, the larger ethyl groups can undergo β -hydride elimination reactions to produce ethene (C_2H_4), which then desorbs. This results in lower rates of carbon contamination during MOCVD film growth with DEZn.
- Relative to DEZn, DMZn reacts much more vigorously with O_2 and H_2O .

Hence, it is very difficult to limit gas phase reactions if DMZn is used.

As mentioned above, even DEZn reacts with O_2 and H_2O at room temperature. Hence alternate Zn metalorganic sources have been investigated.

Most of the earlier work was carried out using DEZn and $O_2/CO_2/H_2O/N_2O$ as the reactants.^{96,97,98,99} Films of good quality were obtained on 3.8 cm R- Al_2O_3 wafers at 730°C and 400 torr by using N_2O as the oxidizer and N_2+H_2 as the carrier gas.⁹⁷ SAW filters were fabricated, and an electromechanical coupling coefficient of 0.61 % was obtained for a t_{ZnO}/λ ratio (film thickness to SAW wavelength ratio) of 0.08. It was also observed that at higher growth rates, the quality of the films decreased dramatically, which coincided with the growth of needle shaped crystals elongated along their c-axis and growing out of the plane. Optimum growth temperatures were either 400° or 500°C with H_2O and CO_2 as the oxidizing agents respectively. Alternate oxidizing agents such as tetrahydrofuran (C_4H_8O) have been found to reduce the gas phase reactions,¹⁰⁰ and single source precursors which provide both the Zn and O atoms,¹⁰¹ such as MethylZinc isopropoxide [$CH_3Zn(OCH(CH_3)_2)$] and Methyl Zinc tert-butoxide [$CH_3Zn(OC(CH_3)_3)$], have also been used. Another technique which has been used is laser or photo-CVD,^{102,103,104} wherein a UV laser beam either irradiates the substrate or passes parallel to the substrate. The effect of the UV beam is to provide additional energy for the surface reactions to proceed, and hence lower substrate temperatures can be used.

We have chosen DEZn and O_2 as the reactants since they are the most commonly available sources. One of the aims of the present work is to modify the MOCVD reactor geometry in order to reduce or limit the gas phase reactions between DEZn and O_2 , and to obtain high-quality ZnO films on large area (75 mm diameter) sapphire substrates.

3.2 MOCVD System

A schematic of our MOCVD system is shown in Figure 3-1. An IBM-compatible PC fitted with Data Acquisition (DAQ) boards is used to control and monitor all mass flow controllers (MFC) and pneumatic valves, and to obtain temperature in the reactor and the pressure in the reactor and the metalorganic bubblers. N_2 is used as the carrier gas, which is introduced into the MOCVD reactor from the top. Ultrahigh purity Ar is passed through the DEZn bubbler maintained at temperatures in the 0 to 20 °C range (vapor pressure 3.6 – 12.2 mm Hg). The Ar flowing through the bubbler becomes saturated with DEZn vapor, which is then transported to the growth chamber. In order to reduce the transit time for DEZn to reach the growth chamber, additional Ar flow of 1000 sccm was added to the DEZn line at the exit side of the bubbler. High purity O_2 is introduced into the growth chamber through a separate line. The vacuum system consists of two stages, the first stage is a roots blower which allows a high volume of gas to flow, and the second stage is a roughing pump. The best vacuum that can be achieved by this system (with no gas flow) is 10^{-1} to 10^{-2} torr.

We have chosen an axisymmetric reactor with the gases flowing vertically, also known as the rotating-disk vertical flow reactor,^{105,106} since it provides the best uniformity compared with other reactor designs. The basic version of this reactor consists of a horizontally placed wafer susceptor which can be rotated at high speeds, and can be heated (through radiation) by a resistive heater placed below the susceptor. Gases flow from the top and exit through an exhaust at the bottom. A schematic of the flow pattern over a rotating susceptor is shown in Figure 3-2.

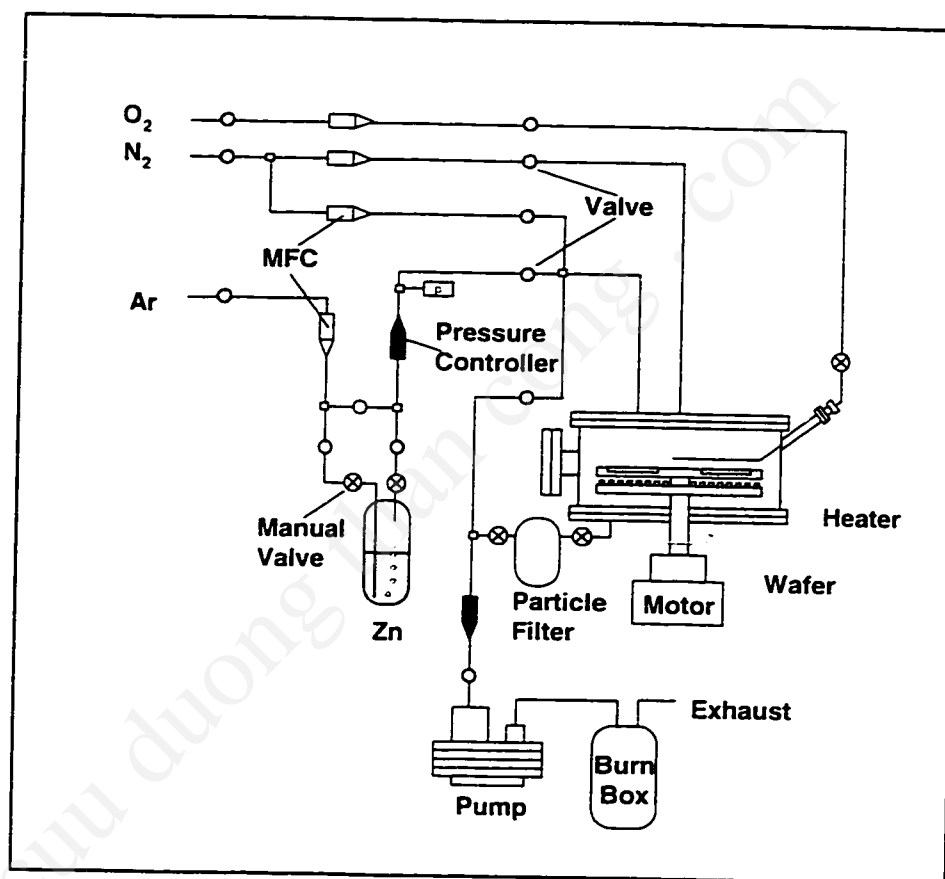


Figure 3-1: A schematic diagram of the MOCVD system

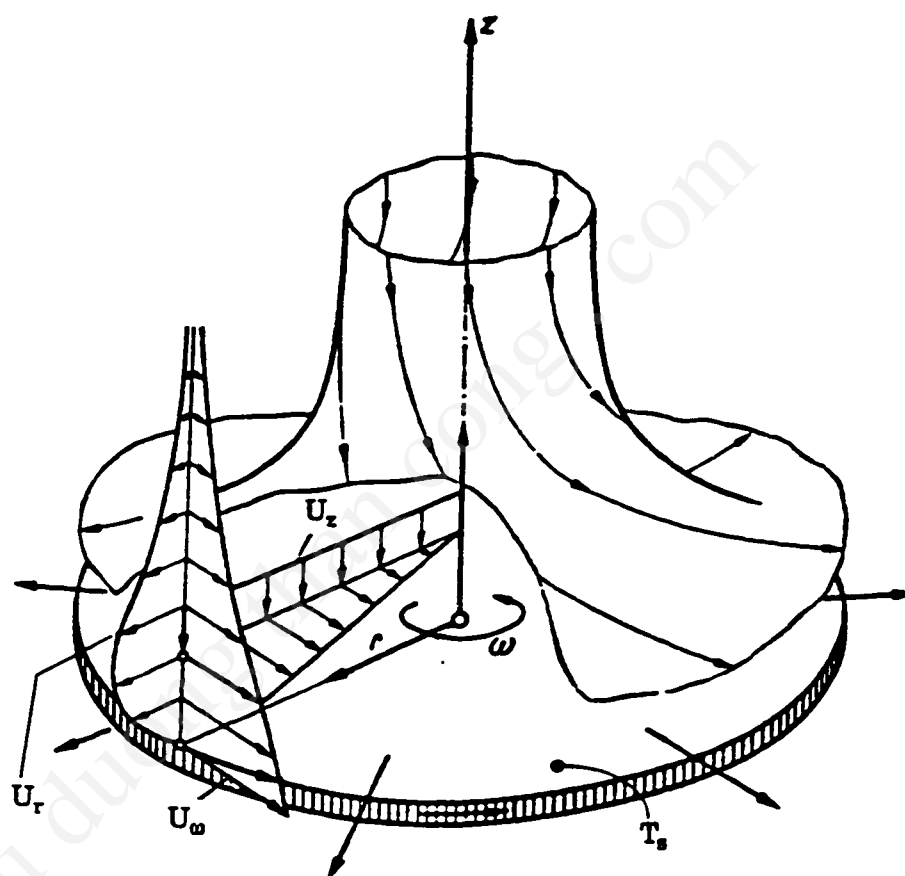


Figure 3-2: A schematic diagram of the flow patterns in a Rotating-disc vertical flow MOCVD reactor. [107]

The vertical velocity of gas flowing downward is reduced as it approaches the susceptor and is redirected radially, reaching a stagnation point of zero vertical velocity at the susceptor surface. The flow pattern is characterized by a boundary layer of fluid being dragged around with the disk and thrown outward by centrifugal force. This centrifugal pumping action also sucks gas down toward the disk. When the susceptor is heated, the gas above the susceptor is heated and rises up due to buoyancy, and then falls again after being recooled. This instability develops into circulating flow patterns. Circulation can result in undesirably long residence time and can degrade the uniformity. In the case of ZnO growth, such flow patterns have to be avoided since small particles which form due to gas-phase reactions will stay in the reactor and grow, and will degrade the growing film if they deposit on to the wafer. These circulating flow patterns can be avoided by maintaining a large downward flow. Hence a large volume of carrier gas has to be constantly introduced from the top.

As mentioned earlier, DEZn reacts with O_2 even at room temperature. Therefore, care has to be taken while introducing the gases into the growth chamber to minimize gas phase reactions. We modified the high speed rotating disk-vertical flow reactor mentioned in the previous paragraph in order to reduce the pre-reaction. DEZn and O_2 were introduced through separate injectors into the growth chamber (Figure 3-3). The injectors which have a series of small holes facing the substrate, are placed horizontally at a distance of 2.5 cm from the wafer carrier. The two injectors are positioned such that the gases from each injector reach the substrate at different regions at any instant.

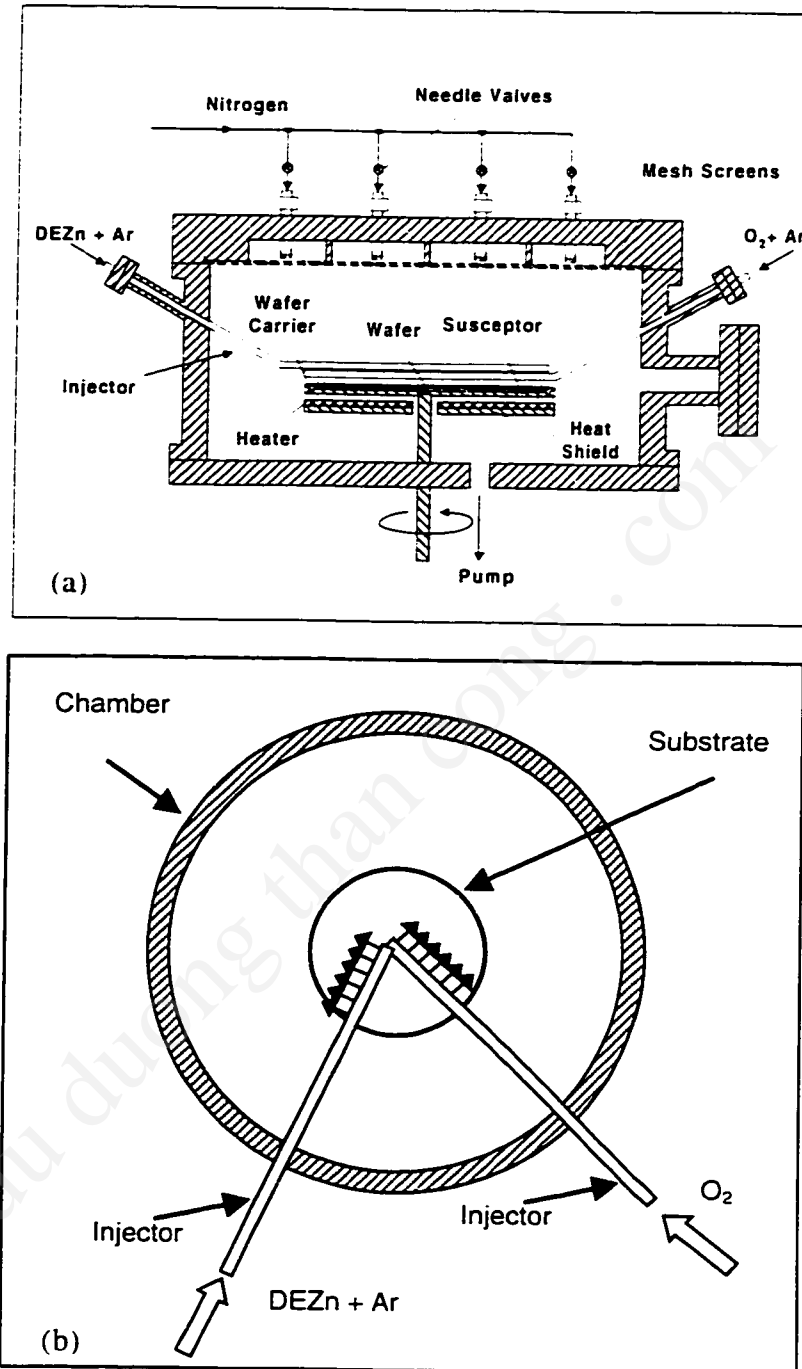


Figure 3-3: A schematic diagram of our MOCVD reactor. (a) Side view and (b) Top view. The figures show the position of the injectors relative to the substrate holder.

This system configuration provides the separation of DEZn from O_2 , and a small transit time for the gaseous species due to the high speed of gases coming out of the holes in the injectors and the short distance from the injectors to the substrate, resulting in a reduction of gas phase reactions. At the same time, rotation of the substrate leads to uniform growth.

A substrate is loaded onto the susceptor, following which the chamber is evacuated to the minimum pressure possible and maintained at this pressure for 10 to 15 minutes. The susceptor is rotated at a speed of 500 to 1000 rpm, and is heated by applying a dc voltage across (passing a dc current through) the resistive heater placed below the susceptor. Meanwhile, the N_2 flow is increased to the required value and the chamber pressure also increased to the set point. Ar is passed through the bubbler but is not introduced into the growth chamber at this time. It bypasses the growth chamber through a bypass line and is transferred directly to the exhaust system. Once the susceptor is heated up to the required temperature (measured by a thermocouple placed very close to the susceptor but not in contact with it), O_2 is introduced through one of the injector tubes mentioned in the previous paragraph, and the DEZn saturated Ar is introduced through the other injector.

3.3 Substrate Selection

The $ZnO/(01\bar{1}2) Al_2O_3$ system possesses anisotropic properties for various important applications, such as acousto-optic,⁴⁴ and surface acoustic wave devices.⁷⁷ This structure is chosen instead of $ZnO/(0001) Al_2O_3$ for SAW devices, as the $ZnO/(0001) Al_2O_3$ structure offers a low electromechanical coupling coefficient (1 %) compared to a value of 6 % for $ZnO/(01\bar{1}2) Al_2O_3$. In addition, higher order Rayleigh waves, known as

Sezawa waves, which have a higher acoustic velocity can be excited on ZnO/(01 $\bar{1}$ 2) Al₂O₃. Hence ZnO films grown on R-Al₂O₃ are preferable for high-performance, high-frequency SAW devices. Very recently, an optically addressed normal incidence UV light modulator that uses the anisotropic absorption and concomitant ultrafast polarization rotation near the lowest exciton to achieve high contrast. Due to these important applications, we have concentrated our efforts to grow ZnO films on (01 $\bar{1}$ 2) Al₂O₃ (R-plane sapphire). The lattice parameters of ZnO and Al₂O₃ are given in Table 2-1.

3.4 Growth Optimization

The optimum growth temperature were determined by depositing ZnO films on C-sapphire and Si substrates. The x-ray diffraction θ – 2θ scans from the samples grown on Si are shown in Figure 3-4. It can be seen that the most crystalline films are obtained at around 450° C. At lower temperatures, the temperature is not high enough for the formation of highly crystalline films. At higher temperatures, gas phase reactions are predominant which results in poorer quality films. This is also observed in Figure 3-5, which shows SEM images of ZnO films deposited on C-sapphire at (a) 585°C and (b) 480°C. The samples were annealed at 850°C for 1 hr after growth. Particle like deposition is seen in Figure 3-5(a), which is due to the dominant gas phase reactions at high temperatures. Hence a temperature between 400°C to 450°C has been chosen as the optimum growth temperature.

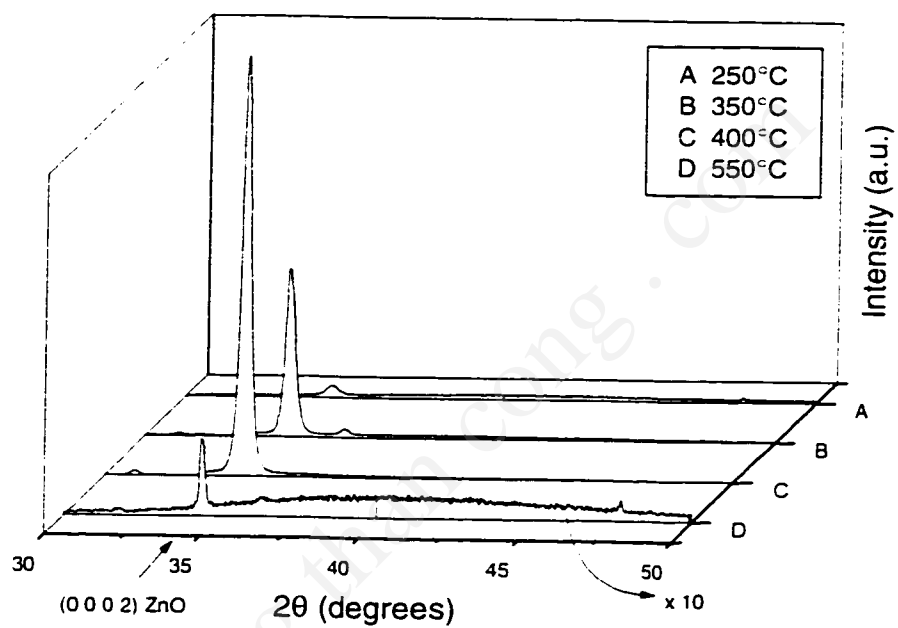
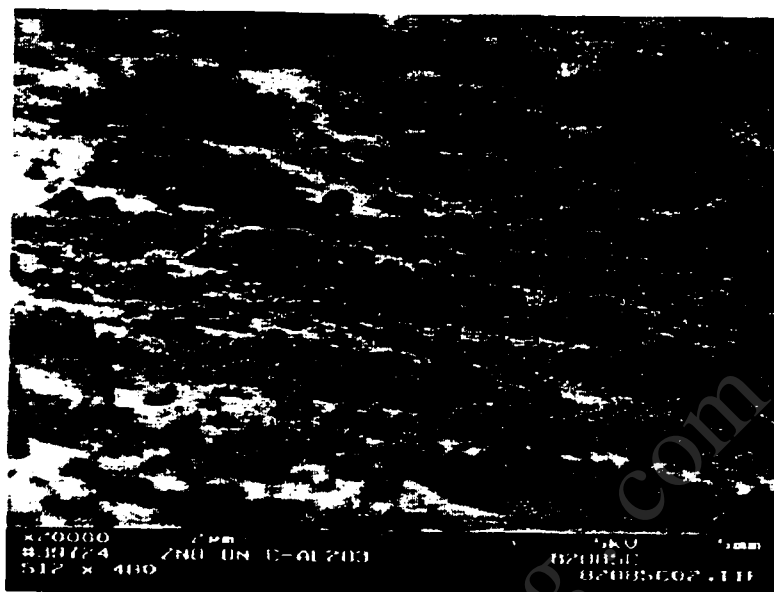
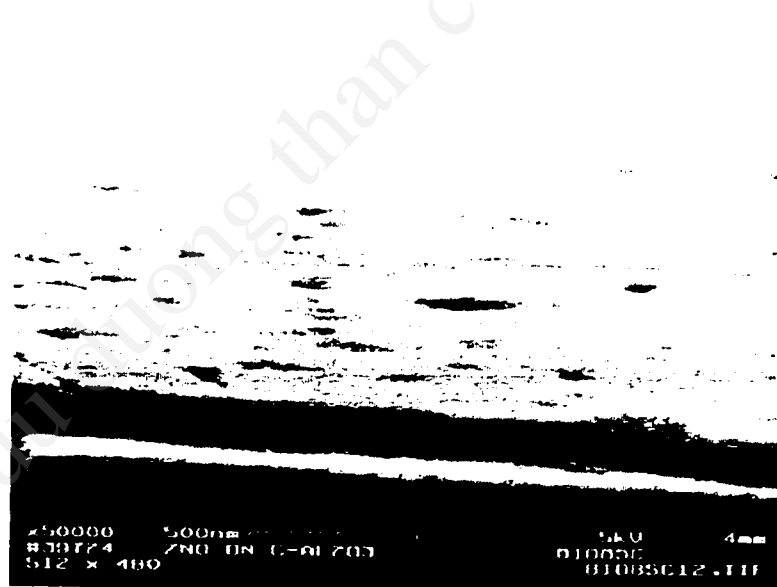


Figure 3-4: Effect of growth temperature on the x-ray θ - 2θ intensities of ZnO films grown on (100) Si.



(a)



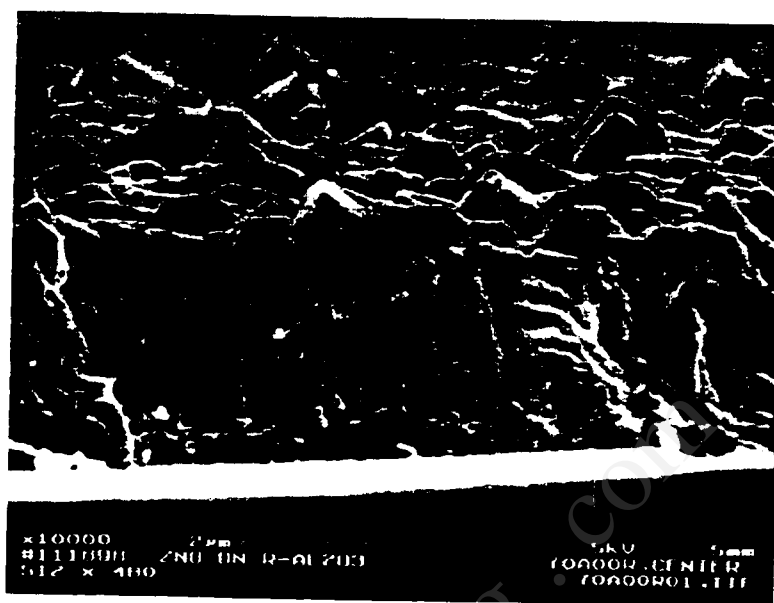
(b)

Figure 3-5: SEM images of ZnO films grown on C-sapphire at (a) 585°C and (b) 400°C. Particle like deposition is seen in (a) due to predominant gas phase reactions.

Under optimum conditions, growth occurs by the coalescence of multiple grains via surface diffusion and step movement, resulting in smooth films. At high growth rates, more material is deposited on these grains before coalescence and step movement occurs, which results in a rough surface morphology. SEM images of films grown on R-plane Al_2O_3 with different growth rates are shown in Figure 3-6. The film grown under high growth rates is observed to have a very rough surface morphology compared with the film grown under lower growth rates.

Typical growth conditions that were used for the growth of smooth films on R-plane Al_2O_3 are as follows: chamber pressure of 20 to 50 torr; an optimum growth temperature of 400 to 450 °C; a total carrier gas flow from the top of 5000 to 15000 sccm; Ar flow through the bubbler of 100 sccm; and an O_2 flow of 1000 to 3000 sccm. An additional flow of 1000 sccm of Ar was introduced into the DEZn line immediately at the exit of the bubbler to reduce the transit time of DEZn to the reactor. The DEZn bubbler was maintained at a temperature between 0° and 20°C, and the pressure at the outlet of the bubbler was maintained at 500 torr. The rotation speed of the susceptor was between 500 and 1000 rpm. The growth rates obtained were between 1 to 2 micron/hour.

Other growth morphologies observed under un-optimized growth conditions are shown in Figure 3-7. Figure 3-7(a) shows a film grown on C-plane Al_2O_3 , (b) shows whisker like growth on (100) Si, and (c) shows a film on R-plane Al_2O_3 .



(a)



(b)

Figure 3-6: SEM images of ZnO film on R-plane Al₂O₃ grown under different growth rates. The film in (a), grown at a higher growth rate, has a rough morphology compared to the film in (b), which was grown with a lower growth rate.

Spurious growth due to DEZn condensation and leaks

Spurious whisker like growth was observed initially in ZnO samples grown on (100) Si and on (01 $\bar{1}$ 2) Al₂O₃. The whiskers observed on Si were studied in more detail through TEM.

These whiskers have a tip with a different structure than the base or body of the whisker. From the TEM images of the whiskers (Figure 3-8), it can be seen that the interface between the tip and the body is extremely flat, and is parallel to the (0001) planes of the ZnO body. The shape of the tip is approximately hemispherical, with facets appearing in some cases. The tip consists of multiple crystalline regions.

Amongst the mechanisms for whisker growth, the Vapor-Liquid-Solid (VLS) mechanism is the most widely accepted mechanism. Based on this mechanism, a liquid phase is formed due to one of the following reasons: the formation of a eutectic phase between the condensed phase and the substrate, or due to impurities present on the surface, or if a phase with a low melting point is present in the system. Once the liquid phase is formed, the reactant gaseous species will adsorb onto the liquid much more efficiently than onto a solid surface. Then these reactants are transported through the liquid to the solid-liquid interface, where growth of the solid phase proceeds. Due to the much larger accommodation coefficient of the reactant species in the liquid, growth is much faster at the liquid-solid interface than at the solid-vapor interface. Usually, the solid-liquid interface is the close packed plane. Detailed investigations of whisker growth have been carried out to establish the kinetics of the VLS mechanism^{108,109}.

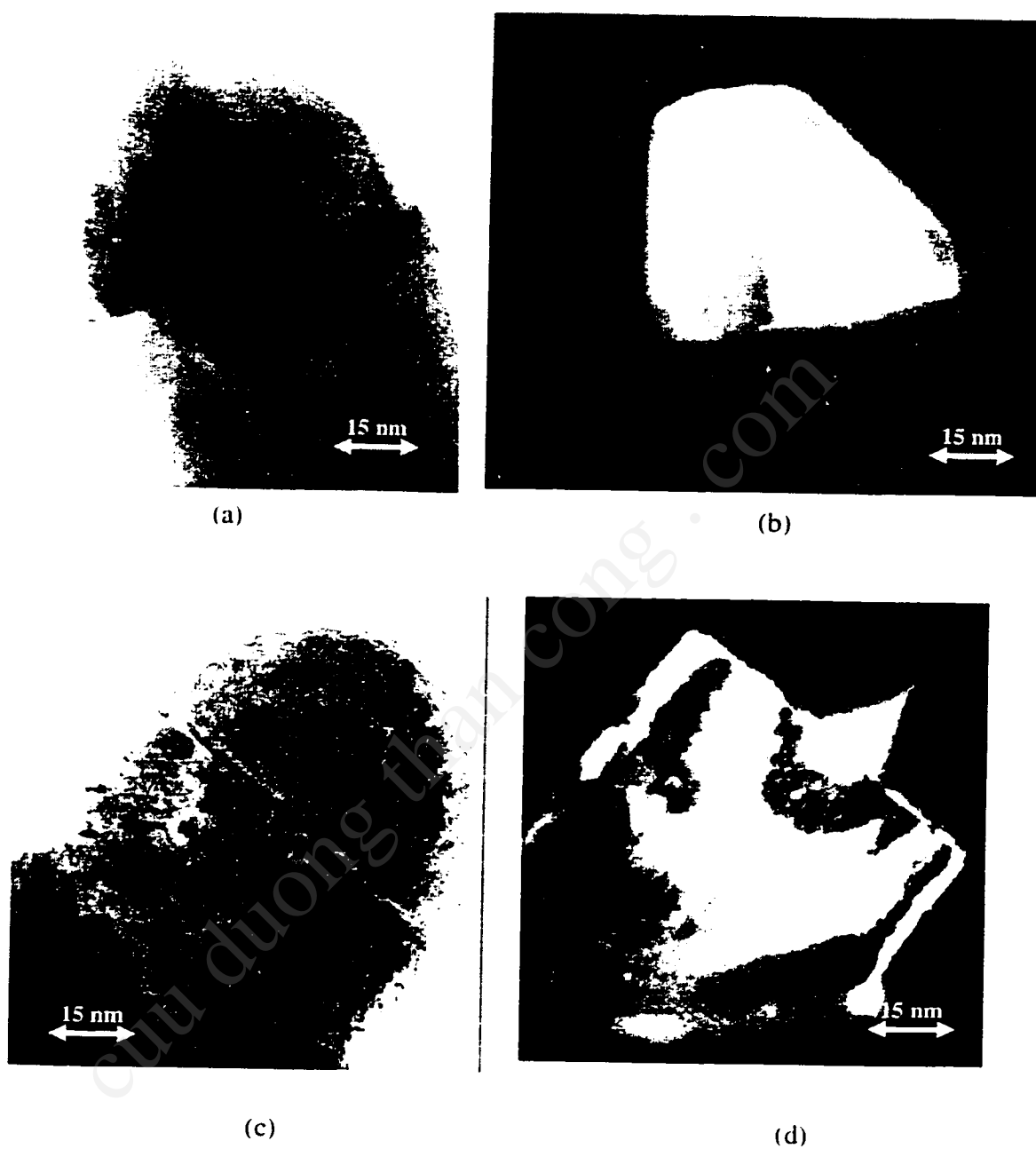


Figure 3-8: TEM images of whiskers observed under spurious growth conditions. (b) and (d) are dark field images corresponding to (a) and (c) respectively. It can be seen from (b) and (d) that the tip consists of multiple crystalline regions.

In the present case, the growth temperature was between 450 - 500°C, which is greater than the melting point of Zn. We suggest that these whiskers were grown by the VLS mechanism, with liquid Zn or a Zn rich phase at the tip. The Zn rich region could have formed by condensation of DEZn onto some impurity particle and could melt when it enters the hot zone in the reactor. The tip consists of multiple crystalline regions. These samples were cooled down in an oxygen atmosphere and hence it is reasonable to assume that the Zn at the tip was oxidized during the cool down stage.

Chapter 4 : Structural Characterization

In this chapter, the surface morphology, epitaxial relationship between ZnO films and the R-plane sapphire substrates, and the structure of the ZnO/R-Al₂O₃ interface are evaluated for the films deposited by MOCVD under optimum growth conditions. A description of the X-ray θ - 2θ and ϕ -scan techniques is given in Appendix C.

4.1 Epitaxial Relationships

The x-ray θ - 2θ scans obtained from a ZnO film deposited on an R-plane sapphire substrate is shown in Figure 4-1(a). For comparison, the scan from ZnO grown on C-sapphire is shown in Figure 4-1(b). From these scans we observed that ZnO grows on R-sapphire with a $(11\bar{2}0)$ orientation, while (0001) ZnO grows on C-sapphire. The in-plane crystallinity was analyzed by the XRD ϕ -scans. The x-ray ϕ -scans from the $\{21\bar{3}1\}$ and $\{21\bar{3}0\}$ family of planes from ZnO and the $\{12\bar{3}5\}$ set of planes from Al₂O₃ are shown in Figure 4-2(a). In a ϕ -scan, the number of planes of a certain $\{h\ k\ \bullet\ l\}$ family which make the same angle with the plane parallel to the surface is determined. In a ZnO single crystal, there are four planes of the $\{21\bar{3}1\}$ type which are at an angle of 15.8° , and two planes of the $\{21\bar{3}0\}$ type which are at angle of 10.9° with the $(11\bar{2}0)$ ZnO plane. The ϕ -scans of the corresponding sets of planes show that there is only one set of four $\{21\bar{3}1\}$ planes and one set of two $\{21\bar{3}0\}$ planes present in the ZnO film. The indices of the corresponding planes based on their relative positions are marked in the figure.

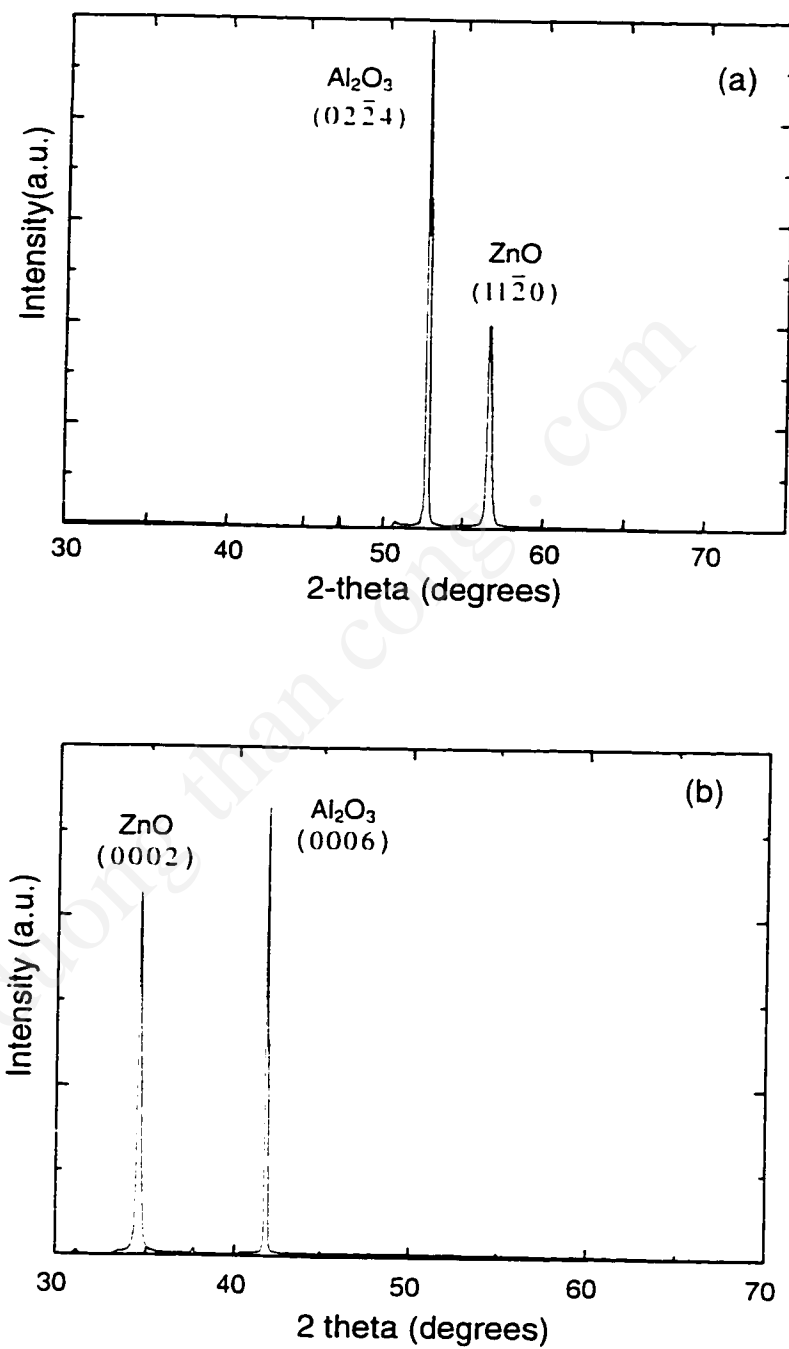


Figure 4-1 X-ray θ - 2θ scans of ZnO grown on (a) R-plane Al_2O_3 and (b) C-plane sapphire.

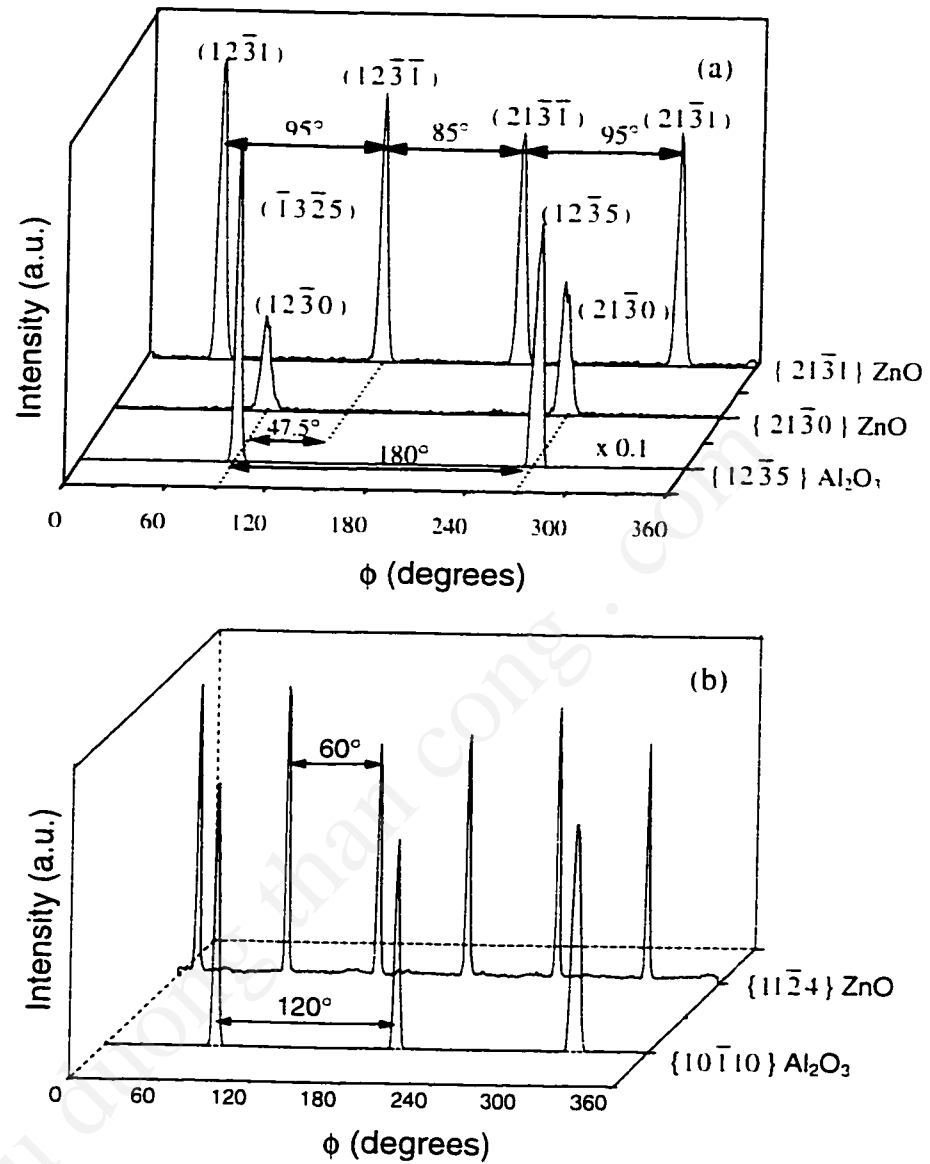


Figure 4-2 (a). x-ray ϕ -scans of the $\{21\bar{3}1\}$ and $\{21\bar{3}0\}$ family of planes from $(11\bar{2}0)$ ZnO and the $\{12\bar{3}5\}$ family of planes from $(01\bar{1}2)$ Al_2O_3 .
 (b). x-ray ϕ -scans from the $\{11\bar{2}4\}$ family of planes from (0001) ZnO and the $\{10\bar{1}10\}$ family of planes from (0001) Al_2O_3 are shown. The three-fold symmetry about the c-axis of Al_2O_3 and the six-fold symmetry about the c-axis of ZnO are seen.

The expected separation between the $(12\bar{3}1)$ plane and the $(12\bar{3}\bar{1})$ plane is 94.5° and that between the $(12\bar{3}\bar{1})$ and $(21\bar{3}\bar{1})$ planes is 85.5° . These angles correspond to the separation between the projections of the normals to the planes on to the $(11\bar{2}0)$ plane. The values obtained are within experimental error. Hence, the films that are obtained are epitaxial, with all the grains having the same orientation.

There are two planes of the $(12\bar{3}5)$ type in sapphire which make an angle of 16.31° with the $(01\bar{1}2)$ plane: the $(12\bar{3}5)$ and $(\bar{1}3\bar{2}5)$ planes. Both these reflections are allowed based on the extinction condition $(-h+k+l=3n \text{ for sapphire}^8)$. The ϕ -scan from this family of planes is also shown. These two peaks coincide with the $\{21\bar{3}0\}$ peaks from ZnO. Hence from the relative positions, the epitaxial relationship between ZnO and sapphire can be evaluated. The zone axis corresponding to $(11\bar{2}0)$ and $(21\bar{3}0)$ reflections of ZnO is $[0001]$, while the zone axis corresponding to $(01\bar{1}2)$ and $(\bar{1}3\bar{2}5)$ of Al_2O_3 is $[\bar{1}\bar{2}1]$ in the three-axis system or $[0\bar{1}11]$ in the four-axis system. These two directions coincide. Hence the epitaxial relationship was determined to be

$$(11\bar{2}0) \text{ ZnO} // (01\bar{1}2) \text{ Al}_2\text{O}_3 \text{ and } [0001] \text{ ZnO} // [0\bar{1}11] \text{ Al}_2\text{O}_3.$$

The positions of the peaks from the $\{21\bar{3}1\}$ x-ray ϕ -scans confirms this relationship. Based on this epitaxial relationship, the c-axis of ZnO lies in the plane of the ZnO film, with a lattice mismatch along the $[0001]$ direction of ZnO of 1.53 %, and that along the $[1\bar{1}00]$ direction of ZnO of 18.3%.¹¹⁰

For comparison, the ϕ -scans from ZnO grown on C-sapphire are presented in Figure 4-2(b). The $\{11\bar{2}4\}$ family of planes from (0001) ZnO and the $\{10\bar{1}10\}$

family of planes from (0001) Al_2O_3 are shown. In these scans, six peaks corresponding to the six-fold symmetry of ZnO and three peaks corresponding to the three-fold symmetry of Al_2O_3 about their corresponding c-axes are observed. Here we consider the hexagonal unit cell of Al_2O_3 . As we can see, there is a 30° rotation between the two lattices. The epitaxial relationship for ZnO films grown on C-plane sapphire is:

$$(0001) \text{ZnO} // (0001) \text{Al}_2\text{O}_3 \quad \text{and} \quad [10\bar{1}0] \text{ZnO} // [2\bar{1}\bar{1}0] \text{Al}_2\text{O}_3.$$

This rotation results in a continuation of the oxygen sublattices in the two materials. Based upon these considerations, the lattice misfit along the $[2\bar{1}\bar{1}0]$ direction of ZnO is found to be 18.3%. The epitaxial relationships are tabulated in Table 4-1.

Table 4-1: Epitaxial relationships between ZnO and R- and C- sapphire

Sapphire substrate	Parallel ZnO plane	Directions, ZnO // sapphire
R $(01\bar{1}2)$	$(11\bar{2}0)$	$[0001] // [0\bar{1}11]$
C (0001)	(0001)	$[10\bar{1}0] // [2\bar{1}\bar{1}0]$

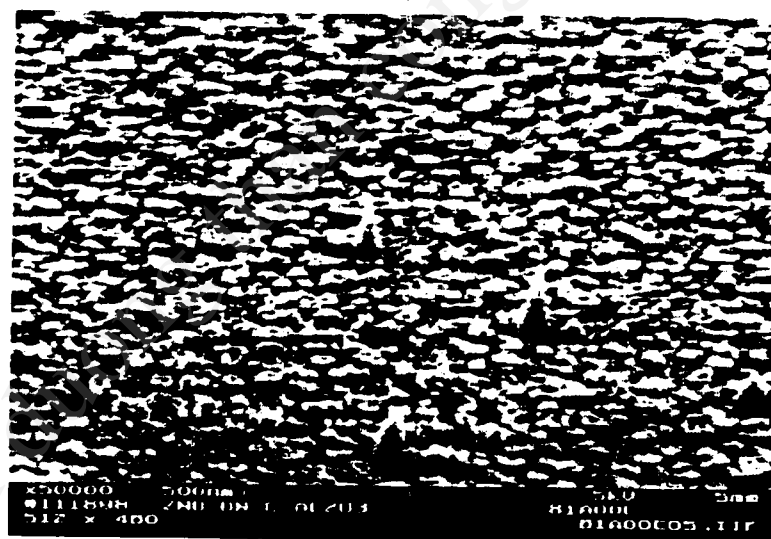
4.2 Surface Morphology

The ZnO films on R-sapphire are very smooth and dense, as seen in the SEM image shown in Figure 4-3(a). In contrast, the films on C-sapphire have a columnar structure, and the grains are elongated along their c-axis (Figure 4-3 (b)). ZnO has a wurtzite structure, with the (0001) planes being Zn-terminated and its $(000\bar{1})$ planes being O-terminated. ZnO has a partial ionic character, which results in a partial and opposite charge on the $[0001]$ and $[000\bar{1}]$ planes. Thus, there is a net dipole moment

when the crystal is terminated by the basal plane, which results in the surface energy to diverge.¹¹ On the other hand, the prismatic planes, i.e., the $(11\bar{2}0)$ and the $(10\bar{1}0)$ planes are nonpolar as they have equal number of O and Zn atoms, and hence have a lower surface energy compared to the basal plane. This results in a high growth rate along the c-axis and a columnar morphology in the case of films grown on C-sapphire. Another interesting feature seen in Figure 4-3(b) is that while most of the grains are either flat or have a small depression, there are a few grains, which are elongated and have a pointed tip. The Zn-terminated side of bulk grown needle shaped crystals has been observed to end as a hexagonal pyramid pointing outward, while the O-terminated end has been observed to have a depression. Compared with the shape of bulk crystals, the elongated grains in Figure 4-3 (b) are expected to be Zn terminated, i.e. grow along the $[0001]$ direction, while the majority of the grains grow in the $[000\bar{1}]$ direction. This can be explained based on the relative positions between the first Zn sub-layer and the first O sub-layer (Figure 4-4). Assuming that the first layer that is formed is the Zn sub-layer. The O layer can occupy the valley positions in-between three Zn atoms or they can occupy the positions exactly above the Zn atoms. O terminated crystals grow in the first case as shown in Figure 4-4(a), while Zn terminated crystals grow in the second case as shown in Figure 4-4(b). For the $(11\bar{2}0)$ ZnO films grown on R-sapphire, the c-axis is in the plane of the film, which results in the absence of a columnar structure. On investigation by transmission electron microscopy, grain boundaries are clearly visible in the films grown on C-sapphire, while threading dislocations are the main defects observed in the films grown on R-sapphire at low growth temperatures (400–450 °C).



(a)



(b)

Figure 4-3 (a) SEM image showing the smooth surface morphology of ZnO on $R\text{-Al}_2\text{O}_3$.
 (b) SEM image showing the columnar structure of ZnO on $C\text{-Al}_2\text{O}_3$. Two types of grains can be seen in this image. The majority of the grains are flat while some of them are elongated.

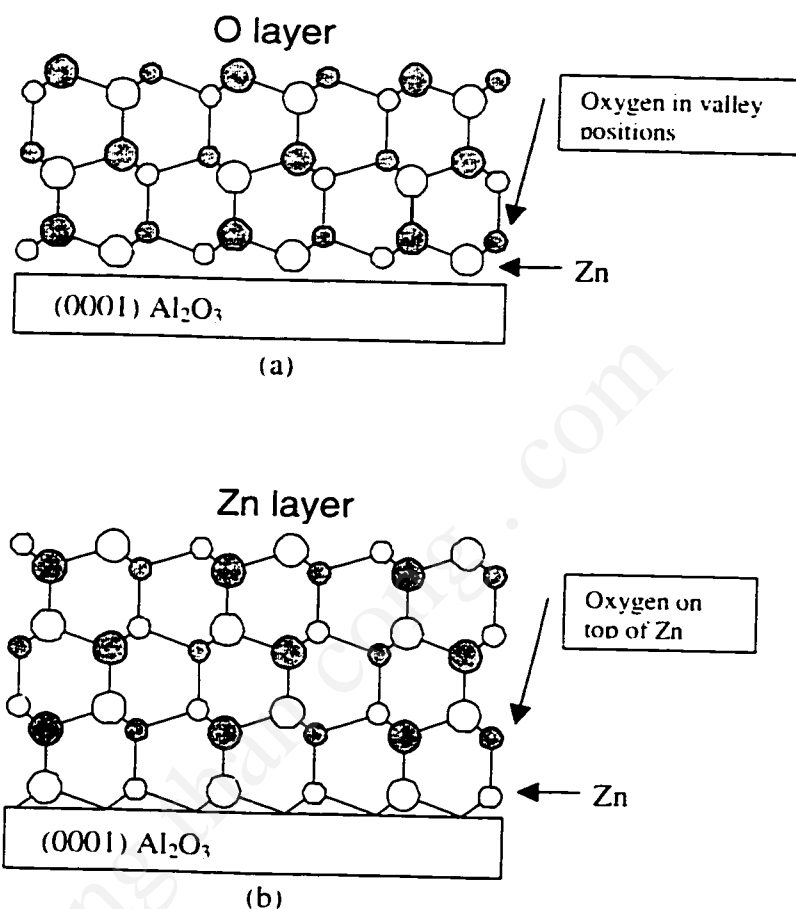


Figure 4-4 The possible origin of the two types of grains seen in Figure 4-3(b).

(a). O-terminated (0001) ZnO results if the oxygen atoms of the first O sublayer occupies the valley positions between Zn atoms of the first Zn sublayer

(b). Zn terminated (0001) ZnO results if the oxygen atoms of the first O sublayer occupy positions directly above the Zn atoms of the first Zn sublayer

4.3 Structure of the ZnO/R-Al₂O₃ interface

The interfacial structure between ZnO and sapphire is important in controlling many properties such as adhesion and surface acoustic wave propagation. Therefore, monitoring the structures and reactions at the interface is of utmost importance in studies of this type. A cross-sectional TEM lattice image of the interface between ZnO and R-sapphire is shown in Figure 4-5(a). The view is along the c-axis of ZnO (c-axis coming out of the plane of the paper). The interface is observed to be atomically sharp and semicoherent. The misfit dislocations can be seen more clearly in Figure 4-5(b), which is a Fourier-filtered image (a) using the $(2\bar{1}\bar{1}0)$ and $(\bar{2}110)$ Al₂O₃ reflections, and the $(1\bar{1}00)$ and $(\bar{1}100)$ ZnO reflections. The $(2\bar{1}\bar{1}0)$ planes in sapphire are continued by the $(1\bar{1}00)$ planes in ZnO. The 18.3% misfit along the $[1\bar{1}00]$ direction of ZnO is relieved by extra half planes on the sapphire side of the interface. On average, there is one dislocation for every five $(1\bar{1}00)$ planes. Assuming that the Burgers vector is perpendicular to the dislocation line, the total misfit between the two lattices is completely accommodated by the misfit dislocations.

In addition, there are locally strained regions at the interface, with a repeat distance almost twice that of the misfit dislocations. The origin of these regions is not understood at present. Due to the semicoherent nature of the interface, the adhesion of the film to the substrate is strong. Moreover, a high efficiency of transfer (low loss) of acoustic energy across the interface is expected for SAW devices with such an interface.

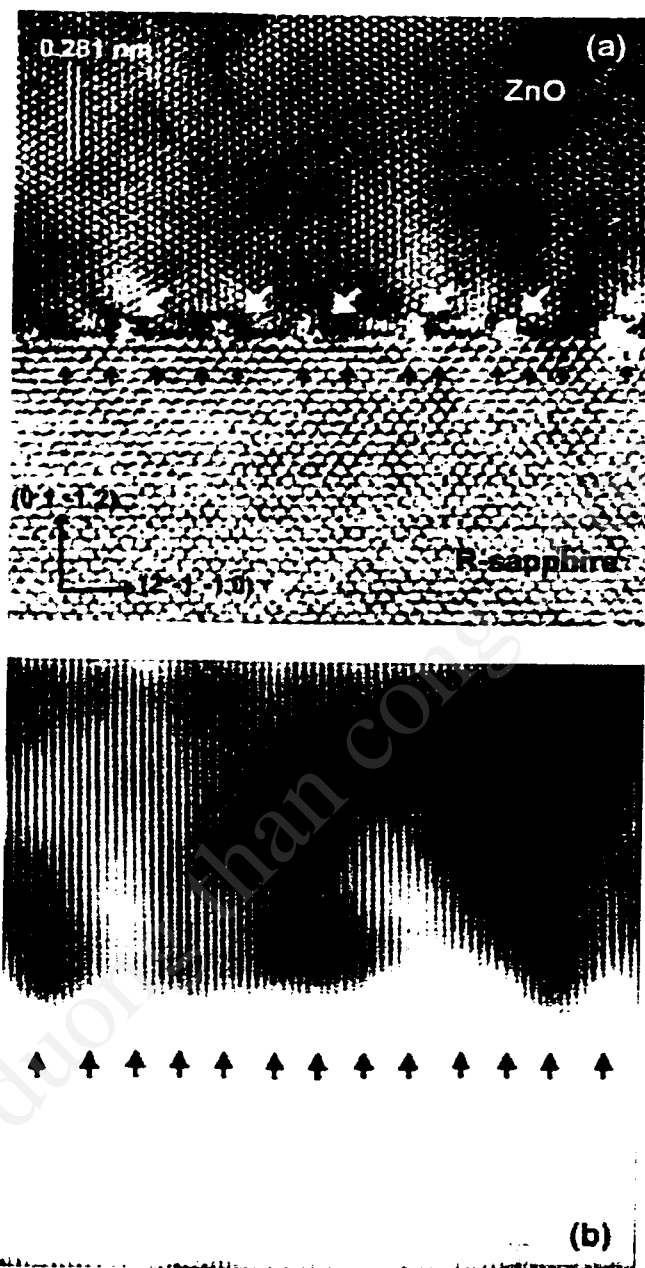


Figure 4-5 (a). HR-TEM image of the interface between ZnO and R-sapphire. (b). Fourier-Filtered image corresponding to image in (a). The view is along the c-axis of ZnO. Highly strained regions with a repeat distance twice that of the misfit dislocations are seen (white arrows).

Chapter 5 : Surface Acoustic Wave And Optical Properties

In this chapter, the fabrication procedure and performance of prototype SAW filters fabricated on $(11\bar{2}0)$ ZnO/ $(01\bar{1}2)$ Al₂O₃ are presented. Photoluminescence spectra (PL) of the as-grown ZnO films, and the absorption characteristics to light polarized parallel and perpendicular to the c-axis of ZnO are also presented.

5.1 Surface Acoustic Wave Devices

5.1.1 SAW Device Design

SAW filters have been fabricated on ZnO/R-Al₂O₃ to evaluate the SAW velocity, insertion loss, and electromechanical coupling coefficient of the films. The $(11\bar{2}0)$ ZnO/ $(01\bar{1}2)$ Al₂O₃ structure is chosen instead of (0001) ZnO/ (0001) Al₂O₃ for SAW devices, since the (0001) ZnO/ (0001) Al₂O₃ structure offers low coupling (1 %) on a ZnO surface. For high-performance SAW devices, ZnO films grown on R-Al₂O₃ are preferred.¹¹¹ These surface waves are confined to a depth of a few wavelengths. The effective electromechanical coupling coefficient of the Rayleigh wave exhibits its maximum in the $[0001]$ direction, and the Love wave effective coupling coefficient maximum is in the $[1\bar{1}00]$ direction.¹¹² The Rayleigh wave has a higher phase velocity than the Love wave; therefore, the IDTs were placed along the c-axis of the ZnO film, as shown in Figure 5-1. In the IDT structure, the center-to-center spacing between two adjacent electrodes (d) determines the wavelength (λ) of the surface wave generated ($\lambda = 2d$ for the simple case of single interpenetrating electrodes). Other waves are also

generated, but the efficiency of energy transfer is very small. The center frequency (f_c) of operation of a pass-band SAW filter is dependent on the velocity (v) of the surface acoustic wave and its wavelength according to the relation $f_c = v/\lambda$.

The SAW filter consists of two interdigital transducers (IDT), one for converting the microwave signal to a surface acoustic wave, and the second for receiving the SAW i.e. for converting the SAW to a microwave signal. The device structure is shown in the following figure. Two device structures were used in order to study the effect of h/λ ratio (ZnO thickness to SAW wavelength) on the SAW velocity (v_{SAW}) and electromechanical coupling coefficient (k_{SAW}^2). The main design parameters are given in Table 5-1.

The wavelength of the SAW generated in devices A and B is 10 μm and 16 μm respectively. These devices were fabricated on 0.5 μm and 1.5 μm thick (h_{ZnO}) ZnO films so that device characteristics for four h_{ZnO}/λ values can be measured.

Surface acoustic waves generated at input IDT travel in both directions of the propagation axis. Hence only half the input power is directed towards the receiving IDT. This results in a 3 dB loss in power transmitted. Moreover, for maximum power transfer at the receiving IDT, the IDT and load impedances have to be matched, which results in another 3 dB loss. Hence there is an inherent loss of 6 dB for this particular filter design.

Table 5-1: Design parameters for the fabricated SAW filters

	Electrode separation ($\lambda/2$)	Electrode width ($\lambda/4$)	Edge-to-Edge IDT1–IDT2 spacing (20λ)	# of electrodes per IDT
Device A	5 μm	2.5 μm	200 μm	81
Device B	8 μm	4 μm	320 μm	81

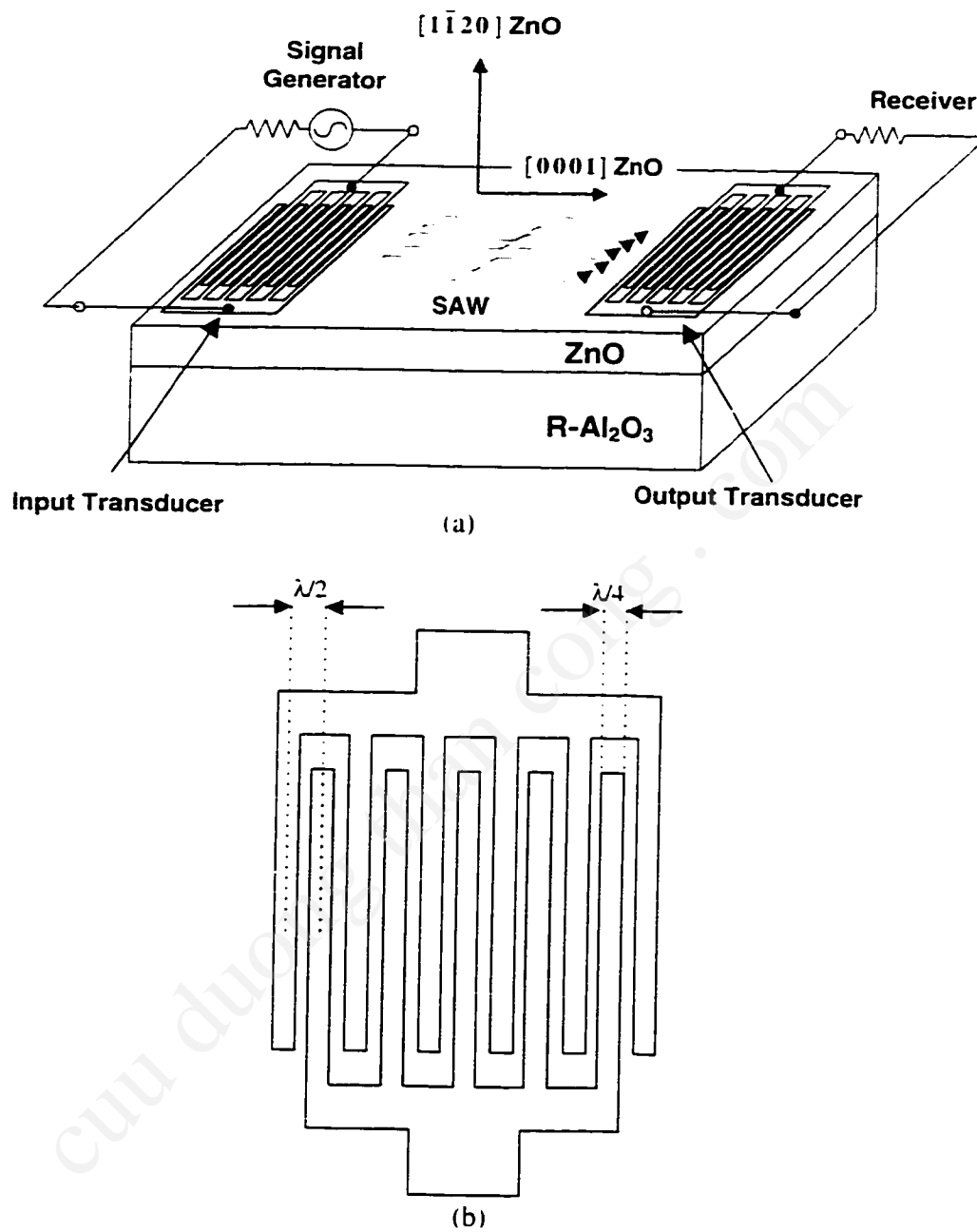


Figure 5-1: (a).Schematic diagram of a SAW filter fabricated on ZnO/R-Al₂O₃. The crystallographic directions in ZnO are shown. (b). Design parameters of the IDT.

5.1.2 SAW Device Fabrication

The as-grown ZnO films showed n-type conductivity with resistivity of the order of $1\ \Omega\text{-cm}$ to $10\ \Omega\text{-cm}$, and in order to achieve piezoelectricity (high resistivity), the films were doped with Li. LiCO_3 solution was coated onto the ZnO film by spin coating and allowed to dry. Then the wafer was annealed in an O_2 atmosphere at 690°C for ten hours so that Li could diffuse into the ZnO film and reach equilibrium. As suggested by Lander [40], initial diffusion of Li occurs through the interstitial sites, while under equilibrium conditions, Li occupies the Zn site. It has also been suggested that Li acts as an acceptor only when it substitutes for Zn in the Zn lattice (see section 2.2), and hence sufficient time has to be given for equilibration to occur in order to obtain high resistivities. The resistivity after doping was greater than 10^6 , which is sufficient to observe piezoelectric effects.

The IDTs were fabricated by a image reversal liftoff photolithographic technique. The basic steps (shown schematically in Figure 5-2) were:

- a. Spin coat negative photoresist and bake at 110°C
- b. Expose to UV radiation through a mask, followed by a bake at 110°C .
- c. Remove unexposed photoresist and expose to UV radiation a second time in order to improve the cross-linking in the photoresist.
- d. Depoist Al metal by e-beam evaporation.
- e. Dissolve the remaining photoresist. This process lifts-off the metal deposited on the photoresist.

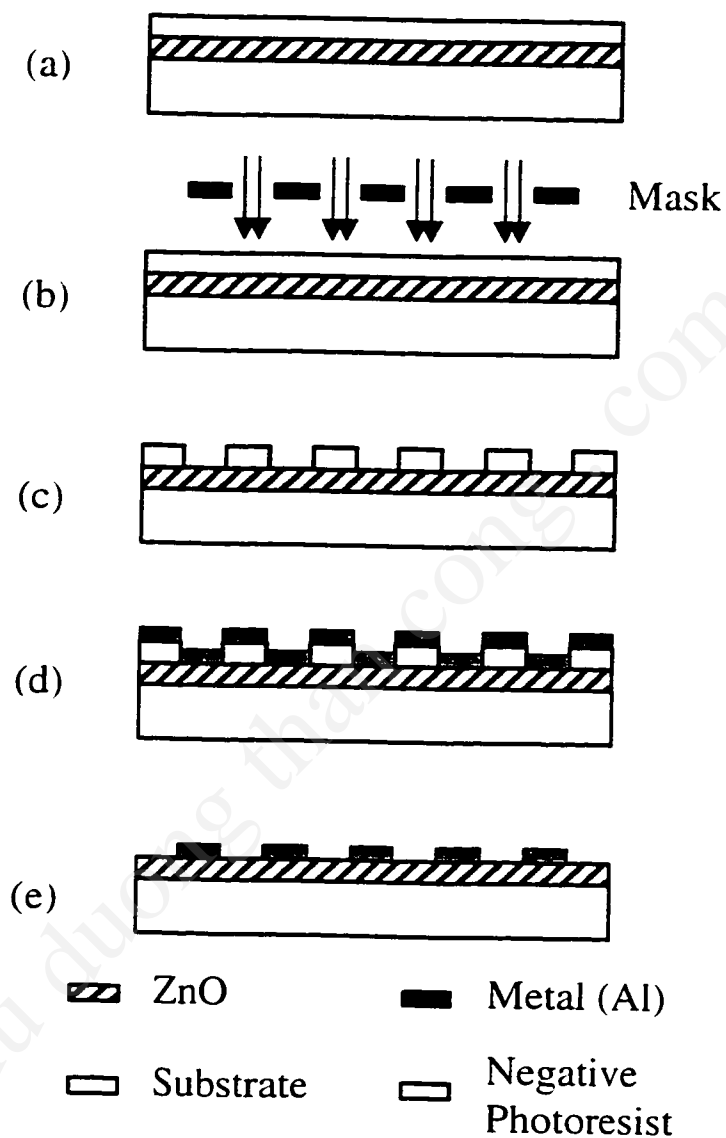


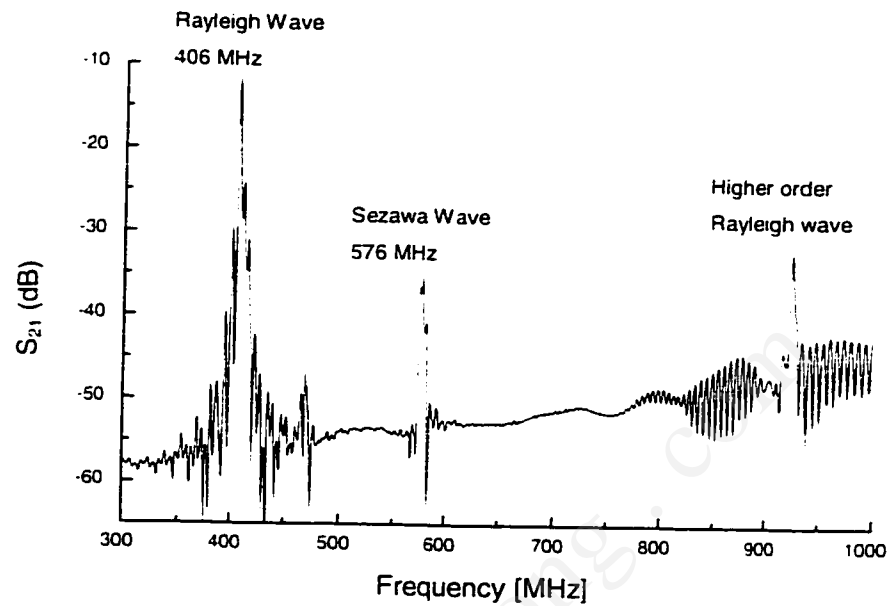
Figure 5-2: Schematic representation of the steps involved during the fabrication of the IDTs and the SAW devices. (a) deposit negative photoresist, (b) expose to UV radiation, (c) remove unexposed photoresist, (d) deposit metal, and (e) remove the remaining photoresist and the metal deposited on top of it.

All that remains is the metal lodged between the photoresist tracks. This is possible only if there is no continuity between the metal deposited on the surface of the ZnO film and that deposited on top of the photoresist. The advantage of the liftoff technique is that the ZnO film is not etched and hence there is no damage to the film, and any metal can be deposited onto ZnO by this technique

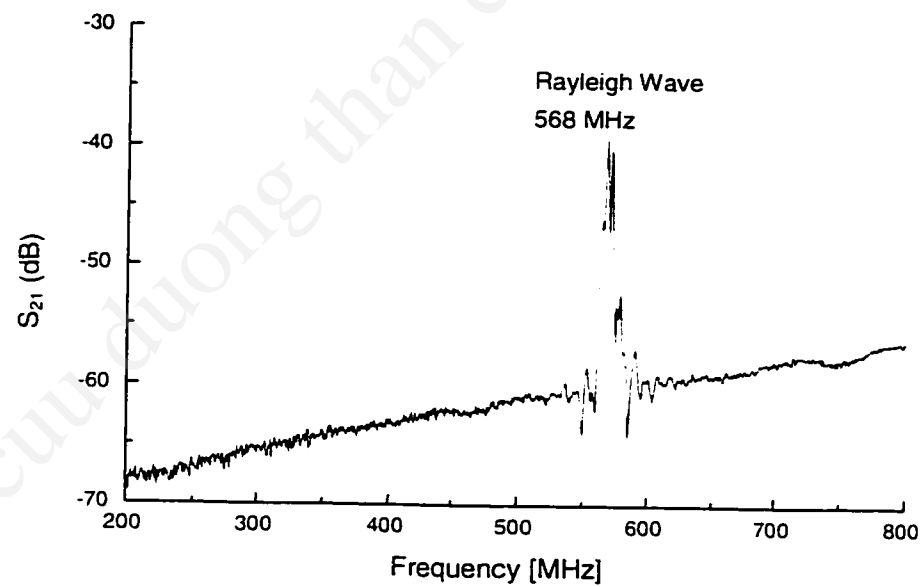
5.1.3 SAW Device Characterization

The characteristics of the SAW devices were evaluated with a setup that included a HP 8753D Vector Network Analyzer, a Cascade Microtech 9100 probe station, and Cascade Microtech Air Coplanar Probes for on-wafer testing.

The effective electromechanical coupling coefficient, k_{eff}^2 , was obtained by fitting Coupling-of Modes (COM) simulations⁶⁵ to the measured frequency spectrum of the SAW devices. The phase velocities are evaluated for SAW delay lines. The effective electromechanical coupling coefficients were determined for two sets of devices ($\lambda = 10 \mu\text{m}$ and $\lambda = 16 \mu\text{m}$) on ZnO films of thickness (h_{ZnO}) $0.5 \mu\text{m}$ and $1.5 \mu\text{m}$. Figure 5-3 shows the frequency spectrum of the $10 \mu\text{m}$ devices on the ZnO films of thickness $1.5 \mu\text{m}$ and $0.5 \mu\text{m}$ respectively. The center frequency is close to 420 MHz, resulting in velocity of the surface wave to be close to 4200 m/sec. The SAW properties for the devices are summarized in Table 5–2. The highest value of 6% for k_{eff}^2 is obtained for the $10 \mu\text{m}$ device on the $1.5 \mu\text{m}$ ZnO film. Table 5–2 shows that for the same λ , as h_{ZnO} decreases, the coupling coefficient decreases but the acoustic velocity increases.



(a)



(b)

Figure 5-3 (a) Frequency spectra of 10 μm device fabricated on 1.5 μm thick film

(b). Frequency spectra of 10 μm device fabricated on 0.5 μm thick film

The observed maximum effective coupling coefficient of 6% is close to that of bulk single crystal ZnO. The insertion loss of the devices fabricated on the 1.5 μm film was 11 dB, which includes a 6 dB loss due to the device design. This high coupling coefficient and low insertion loss result from the high crystal quality of the ZnO films, as well as a semi-coherent ZnO/R-Al₂O₃ interface. When a thin piezoelectric film, such as ZnO, is deposited on a nonpiezoelectric substrate with a higher acoustic velocity, such as Al₂O₃, the velocity of the surface wave propagating through this layered structure (ZnO + Al₂O₃) will lie between that of the individual surfaces of ZnO and Al₂O₃. The thickness-to-wavelength ratio, h/λ , is used to characterize the acoustic velocity. As h/λ increases, the velocity decreases. To obtain high frequency SAW filters, the thickness of the ZnO films has to be as small as possible. But the efficiency of electromechanical coupling between the input electrical signal and the generated surface acoustic wave decreases with decreasing ZnO film thickness. For a high-frequency and low-loss SAW device design, a trade-off between operating frequency and coupling coefficient has to be taken into account.

Table 5-2. SAW properties of the tested devices

$(h_{\text{Zn}}/\lambda)_{\text{nominal}}$	Wavelength (μm)	Acoustic velocity (m/s)	k^2 (%)	ZnO film thickness (μm)
0.03125	16	5768 - 5804	< 1	0.5
0.05	10	5562 - 5692	< 1	0.5
0.09375	16	4745 - 4927	3	1.5
0.15	10	4050 - 4200	6	1.5

In Table 5-3, the SAW properties of the $\text{ZnO}/\text{Al}_2\text{O}_3$ system are compared with some of the other material systems that are normally used. The ST cut of Quartz has a very low TCF, but has a very small electromechanical coupling coefficient. There are other cuts with $0.3\% k^2$, but unfortunately their TCF is not zero. Hence the ST cut is almost exclusively used in quartz devices. LiNbO_3 and LiTaO_3 crystals have a higher k^2 , but have inferior temperature characteristics. In addition, the attenuation constants are high for these cuts as the wave mode is leaky SAW or surface-skimming bulk waves (SSBW). Hence these substrates are not suitable for low-loss SAW filters as they have substantial propagation losses (attenuation). $\text{ZnO}/\text{R-Al}_2\text{O}_3$ displays a high electromechanical coupling coefficient as well as a high acoustic velocity. In addition, higher order Rayleigh waves, known as Sezawa waves, which have a higher acoustic velocity can be generated (Figure 5-3(a)), thus further increasing the operation frequency of SAW devices.

Table 5-3: Comparison of the SAW properties of various material systems

	Crystal Cut	k^2 (%)	TCF (ppm/°C)	v_{SAW} (m/sec)
$\text{ZnO}/\text{R-Al}_2\text{O}_3$	(11 $\bar{2}$ 0): plane, Z-prop	6	(-48)	4200
		1		5680
LiNbO_3	(128°)Y cut - X prop	5.5	(-75)	3980
	(64°)Y cut - X prop	11.3	(-70)	4742
LiTaO_3	X cut - 112° Y prop	0.75	(-18)	3290
	(36°)Y cut - X prop	5.0	(-32)	4160
Quartz	(42.75°)Y cut - X prop (ST cut)	0.16	0	3158

5.2 Optical Properties

5.2.1 Introduction

The refractive index of ZnO varies (with wavelength below the band gap) between 1.96 and 2.1⁴³ and it has a direct band gap (≈ 3.37 eV at room temperature) at the Γ position of the Brillouin Zone. The conduction band is predominantly s like, and the valence band is p like (6 fold degenerate). Splitting of the valence band (or removal of degeneracy) occurs due to two effects: (i) spin-orbit coupling and (ii) crystal-field splitting. The effect of the splitting on the band structure is shown in Figure 5-4.

(i) Spin-orbit coupling (Δ_{so}): An electron moving through an electric field, such as that of the periodic potential of the crystal lattice, experiences a potential proportional to the scalar product of its velocity and the electric field. This additional interaction is referred to as spin-orbit coupling. Spin-orbit coupling tends to remove the degeneracy of states with the same wavefunction but opposite spin. Spin-orbit coupling leads to a partial lifting of the valence band degeneracy by causing the formerly six fold degenerate valence band to be split into fourfold ($j = 3/2$) and twofold ($j = 1/2$) bands. In ZnO, the spin-orbit coupling is negative due to the negative contribution from the zinc d band in the valence band,^{113,114,115} which results in the $j = 1/2$ band to be at a higher energy than the $j = 3/2$ band.

(ii) Crystal field splitting (Δ_{cf}): Another type of perturbation occurs due to the interaction of the inner electron shells (d -shell in Zn) with the non-negligible electric field of the surrounding crystal lattice, which does not have a spherical symmetry but the symmetry of the crystalline site at which the ion is located. This is known as the Crystal Field Splitting, and results in the splitting of the valence band into Γ_5 and Γ_1 states.¹¹⁶

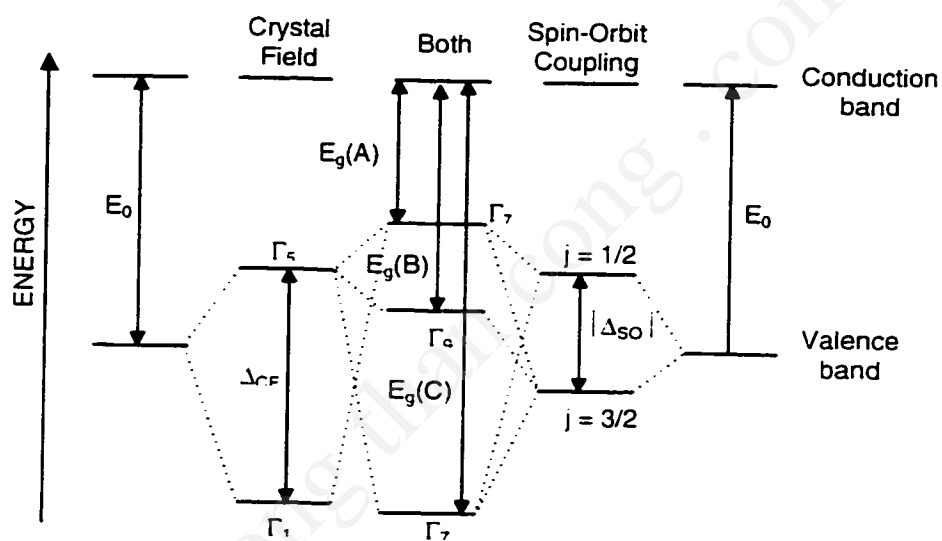


Figure 5-4 Schematic diagram of the valence band splitting due to spin-orbit coupling and crystal-field splitting in ZnO [118].

A combination of these two effects gives rise to three twofold degenerate valence bands, denoted as A (Γ_7 symmetry), B (Γ_9) and C (Γ_7). The energy gaps for these three bands are given in terms of E_0 (the average band gap), Δ_{so} and Δ_{cr} by the following expressions¹¹⁷:

$$\left. \begin{matrix} E_c(A) \\ E_c(C) \end{matrix} \right\} = E_0 + \frac{1}{6}(\Delta_{so} + \Delta_{cr}) \mp \frac{1}{2} \sqrt{\Delta_{so}^2 + \Delta_{cr}^2 - \frac{2}{3}\Delta_{so}\Delta_{cr}} \quad (5-1)$$

$$E_c(B) = E_0 - \frac{1}{3}(\Delta_{so} + \Delta_{cr}) \quad (5-2)$$

The values that have been reported (at 6 K) are¹¹⁸

$$\Delta_{so} = -3.5 \text{ meV}, \Delta_{cr} = 39.4 \text{ meV}, E_0 = 3.4553 \text{ eV}$$

$$E_g(A) = 3.441 \text{ eV}, E_g(B) = 3.4434 \text{ eV}, \text{ and } E_g(C) = 3.4817 \text{ eV}.$$

Free Excitons

A free hole in the valence band and a free electron in the conduction band can experience a coulombic attraction due to their opposite charges. Hence the electron can orbit about the hole as if this were a hydrogen-like atom. The ionization or binding energy for such a system is then

$$E_n = -\frac{m^* e^4}{32\pi^2 \hbar^2 \epsilon^2 n^2} = -\frac{e^2}{8\pi\epsilon r_h n^2} = -\frac{R(X)}{n^2} \quad (5-3)$$

where

$$m^* = \frac{m_e m_h}{m_e + m_h} \text{ is the reduced effective mass}$$

$$r_h = \frac{4\pi\epsilon \hbar^2}{e^2 m^*} \text{ is the effective first Bohr radius of the exciton}$$

$R(X)$ is the Rydberg constant of the exciton,

n is the exciton main quantum number.

e is the elementary charge of an electron

h is the planks constant,

ϵ is the dielectric constant, and

m_e and m_h are the effective masses of electrons and holes respectively.

Hence, the total energy for an excitonic transition is given by

$$E_{\epsilon} = E_g + E_n = E_g - R/n^2 \quad (5-4)$$

Each valence band has a series of excitons ($n = 1, 2, 3$ etc...). The binding energy for the A, B, and C free excitons in ZnO (6 K) have been found to be¹¹⁸

$$E_n(A) = 63 \text{ meV}, E_n(B) = 50 \text{ meV}, \text{ and } E_n(C) = 49 \text{ meV}.$$

The effective masses of the electron and holes have been estimated to be

$$m_e = 0.28 m_0 \text{ and } m_h = 0.59 m_0$$

where m_0 is the free electron mass.

Figure 5-5 shows the reflectance spectra (R) of polarized light ($E // c$ -axis and $E \perp c$ -axis) at 1.6 K from a ZnO single crystal which had its c -axis lying in the plane of the surface.¹¹⁹ As seen from Figure 5-5, the C series of exciton (C1, C2, C3 correspond to $n = 1, 2, 3$ respectively) is strongly excited when $E // c$, while the A and B series of excitons are excited when $E \perp c$. A consideration of the allowed optical transitions of the involved bands and the respective electric field vector of the perturbing light shows¹²⁰ that transitions with $E \perp c$ polarization are symmetry-allowed for the A, B and C bands, but the oscillator strength of the C band is small. $E // c$ transitions are forbidden for the B band, while they have a small oscillator strength for the A band and a large oscillator for the C band. Hence, the $E \perp c$ spectrum is dominated by the A and B bands while the C band dominates the $E // c$ spectrum.

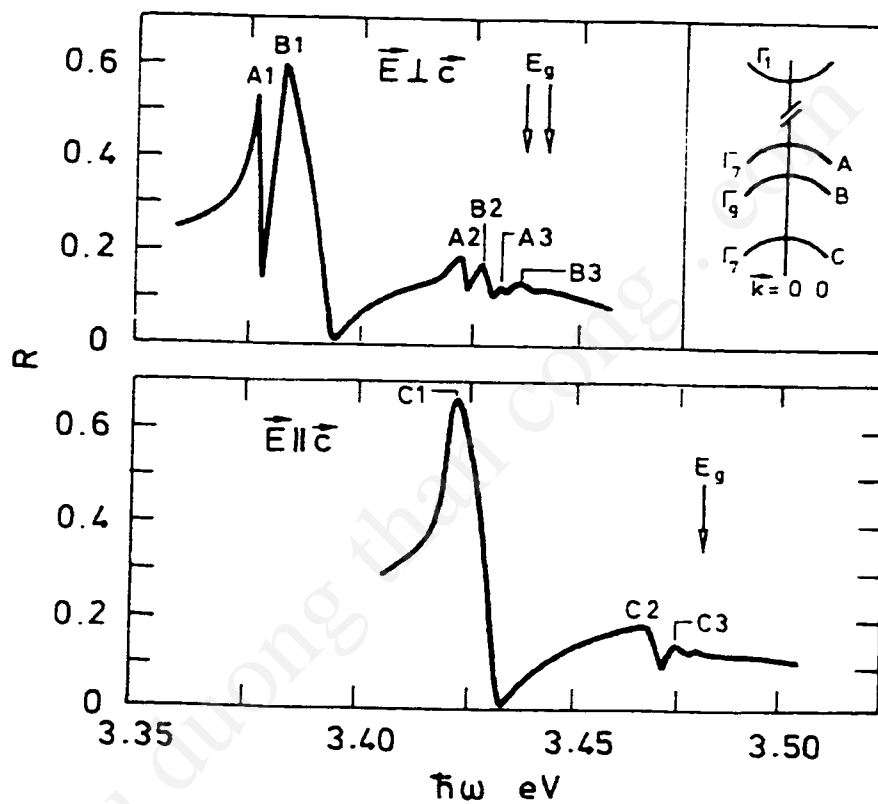


Figure 5-5 Reflectance spectra of ZnO at 1.6 K near the fundamental band gap.

(a) $E \perp c$ (b) $E \parallel c$. [119]

Bound Excitons

In the region of band–band transitions, the emission spectrum of ZnO is dominated by the recombination of bound-excitons, while weak lines are also present due to the free-excitons. Bound excitons are formed when a an isolated intrinsic or extrinsic defect in the lattice facilitates the binding of an exciton via coulombic forces. For example, a free hole can combine with a neutral donor to form a positively charged excitonic ion. In this case, the electron bound to the donor still travels in a wide orbit about the donor, while the associated hole moves in the electrostatic field of the donor–electron dipole. Electrons bound to neutral acceptors can also form bound excitons. The first type (hole-donor) are known as DX excitons, while the second type (electron-acceptor) are known as AX excitons. Emission or photoluminescence is a result of the collapse or recombination of excitons bound to the acceptors or donors. It has been found^{121,122} that optical transitions of bound excitons turn out to be preferentially polarized with $E \perp c$. Under the assumption that the eigenstates involved can be treated analogous to those of intrinsic excitons, the same relative oscillator strengths of transitions can be expected. Hence, in the emission spectra of ZnO, the hole states behave similarly to those of the A and B valence bands. Thus, strong anisotropy exists in the absorption and emission spectra of light from ZnO. The position of the DX and AX excitons has been found to be approximately 10 meV and 25–30 meV respectively below the A free exciton position at 4 K.¹²¹ Many lines due to excitons bound to impurities or dopants, which lie close to the free exciton line, have also been found.

5.2.2 Photoluminescence Characterization

Photoluminescence (PL) measurements were taken with 15 mW of excitation from an Ar⁺ laser. Figure 5-6(a) shows the room-temperature PL spectrum. The feature at 3.28 eV is due to band-edge recombination, while the broad feature at 2.35 eV (green emission) has been attributed by various authors to the recombination of free electrons with holes via interstitial zinc,¹²³ or via defects at grain boundaries (in polycrystalline ZnO investigated by cathodoluminescence).¹²⁴ Plasma hydrogenation has been found to passivate the green emission and enhance the band-edge recombination.¹²⁵ From Figure 5-6(a), the ratio of the integrated intensities of the band-edge emission to the deep level emission (broad band green emission) at room temperature is approximately 3:1. Similar results were observed from ZnO grown by MBE.¹²⁶

The low-temperature PL spectrum collected at 11 K is shown Figure 5-6(b). The peak at 3.363 eV is from donor-bonded exciton (D^0X) transition, while the feature at 3.320 eV is from the acceptor-bonded exciton transition. Note that the position of D^0X is in good agreement with 4 K PL result from bulk ZnO⁵ indicating that the thin film is almost strain free. The full width at half maximum of this feature is about 6 meV, compared to 3 meV (4.2 K) from bulk ZnO and 8.9 meV (4.2 K) from ZnO grown on GaN/SiC¹²⁶ by MBE, indicating a film of high quality.

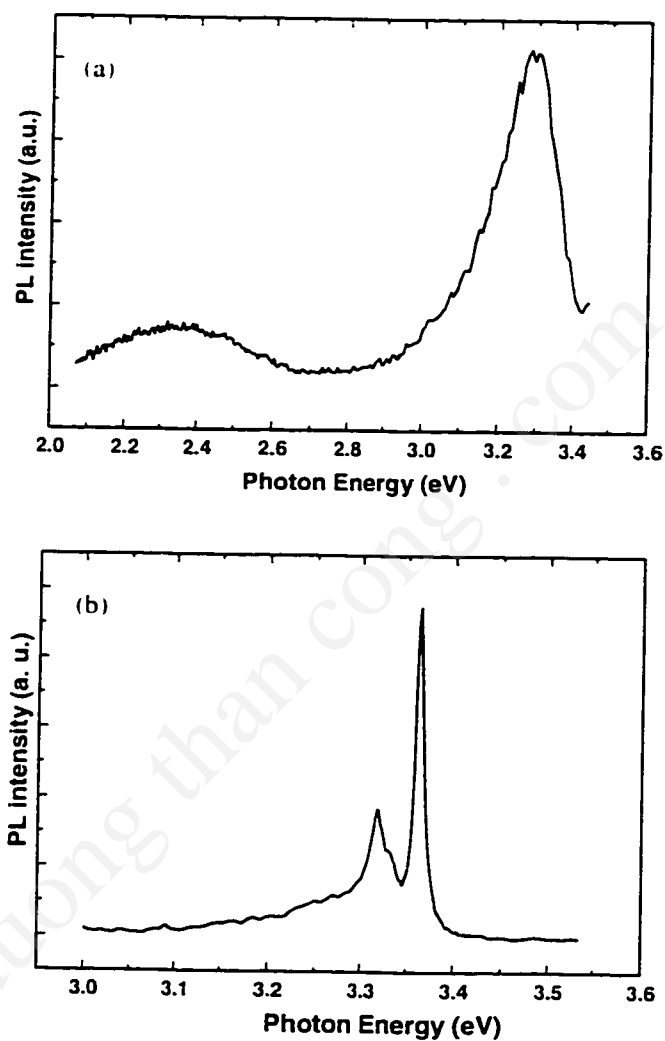


Figure 5-6 (a). Room temperature Photoluminescence from ZnO/R-sapphire and
(b). Photoluminescence from ZnO/ R-sapphire at 11 K.

5.2.3 Anisotropic Properties

In bulk single crystal ZnO, a strong optical anisotropy exists at near bandgap photon energies due to the different selection rules for light polarized parallel and perpendicular to the in-plane c -axis. In addition to PL, the anisotropic absorption properties of $(11\bar{2}0)$ oriented ZnO on $(01\bar{1}2)$ sapphire have been investigated.

Figure 5-7 shows the transmission T and reflectivity R of the ZnO film measured as a function of photon energy for light polarized parallel and perpendicular to the c -axis with a xenon arc lamp and monochromator. Although the shape of the transmission and reflectivity curves are similar for the two polarizations, the curves for $p//c$ are shifted by ~ 20 meV to higher energy with respect to those for $p\perp c$.

This phenomenon is primarily related to the anisotropy in absorption associated with the polarization selection rules and the effect of a thermally induced in-plane anisotropic strain, combined with the separation in energy of the C band from the A and B bands. The energy separation of A and B bands is unresolved at room temperature. From a linear fit to the square root singularity, we found that the separation between the A (B) and C bands is about 21 meV, which is significantly smaller than the separation of 40 meV measured from bulk ZnO at low temperature (1.6 to 4 K).

In the spectral region near the bandgap, higher photon energy transitions from the C-band to the conduction-band are preferred for light polarized parallel to the c -axis, while lower photon energy transitions from the A and B bands to the conduction band dominate for light polarized perpendicular to the c -axis.

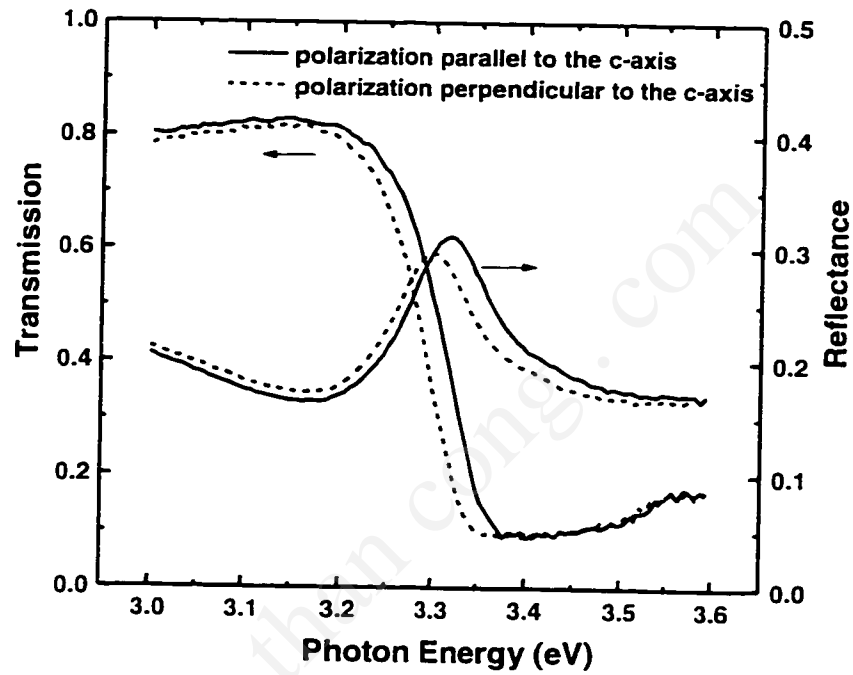
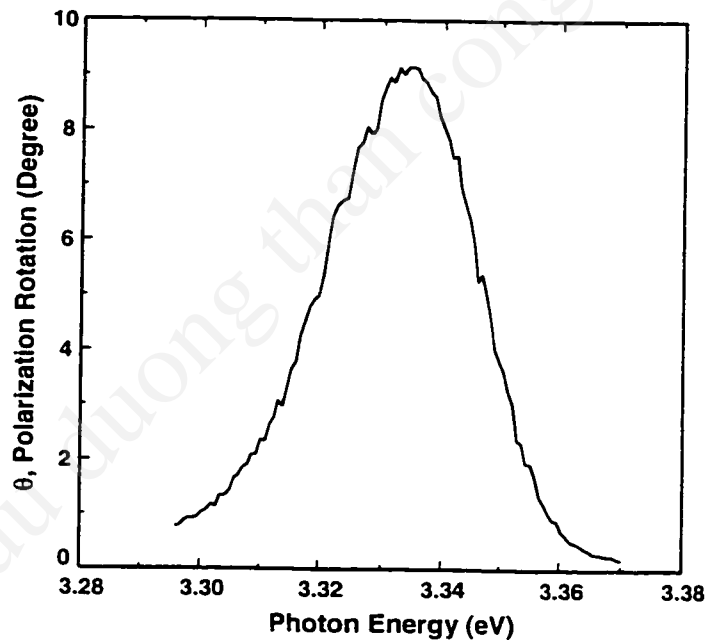
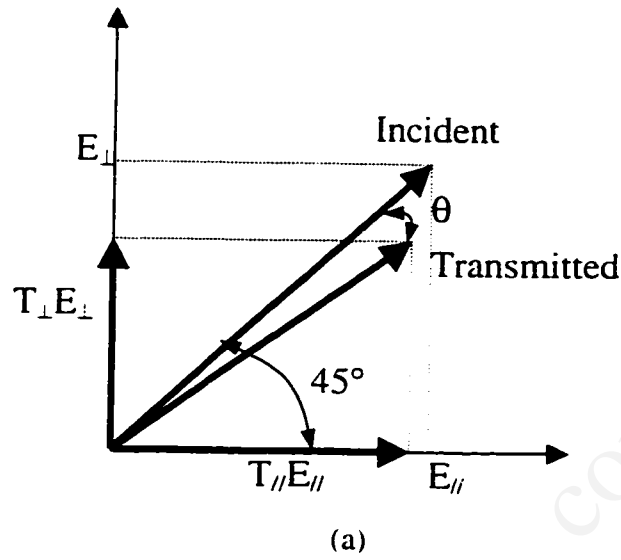


Figure 5-7 Transmission and Reflectivity of ZnO on R-plane sapphire as a function of photon energy for light polarized parallel (solid lines) and perpendicular (dashed lines) to the c-axis of the ZnO.

For normal incident light linearly polarized at 45° with respect to the c -axis, this leads to a polarization rotation toward the c -axis (Figure 5-8 (a)) given by the relation

$$\theta = \tan^{-1} [(T_{//} / T_{\perp})^{1/2}] - 45^\circ \quad (5-5)$$

where $T_{//}$ and T_{\perp} are the transmission for $p//c$ and $p\perp c$, respectively. Figure 5-8(b) shows this 'static' polarization rotation as a function of photon energy. A maximum rotation of 10° occurs at 3.335 eV. This rotation was used to demonstrate a high-contrast, high-speed ultraviolet light modulator.⁵¹



(b)

Figure 5-8 (a). Schematic diagram showing the effect of the anisotropic transmission properties of ZnO on the polarization

(b) Polarization rotation as a function of photon energy for normal incident light linearly polarized at 45° with respect to the c-axis.

Chapter 6 : THERMAL STABILITY OF ZnO/R-Al₂O₃

In applications involving high temperatures, such as in the use as buffer layers for III–Nitride growth by MBE, the thermal stability of the ZnO films is extremely important. In addition, the chemical stability against etching and reaction with the gaseous phase (with NH₃, Triethyl Gallium etc.,) is also important in the case of III–Nitrides growth by reactive MBE¹²⁷ or MOCVD.²⁵ High temperature annealing is also a means of improving the crystalline quality of the films and hence the upper limits for annealing, with out degradation of the film occurring, have to be established. The ZnO/R–Al₂O₃ system was chosen as it possesses anisotropic properties for various important applications, such as acousto-optic,⁴⁴ optical modulator,⁵¹ and piezoelectric/surface acoustic wave (SAW) devices.^{65, 77}

In addition to the technological importance of the annealing characteristics of ZnO, the reaction between ZnO and Al₂O₃ is also important scientifically. Reactions between oxides of the form AO and B₂O₃, resulting in the formation of BA₂O₄, have been model systems for studying the mechanisms involved during reactions between ionic solids. Utilizing irreversible thermodynamics and point defect theory, the basic mechanism involved has been established¹²⁸ as one where the counter diffusion of cations occurs to maintain charge neutrality, while the anions (oxygen ions) are immobile. Three sequential steps are envisioned: (1) counter diffusion of cations through the reaction product (AB₂O₄), (2) reaction of B ions with AO at the AO/AB₂O₄ interface, and (3) reaction of A ions with B₂O₃ at the B₂O₃/AB₂O₄ interface. When the diffusion of one

or both cationic species is rate controlling, a parabolic growth rate is observed, while a linear growth rate is observed if the reaction is interface controlled.¹²⁹

As observed in the NiO/Al₂O₃ system, the growth rate and mechanism is dependent on the orientation relationship between the two reactants.¹³⁰ Thin film reactions i.e. reactions between a substrate and a deposited epitaxial thin film are useful as they reduce the number of variables such as presence of oxygen (gas) at the reaction interfaces and multiple orientations of the reactants. Considerable work has been carried out in the NiO/Al₂O₃¹³⁰ and MgO/Al₂O₃¹³¹ systems and formation of other spinels such as MgFe₂O₄¹³⁰, MgCr₂O₄¹³², FeCr₂O₄¹³², and MgIn₂O₄¹³³ have also been studied. It has been shown¹³⁰ that while reaction between NiO on (01 $\bar{1}$ 2) Al₂O₃ is diffusion controlled, the reaction between NiO on (0001) Al₂O₃ is interface controlled. The interface control of the growth rate can occur either due to the effect of step heights on growth fronts, as has been found during the growth of NiS₂ on Si¹³⁴, or due to the glide or climb of misfit dislocations at the interface.^{133,135}

In the ZnO/Al₂O₃ system, the oxygen sublattice has to rearrange itself from an hcp to an fcc arrangement at each of the reaction fronts. By contrast, in the NiO/Al₂O₃ and MgO/Al₂O₃ systems, the rearrangement of the oxygen sublattice occurs only at a single interface (spinel/sapphire). Thus, differences are expected in the behavior of the ZnO/Al₂O₃ system when compared with the other two systems. In addition to the scientific interest in the ZnO/Al₂O₃ system, Reaction between ZnO and Al₂O₃ powders has shown that the early stages of ZnAl₂O₄ formation follows a linear rate law¹³⁶, but at later stages a parabolic rate law has been reported.^{136,137}

To ascertain the controlling mechanism, a thin film reaction couple, epitaxial $(11\bar{2}0)$ ZnO on $(01\bar{1}2)$ Al_2O_3 was used in the present study. The ZnO films were deposited by MOCVD, and their structure and epitaxial relationship determined by x-ray diffraction and cross sectional transmission electron microscopy. The epitaxial relationships between the product phase (ZnAl_2O_4) and the reactants, and the structure of the spinel layer is evaluated using cross sectional TEM. It was found that when measuring growth rates, measurements have to be taken from grains of the same orientation and far away from grain boundaries. The growth rate at the initial stages of reaction is measured and the structures of the ZnO/ ZnAl_2O_4 and $\text{ZnAl}_2\text{O}_4/\text{Al}_2\text{O}_3$ interfaces are investigated.

6.1 Introduction to solid state reaction kinetics

Heterogeneous solid state reactions occur when two phases, A and B, react to form a product C. The characteristic feature of this type of reaction is that the product C separates the reactants A and B, and that growth of C proceeds by the transport of A and/or B through the product layer. The driving force for such a reaction is the difference in the Gibbs free energy between the reactants and the reaction product. The kinetics of the reaction are determined by

- (a). the speed of diffusion of the reactant species through the product layer, and
- (b). by the rate of reaction at the interfaces.

Some of the factors that affect the reaction rates at interfaces are discussed below.

Interfaces between dissimilar materials or phases involves either a change in composition or a change in structure and symmetry across the boundary. There could be additional effects such as coherency strains, misfit dislocations, and electrostatic effects

in the case of ionic materials and semiconductors. All these aspects of an interface can affect the dynamics of a moving boundary or the kinetics of a reaction occurring at the boundary.

Interfaces are associated with an extra energy compared with the bulk since there is symmetry breaking. Hence, there is a barrier or resistance for mass transport across the interface, which has to be overcome by thermally activated processes.

In addition to a higher energy due to symmetry breaking as in the case of metallic interfaces, interfaces in ionic crystals may also carry an electric charge resulting from the presence of excess ions of one sign. This charge must then be compensated for by a space-charge region of the opposite sign adjacent to the boundary, which can have a significant effect in the transport of ionic species across the interface.

If misfit dislocations are present at an interface, the dislocations must move along with the interface during the course of a reaction. The dislocations can move either by glide or by climb. Whether the dislocations will glide depend on their Burgers vectors and the presence of glide planes. Climb of dislocations involves the diffusional transport of vacancies and ions, and is therefore slow and strongly temperature dependent.

Taking all these aspects into consideration, an interface/boundary acts as a series resistance for the transport of matter perpendicular to the boundary, and can be rate determining if it is greater than the bulk (diffusional) resistance. Interface-controlled kinetics then means that if matter crosses the interface, there must occur thermally activated processes which are definitely slower than diffusional transport in the bulk.

Before we proceed to look at the theory behind diffusion- or interface-controlled reactions, some of the basic concepts regarding diffusion in ionic solids and some of the assumptions made for studying solid state reactions are discussed.

(a). Diffusion or transport in solids occurs due to the presence of point defects such as vacancies or interstitials wherein atoms (or ions) move by thermally activated jumps into vacant sites. The equilibrium concentrations of these defects combined with the frequency of the thermally activated jumps, both of which depend on the temperature, will determine the diffusion rate.

(b). The defect notation S_M^x , of Kroger and Vink²⁹ is employed, wherein the principle symbol (S) represents the species occupying the site M (A for a site in the A sublattice, i for an interstitial position etc.,). The superscript represents the charge of the species *relative to normal site occupancy* with a prime indicating a negative, a dot representing a positive, and a cross zero charge.

(c). A small fraction of atoms, by virtue of the entropy gain, dissociate from their regular sites into the interstitial lattice. These are known as Frenkel defects¹³⁸, and their formation mechanism (species A in an ionic solid AO) can be written as



Schottky defects¹³⁹ are matched anion and cation vacancies which are formed according to the mechanism



In the absence of free carriers (electrons or holes), the interstitial cation and the vacancy in the case of a Frenkel defect or the cation and anion vacancies in the case of a Schottky

defect have to occur in pairs. The complications introduced by association (pairing) of ions and vacancies have been discussed by Howard and Lidiard.¹⁴⁰

(d). Using the phenomenological theory of diffusion¹⁴¹, the diffusional flux (j_i) of a species in the presence of a chemical potential gradient ($\nabla\mu_i$) is given by:

$$\begin{aligned} j_i &= L_i X_i = -L_i \nabla\mu_i = -\frac{D_i c_i}{RT} \frac{d\mu_i}{dx} = -D_i c_i \frac{d \ln \gamma_i N_i}{dx} \\ &= -D_i \left[1 + \frac{d \ln \gamma_i}{d \ln c_i} + \frac{d \ln V_m}{d \ln c_i} \right] \frac{dc_i}{dx} \end{aligned} \quad (6-3)$$

where L_i is a transport coefficient,

X_i is a generalized driving force,

D_i is the diffusion coefficient of species i ,

c_i is the concentration of species i ,

γ_i is the activity coefficient, and

V_m is the molar volume of the diffusing species 'i'

The driving force is the decrease in the Gibbs free energy, which for an isothermal and adiabatic system is equal to the change in the chemical potential.

For ideal dilute solutions with constant activity coefficients γ_i , the above equation reduces to Fick's first law:

$$j_i = -D_i \frac{dc_i}{dx} \quad (6-4)$$

In ionic systems which contain electrically charged particles with charge $z_i \cdot e_0$, and in the presence of an electrical potential ϕ , the chemical potential has to be replaced by the electrochemical potential

$$\eta_i = \mu_i + z_i F \phi \quad (6-5)$$

where F is the faraday constant.

Due to the close packed nature of the anions (O^{2-}) in $ZnAl_2O_4$ (and in most oxides) and due to their larger size compared to the cations (Al^{3+} and Zn^{2+}), the diffusion rates for O^{2-} are very low. Hence during solid state reactions, we will consider the diffusion of cations in a lattice with immobile anions. In the absence of any mobile electrons or holes (insulator), the diffusion of Al^{3+} and Zn^{2+} will be coupled in order to maintain local charge neutrality. Hence the reaction rate will be determined by the slower diffusing species.

(e). Transport across boundaries:

If a boundary or interface creates a resistance for mass transport across it, there will be a drop in chemical potential or concentration across the interface. The structure of the phase boundary is determined by the two bordering phases, and if these phases do not change during the reaction, except to alter their dimensions, it can be seen that the resistance of the phase boundary to the passage of particles is a constant. In such a situation, a part of the Gibbs energy (ΔG_{AB}) available in a solid state reaction is dissipated at the phase boundaries (ΔG^b). The flux across an interface can be described phenomenologically as

$$j_i = \lambda_i \delta\mu_i = j_i^0 \frac{\delta\mu_i}{RT} \quad (6-6)$$

where $\delta\mu_i$ is the change in chemical potential across the boundary, and

λ_i is the interface conductance, and

j_i^0 is the equilibrium exchange flux.

At equilibrium, there are equal fluxes of species i crossing the boundary in opposite directions, resulting in a net zero flux. The equilibrium exchange flux is defined as this value of flux in any one direction. The above equation is based on the assumption that the interface conductance of an interface is a constant, which results in the potential drop across the boundary to be proportional to the flux. This assumption is usually valid, since the structure of the boundary remains a constant as the reaction proceeds, and so the interface conductance can be assumed to be constant.

(f). Relaxation (rearrangement) of species after crossing the boundary:

As mentioned earlier, the species diffuse predominantly by interstitial diffusion. Once the species cross the boundary they have to move from the interstitial positions into the lattice sites which they would occupy in the reaction product at equilibrium. For example, in the case of a reaction between A and B forming AB, the A species would cross the AB/B boundary and occupy the interstitial sites in B. Subsequently, the A species interact with B forming AB, during which A has to move from the interstitial sites to the appropriate equilibrium sites in AB. This relaxation process can be rate controlling if the relaxation time (τ_R) is sufficiently slow. This effect can be grouped with the boundary effects when discussing reaction kinetics.

Let us consider a simple example of two reactants A and B reacting to form AB. For simplicity we will make the assumption that $D_A \gg D_B$, and study the transport of A ions across the product layer AB, and the interface reaction of these ions at the AB/B interface. The total available driving force for any reaction is the change in Gibbs free energy, ΔG_{AB} . ΔG^b is the fraction of the Gibbs free energy is dissipated at the interface. If

$\Delta\mu_A(AB)$ and $\Delta\mu_A^b$ are the change in chemical potentials across the product layer and across the boundary respectively (see Figure 6-1(c)), then

$$\Delta G_{AB} = \Delta\mu_A(AB) + \Delta\mu_A^b \quad (6-7)$$

The steady state condition requires that the diffusional flux entering the boundary, j_A , should be equal to the flux across the boundary. Hence

$$j_A = \frac{D_A c_A}{\Delta x(AB)} \frac{\Delta\mu_A(AB)}{RT} = j_A^0 \frac{\Delta\mu_A^b}{RT} \quad (6-8)$$

where $\Delta x(AB)$ is the thickness of the product layer. Defining a length scale

$$\Delta x' = \frac{D_A c_A}{j_A^0} \quad (6-9)$$

We obtain from the above equation

$$\frac{\Delta x'}{\Delta x' + \Delta x(AB)} = \frac{\Delta\mu_A^b}{\Delta G_{AB}} = \frac{\Delta\mu_A^b}{\Delta\mu_A^b + \Delta\mu_A(AB)} \quad (6-10)$$

For $\Delta x(AB) \rightarrow 0$, $\Delta\mu_A^b = \Delta G_{AB}$, and the reaction is interface controlled. If $\Delta x(AB) \gg \Delta x'$, then $\Delta\mu_A^b \rightarrow 0$, and the reaction is controlled by diffusion through the product AB. For very small product layer thickness, the diffusional resistance of the product layer is negligible, and the discontinuity in the activity at the phase boundary takes on the maximum value that is thermodynamically possible (Figure 6-1(b)). As the thickness of the product layer increases, the diffusional resistance of this layer continually increases relative to the phase boundary resistance. The particle flux and the activity change across the boundary become smaller until, finally, a state of local equilibrium is achieved at the phase boundary and the discontinuity in activity virtually disappears (Figure 6-1(a)).

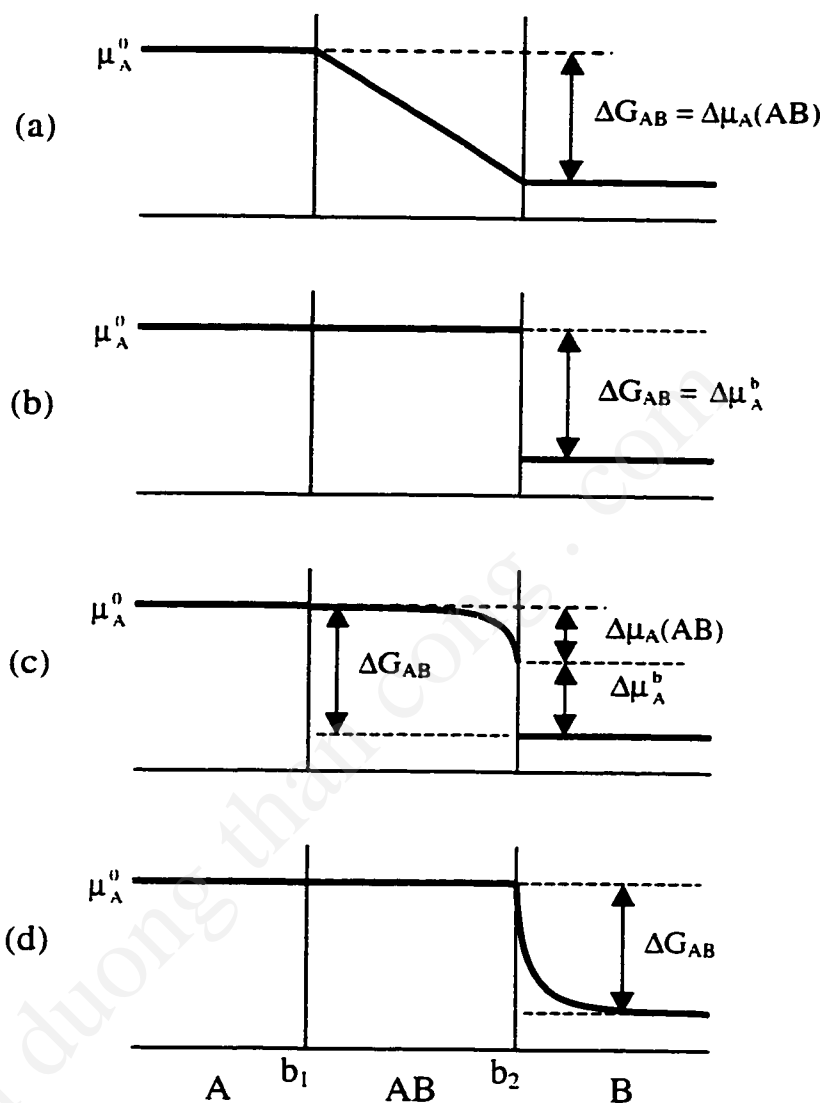


Figure 6-1: Schematic representation of the variation of the chemical potential of A during the solid state reaction $A + B = AB$. (a). Diffusion controlled (b). Interface controlled (c). Simultaneous interface and diffusion controlled (d) rate control by rearrangement (relaxation) of A in B. [129]

Figure 6-1(d) corresponds to the situation when the relaxation of rearrangement of the species determines the rate of the reaction

Let us derive a simplified equation for the growth rate of the product under mixed control. Here we consider the concentration gradients in the product layer and across the boundary instead of the chemical potential changes. Let the concentration of the diffusing species (A ions) be C_0 at the A/AB interface, C_1 the concentration on the product side of the AB/B interface and C_2 the concentration across the boundary. The diffusional flux entering the boundary is

$$j_A = D_A \frac{dc}{dx} = D_A \frac{\Delta c}{\Delta x} \approx D_A \frac{(C_0 - C_1)}{x} \quad (6-11)$$

where x is the thickness of the product layer and a dilute solution is assumed.

Simultaneously, the flux crossing the boundary can be written as

$$j_A = \lambda (C_1 - C_2) \quad (6-12)$$

where λ is the interface transfer coefficient or conductance. At steady state these fluxes should be equal to each other, we can obtain

$$j_A = (C_0 - C_2) \left(\frac{x}{D_A} + \frac{1}{\lambda} \right)^{-1} \quad (6-13)$$

by substituting $(C_1 - C_2) = (C_0 - C_2) - (C_0 - C_1)$ in equation (12) for the flux across the boundary. If V_m is the molar volume of the product AB is V_m per ion of A, then the growth rate is

$$\frac{dx}{dt} = j_A V_m = V_m \frac{(C_0 - C_2)}{\left(\frac{x}{D_A} + \frac{1}{\lambda} \right)} \quad (6-14)$$

Integrating, we get

$$\frac{x^2}{2D_A} + \frac{x}{\lambda} = V_m(t - t_0) \quad (6-15)$$

The second term (linear rate constant) dominates when the thickness of the layer is small and the first term (parabolic rate law) dominates at larger thickness.

6.2 RESULTS AND DISCUSSION

The films were annealed in a tube furnace in an O₂+N₂ ambient at atmospheric pressure. The epitaxial relationship between the as-grown ZnO film and R-sapphire was evaluated using a combination of X-Ray diffraction θ - 2θ scans, ϕ -scans and electron diffraction. The ZnO/Al₂O₃ interface was also studied by cross-sectional High Resolution Transmission Electron Microscopy (HR-TEM). A combination of High Resolution TEM imaging, Selected Area Electron Diffraction and Convergent Beam Electron Diffraction were used to characterize cross-sections of the films after annealing. Cross-sectional samples were prepared by gluing two samples face to face using M-Bond 610 epoxy, followed by mechanical thinning to < 10 μ m and ion-milling to electron transparency. A Topcon 002B 200 kV electron microscope was used.

6.2.1 REACTION KINETICS

ORIENTATION RELATIONSHIPS

As shown in Section 4.1, the epitaxial relationship between ZnO grown on (01 $\bar{1}$ 2) plane of sapphire is:

$$(11\bar{2}0) \text{ ZnO} // (01\bar{1}2) \text{ Al}_2\text{O}_3 \text{ and } [0001] \text{ ZnO} // [0\bar{1}11] \text{ Al}_2\text{O}_3.$$

According to this epitaxial relationship, the c-axis of ZnO lies in the plane of the film and in a plane (perpendicular to the surface) which also contains the c-axis of Al₂O₃ (which

makes an angle of 32° with the surface. From X-ray and cross-sectional TEM studies, no other orientation relationships were observed.

The films were annealed in an O_2+N_2 atmosphere at 1000°C for 30, 90 and 150 minutes. From cross-sectional TEM analysis, $ZnAl_2O_4$ was observed to form along the entire ZnO/Al_2O_3 interface in all samples. A TEM image of the spinel layer from the sample annealed for 150 min is shown in Figure 6-2.

Multiple epitaxial relationships were observed between the spinel grains formed and the Al_2O_3 and ZnO layers. The epitaxial relationship of one type of grains that were observed in all samples was studied in more detail. The diffraction patterns in mutually perpendicular directions are shown in Figure 6-3(a) (from sample annealed for 150 min) and Figure 6-3(b) (from sample annealed for 90 min). The diffraction pattern in Figure 6-3(a) is taken while viewing along the c-axis of ZnO , i.e. in the $[0001]$ zone axis of the ZnO film. Figure 6-3(b) is taken along the $[\bar{1}100]$ zone axis of ZnO . From Figure 6-3(a), the $(\bar{1}31)$ plane of $ZnAl_2O_4$ makes an angle of $\approx 3.5^\circ$ (clockwise rotation) with the $(\bar{1}100)$ plane of ZnO or the $(2\bar{1}\bar{1}0)$ plane of Al_2O_3 . Moreover the crystal is tilted by $\approx 2^\circ$ as calculated from the radius of the laue circle of the $[11\bar{2}]$ zone axis. In Figure 6-3(b), the reflections from the First Order Laue Zone (FOLZ) of the $[\bar{1}31]$ zone are closest to the transmitted spot, and the center of the zone makes an angle $\approx 3.5^\circ$ with the $[\bar{1}100]$ zone of ZnO . This confirms the tilt observed in Figure 6-3(a). Also, the $(11\bar{2})$ plane makes an angle of $\approx 2^\circ$ with the (0001) plane of ZnO , again verifying the tilt observed in Figure 6-3(a).

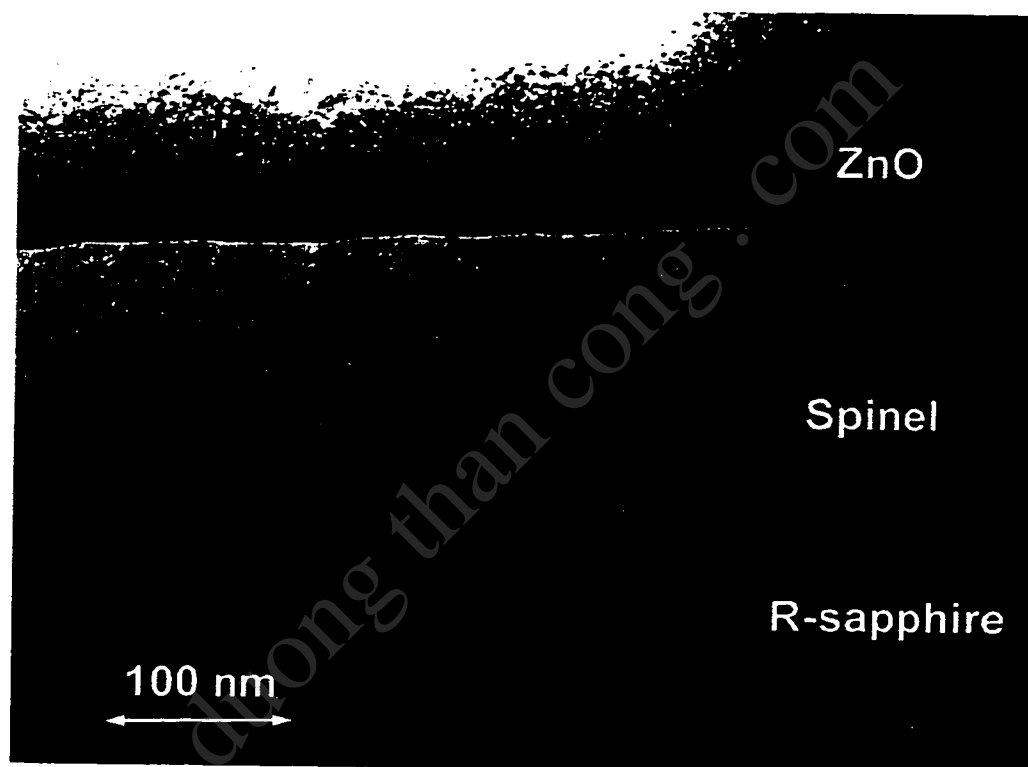


Figure 6-2: Image of the spinel layer between ZnO and R-plane sapphire. The sample was annealed at 1000°C for 150 min.

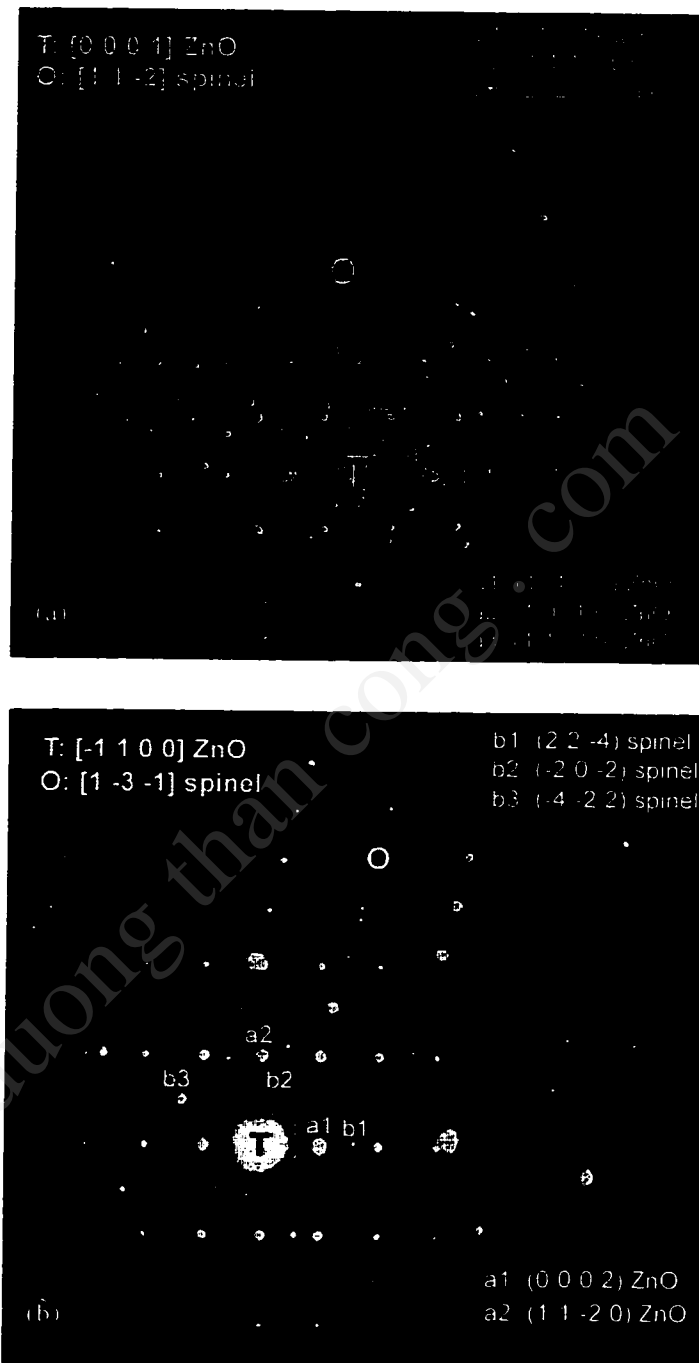


Figure 6-3 (a). Diffraction pattern of ZnO + spinel viewed along the $[0001]$ axis of ZnO.

(b). Diffraction pattern of ZnO + spinel viewed along the $[\bar{1}\ 1\ 00]$ axis of ZnO.

Hence, the epitaxial relationship between this orientation of ZnAl_2O_4 and ZnO is

$(\bar{1}31)\text{ZnAl}_2\text{O}_4$ makes a 3.5° angle with $(1\bar{1}00)\text{ZnO}$; and $[11\bar{2}]\text{ZnAl}_2\text{O}_4$ makes a 2° angle with $[0001]\text{ZnO}$.

We can also represent the epitaxial relationship between Al_2ZnO_4 and Al_2O_3 as

$(\bar{1}31)\text{ZnAl}_2\text{O}_4$ makes a 3.5° angle with $(2\bar{1}\bar{1}0)\text{Al}_2\text{O}_3$; $[11\bar{2}]\text{ZnAl}_2\text{O}_4$ makes a 2° angle with $[0\bar{1}11]\text{Al}_2\text{O}_3$

In this orientation, the $(2\bar{2}0)$ plane in ZnAl_2O_4 is parallel to the $(\bar{1}101)$ plane in Al_2O_3 . This tilt was consistently observed in different samples

Another orientation, similar to the above, with a $\approx 5^\circ$ rotation (counter clock wise) about the $[11\bar{2}]$ zone axis was observed. This rotation results in the $(2\bar{2}0)$ plane in ZnAl_2O_4 to be parallel to the $(\bar{1}2\bar{1}0)$ plane in ZnO , which is equivalent to the (111) plane in ZnAl_2O_4 to be parallel to the $(10\bar{1}0)$ plane in ZnO . As a comparison, NiAl_2O_4 on R-sapphire is observed to grow with its $(\bar{1}31)$ plane parallel to the $(2\bar{1}\bar{1}0)$ plane of Al_2O_3 , but with the $[11\bar{2}]$ direction parallel to the $[0001]$ direction of Al_2O_3 .¹³⁰ The epitaxial relationships mentioned above along with three others that were observed are tabulated in Table 6-1.

The reaction couple $\text{ZnO}/\text{Al}_2\text{O}_3$ has oxygen sublattices that are both h.c.p and hence is different from the reaction couples $\text{NiO}/\text{Al}_2\text{O}_3$ and $\text{MgO}/\text{Al}_2\text{O}_3$. When ZnAl_2O_4 is formed, rearrangement of the oxygen sublattices from hcp to fcc has to occur at both the reaction fronts, as compared to only at the Al_2O_3 reaction front in the other two systems. In the later two systems, it has been found that the spinel follows the cube-on-cube epitaxial relationship with respect to NiO or MgO , i.e. the orientation of the spinel

lattice follows the orientation of NiO or MgO. Due to the different structures, this does not occur in the present system. In the (0001) ZnO/(0001) Al₂O₃ system, ZnAl₂O₄ grows with its close packed (111) planes parallel to the close packed (0001) planes of Al₂O₃ and ZnO. There is no such simple relationship between the planes of ZnAl₂O₄ and (01 $\bar{1}$ 2) Al₂O₃ or (11 $\bar{2}$ 0) ZnO. Hence, the more than one epitaxial relationships observed in this case can be expected because there is no simple template for the spinel to follow.

Table 6-1: Observed epitaxial relationships between ZnAl₂O₄ and ZnO/Al₂O₃

A	($\bar{1}$ 31)ZnAl ₂ O ₄ makes a 3.5° angle with (2 $\bar{1}$ $\bar{1}$ 0) Al ₂ O ₃ (or) (2 $\bar{2}$ 0) ZnAl ₂ O ₄ // ($\bar{1}$ 101) Al ₂ O ₃	[11 $\bar{2}$]ZnAl ₂ O ₄ makes a 2° angle with [0 $\bar{1}$ 11]Al ₂ O ₃
B	($\bar{1}$ 31)ZnAl ₂ O ₄ makes a -1.5° angle with (2 $\bar{1}$ $\bar{1}$ 0) Al ₂ O ₃ (or) (2 $\bar{2}$ 0) ZnAl ₂ O ₄ // ($\bar{1}$ 2 $\bar{1}$ 0) ZnO (or) (111)ZnAl ₂ O ₄ // (10 $\bar{1}$ 0) ZnO	[11 $\bar{2}$]ZnAl ₂ O ₄ // [0 $\bar{1}$ 11]Al ₂ O ₃
C	(111)ZnAl ₂ O ₄ // (10 $\bar{1}$ 0) ZnO	[$\bar{2}$ $\bar{1}$ 3]ZnAl ₂ O ₄ // [0 $\bar{1}$ 11]Al ₂ O ₃
D	(011)ZnAl ₂ O ₄ // (11 $\bar{2}$ 0) ZnO (or) (011)ZnAl ₂ O ₄ // (01 $\bar{1}$ 2)Al ₂ O ₃	[4 $\bar{3}$ 3]ZnAl ₂ O ₄ // [$\bar{2}$ 110]Al ₂ O ₃ (or) [32 $\bar{2}$]ZnAl ₂ O ₄ // [0 $\bar{1}$ 11]Al ₂ O ₃
E	(13 $\bar{3}$)ZnAl ₂ O ₄ makes a 5° angle with (11 $\bar{2}$ 0) ZnO	[022]ZnAl ₂ O ₄ makes a 5° angle with [0 $\bar{1}$ 11]Al ₂ O ₃

As mentioned earlier, there are similarities between the orientation 'A' (in Table 6-1) of ZnAl₂O₄ on R-Al₂O₃ and the orientation of NiAl₂O₄ on R-Al₂O₃. Since the only common factor in these two cases is the sapphire substrate, we can assume that the substrate orientation plays an important part in determining the epitaxial relationship. Therefore, we should take a closer look at the relationship between orientation 'A' of ZnAl₂O₄ and R-Al₂O₃. Schematic diagrams of the spinel along its [11 $\bar{2}$] direction, and

that of $R\text{-Al}_2\text{O}_3$ along its $[0\bar{1}11]$ direction are shown in Figure 6-4. Only the oxygen sublattice of ZnAl_2O_4 is shown and the small tilts observed are neglected. Two planes are shown: the (714) plane which is perpendicular to the $(\bar{1}31)$ planes, and the (513) plane which makes an angle of 87° with the $(\bar{1}31)$ planes. The position of the bottom most oxygen ions, viewed from the top (along the $[\bar{7}\bar{1}\bar{4}]$ direction) are also shown. As seen from these figures, two adjacent rows of ions belonging to the $(\bar{2}62)$ planes and along the $[11\bar{2}]$ direction have an arrangement similar to that of the row of ions along the $[0\bar{1}11]$ direction of Al_2O_3 .

In addition to the similar arrangement of oxygen ions, the ridges (at an atomic scale) on both the surfaces probably helps in the bonding and stabilization of this epitaxial relationship. The above description was based on the arrangement of the anions. This is a good first approximation. A more detailed description should include the arrangement of the cations.

EFFECT OF GRAIN BOUNDARIES AND GRAIN ORIENTATION

Grain boundaries can have a considerable effect on the kinetics of solid state reactions. For example, in the diffusion-controlled regime, grain boundary diffusion can enhance the mobility of the various structure elements, thus increasing the growth rate. At the same time, in the interface-controlled regime, there is a tendency for easier accommodation at the junction between the two grains, which in turn increases the reaction rate at the grain boundaries. Hence, when studying the growth rates of films which are made up of multiple grains, the effect of the grain boundaries has to be evaluated.

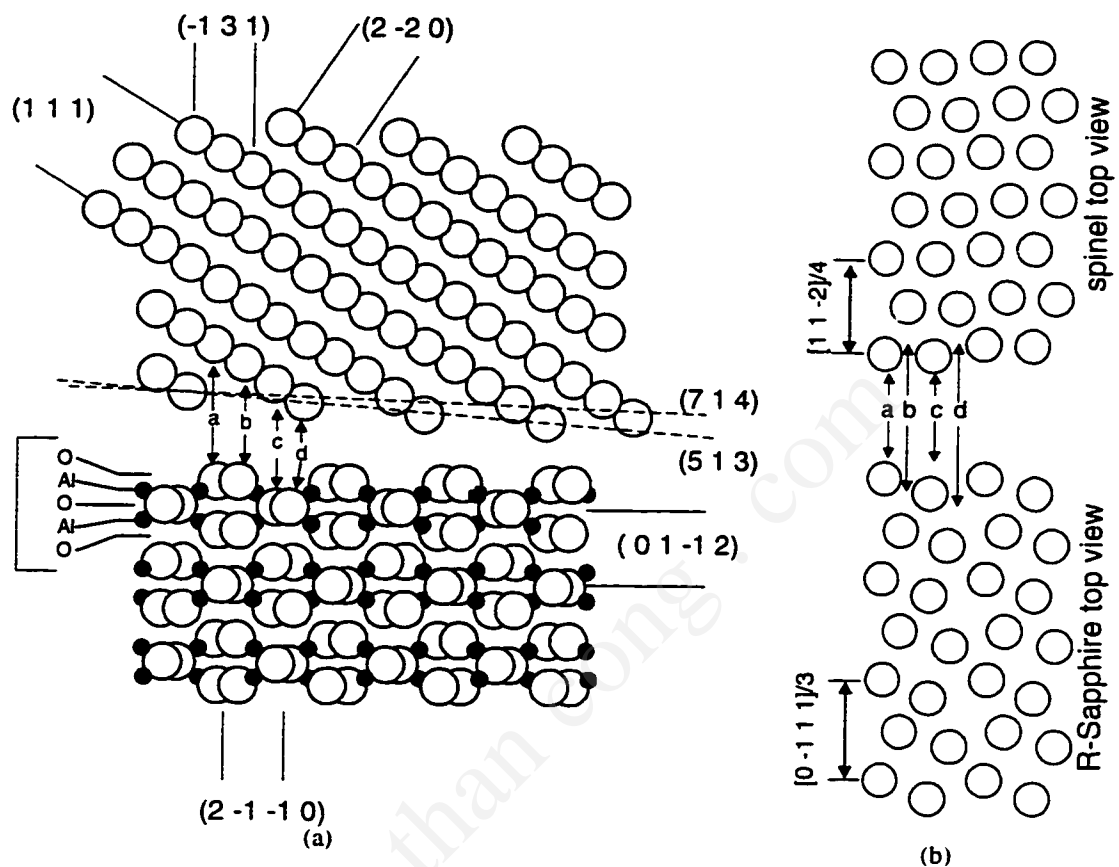


Figure 6-4. Schematic diagrams of the spinel and sapphire crystals which have the epitaxial relationship 'A' given in Table 6-1

(a). The side view along the $[0\bar{1}11]$ direction of sapphire

(b). The arrangement of the bottom layer of spinel and the top layer of the sapphire crystal

In Figure 6-5(a), the region around a grain boundary between two spinel grains is shown. This image was obtained from the sample annealed at 1000°C for 30 minutes and enhanced growth is observed near the grain boundary. The orientation of grain I corresponds to relationship 'D' in Table 6-1, while that of grain II corresponds to relationship 'E'. A region (from the sample annealed for 90 min) where there are many grains next to each other is shown in Figure 6-5 (b). As seen here, the area of the film with many grains (of smaller width) next to each other is thicker than the area far away from a grain boundary. We will see later that the growth rate also depends on the orientation of the spinel layer. The faster growth rate seen in Figure 6-5 (b) is probably a combination of the effect of grain boundaries and grain orientation. Hence, when studying the kinetics of the solid state reaction between ZnO and Al₂O₃, we have to measure the thickness far away from grain boundaries. The higher growth at the grain boundaries can be due to either enhanced diffusion at the grain boundaries or due to easier accommodation of the reacting species at the interface close to grain boundaries. We can identify the process if we establish the growth limiting step i.e. if we can determine whether the reaction is diffusion controlled or interface controlled. The growth rate for orientation A is evaluated in the next section. In this section the structure of the grain boundary region is studied in more detail.

Regions Ia and IIa in Figure 6-5(a) are tilted with respect to regions I and II respectively. Other grain boundaries with grains of other orientations were also observed to have a similar structure. The regions Ia and IIa are tilted such that the bottom of the grain moves towards the grain boundary i.e. Ia is tilted by 6.5–7° in the counter

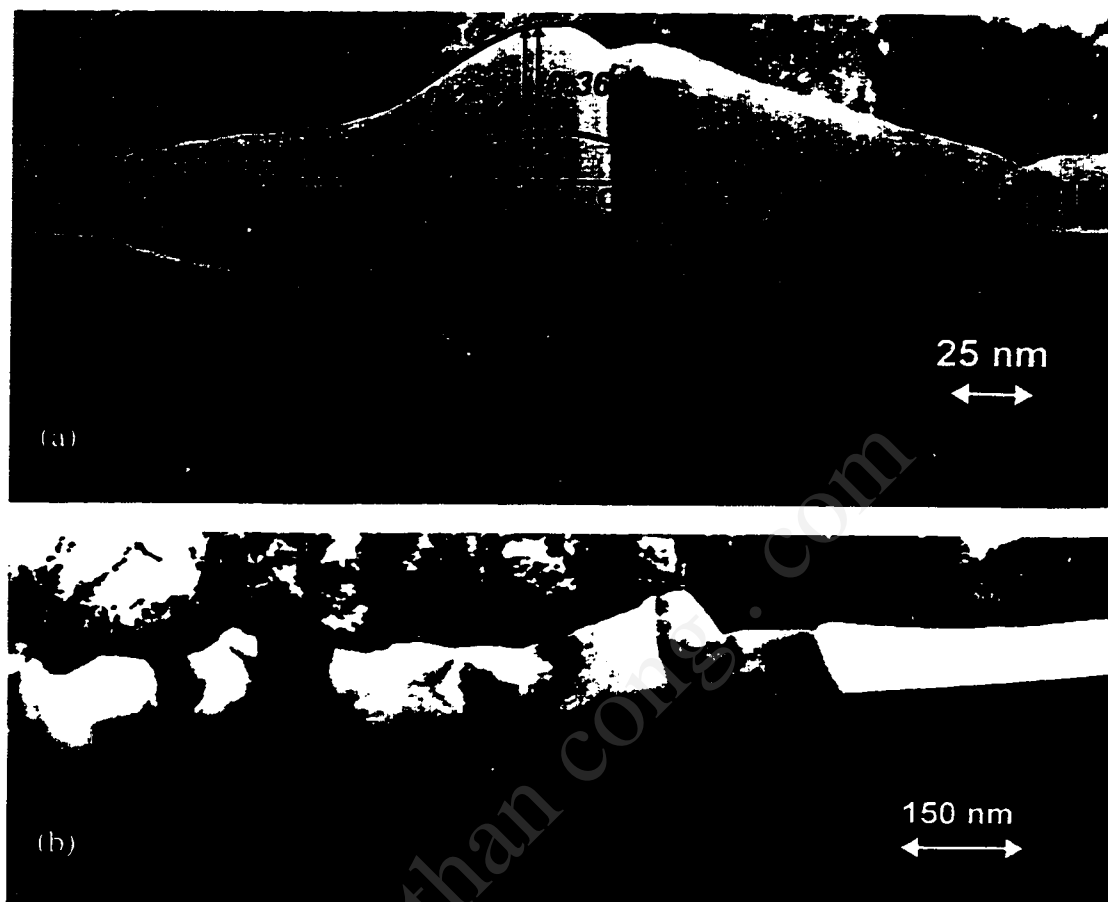
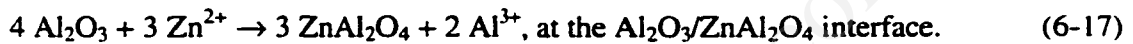


Figure 6-5. (a). Region near a grain boundary between two spinel grains. The orientation of grain I corresponds to the diffraction pattern 4(a), and that of grain II corresponds to the diffraction pattern 4(b). The overlaid schematic shows the expected position of the initial $\text{ZnO}/\text{Al}_2\text{O}_3$ interface O–O, and its position A–A after reaction. See text for explanation. Grain Ia is rotated (by 6°) counterclockwise with respect to I while IIa is rotated clockwise (by 10°) with respect to II.

(b). Another area which shows the effect of multiple grain boundaries close to each other. There is an effective thickening of the layer i.e. the growth rate appears to be larger.

clockwise direction with respect to I and IIa is tilted by 10° in the clockwise direction with respect to II.

Assuming that the mechanism involved in the formation of ZnAl_2O_4 is the counter diffusion of cations, according to which transport of oxygen ions is not involved, except for the jump across the interface, the reactions at the two interfaces (Figure 6-6) can be written as¹²⁸



The Zn^{2+} ions created at the $\text{ZnO/ZnAl}_2\text{O}_4$ interface diffuse across the spinel layer and react at the $\text{Al}_2\text{O}_3/\text{ZnAl}_2\text{O}_4$ while the Al^{3+} ions are transported in the opposite direction, thus conserving the charge. In this case, the volume ratio of the ZnO consumed to the Al_2O_3 consumed is in the ratio 0.36 : 0.64 (i.e. 93.66 : 169.33) (see Table 6-2). As shown in the schematic superimposed on the TEM image in Figure 6-5(a), the original $\text{ZnO/Al}_2\text{O}_3$ is expected to lie along the line O—O. However, the ratio of the volume of spinel formed on the ZnO side of the original interface to the volume formed on the Al_2O_3 side of the original interface is 1:3. There is a net loss in volume (27.6 cubic angstrom) when four ZnO formula units react to form one formula unit of ZnAl_2O_4 according to reaction 1 and table 6-2, due to the closer packing of the oxygen atoms in ZnAl_2O_4 . Similarly, there is a gain in volume (28.84 cubic angstrom) when four units of Al_2O_3 reacts to form three units of ZnAl_2O_4 due to the closer packing in Al_2O_3 . This reduction in volume at the ZnO/ interface and gain of volume at the $\text{Al}_2\text{O}_3/\text{ZnAl}_2\text{O}_4$ results in the shift of the planes upward. The greater the thickness of the spinel layer, the greater the shift.

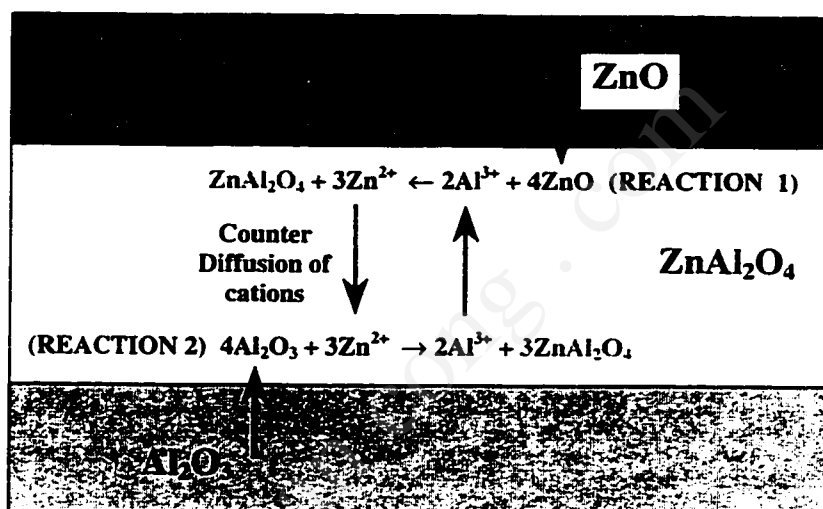


Figure 6-6 Schematic representation of the mechanism involved during the solid state reaction between ZnO and Al₂O₃. Assuming that the anions are immobile, there will be a counter flux of Zn²⁺ and Al³⁺ ions.

If the thickness were uniform, the line A–A (which represents the position of the original ZnO/Al₂O₃ interface after reaction) would be parallel to O–O; however, due to the non-uniform growth near the grain boundaries, the line A–A is curved. In the region close to the grain boundary, the shift in the original interface is more pronounced than in the region far away from the grain boundary. This is equivalent to straining or bending the crystal planes into the shape A–A, causing stresses which result in the observed tilts. In addition to the effect of enhanced growth at grain boundaries, the growth rate is observed to be dependent on the orientation of the grains.

Two adjacent grains with different orientations are shown in Figure 6-7. Grain I has an orientation 'C' (Table 6-1) while grain II is a twin (a 180° rotation about the surface normal) of orientation B. The thickness of grain I is almost twice that of grain II. Hence in addition to taking measurements far away from grain boundaries, measurements from the grains with the same orientation have to be taken into consideration when studying the solid state reaction kinetics of the ZnO/R–Al₂O₃ system.

Table 6-2: Volume changes occurring during the formation of ZnAl₂O₄ at the ZnO/Al₂O₃ interface

	Lattice parameters (Å)	Volume/unit cell (Å ³)	n*	d** (Å)	V _{reactant} used (Å ³)	V _{spinel} created	ΔV (Å ³)
ZnO	a=3.2498 c=5.20661	46.82	2	3.2498	-93.66 (reaction 1)	+66.06	-27.6
Al ₂ O ₃	a=4.758 c=12.991	254.696	6	2.747	-169.33 (reaction 2)	+198.17	+28.84
ZnAl ₂ O ₄	a=8.0848	528.4548	8	2.858			

* n: number of formula units/unit cell
** d: oxygen–oxygen nearest neighbor distance



Figure 6-7 TEM image of two adjacent grains with different growth rates. Grain I has orientation 'C' and grain II is a twin of orientation 'B' given in Table 6-1.

GROWTH KINETICS

In this section the kinetics of the reaction between ZnO and R-Al₂O₃ resulting in a spinel layer with the orientation shown in (b)–(c) is studied (orientation A in Table 6-1). The ZnO/R-Al₂O₃ film was annealed at 1000°C for 30, 90 and 150 min. Cross-section TEM samples were made from the annealed samples and the thickness of the spinel grains with orientation A was measured. Statistical sampling of measurements made by TEM is not practical because of the limited area that is imaged and the time consuming process of making cross-section samples. But in this case TEM measurements were necessary because of the necessity to identify grain boundaries and the crystalline orientation of the grains. The grains from which the thickness measurements were taken, were 1 to 10 microns wide. Care was taken to take measurements away from any grain boundaries. The effect of nucleation has to be taken into consideration when measuring the growth rate. We have observed that a 850°C anneal for 30 minutes results in a continuous spinel layer of thickness between 15 and 20 nm, wherein the nucleated grains grow laterally and join together at an early stage. At a temperature of 1000°C, the nucleation rate and the lateral growth of the grains is expected to be faster, and hence we assume that the incubation time is very short. The average thickness of the spinel grains (orientation A) in the samples annealed for 30, 90 and 150 minutes were 35 nm, 95 nm and 150 nm respectively. Variations in the thickness of the grains were observed, for example the thickness varied between 135 nm and 170 nm for the samples annealed for 150 min. The growth rate for this orientation is seen to follow a linear relationship, which suggests an interface controlled reaction.

The orientation relationship of grains A was discussed in the earlier sections. The lattice misfits at the interfaces (perpendicular to the c-axis of ZnO) are:

(a) ZnO/Al₂O₃ ($(d_{\text{sapphire}} - d_{\text{ZnO}})/d_{\text{ZnO}} = -15.38\%$ or $(d_{\text{ZnO}} - d_{\text{sapphire}})/d_{\text{sapphire}} = 18.3\%$)

(b) ZnAl₂O₄/ZnO interface, ($(d_{\text{spinel}} - d_{\text{ZnO}})/d_{\text{ZnO}} = -13.3\%$) and the

(c) ZnAl₂O₄/Al₂O₃, ($(d_{\text{spinel}} - d_{\text{sapphire}})/d_{\text{sapphire}} = 2.45\%$).

The original ZnO/Al₂O₃ interface was discussed in Chapter 4. It is atomically sharp and planar. While misfit dislocations are present at an average repeat distance corresponding to 5 (1 $\bar{1}$ 00) ZnO planes, there are highly strained regions, the origin of which we do not understand at the moment, which are present with almost twice the average separation of the misfit dislocations.

The ZnAl₂O₄/ZnO interface on the other hand, is very rough. Two images from adjoining grains (from the sample annealed for 150 min) with the same orientation are shown in Figure 6-8(a) and (b). In both figures, the average repeat distance of the misfit dislocations corresponds to 6 (1 $\bar{1}$ 00) ZnO planes. In Figure 6-8(b), the misfit dislocations (marked as '*'s) actually lie about 1 nm below the ZnO/ZnAl₂O₄ interface (marked by a '—' line). While in the region above the dislocations, the spinel forms a coherent interface with ZnO. There is some additional contrast parallel to the (111) planes. It is possible that the reaction proceeds ahead of the dislocations, but the reaction zone is limited due to increasing strain energy. In Figure 6-8(b), a slightly out of focus image of the ZnO/ZnAl₂O₄ interface from an adjoining grain is shown. The misfit dislocations in this case lie at the interface, and a coherent region as in Figure 6-8(b) is not seen.

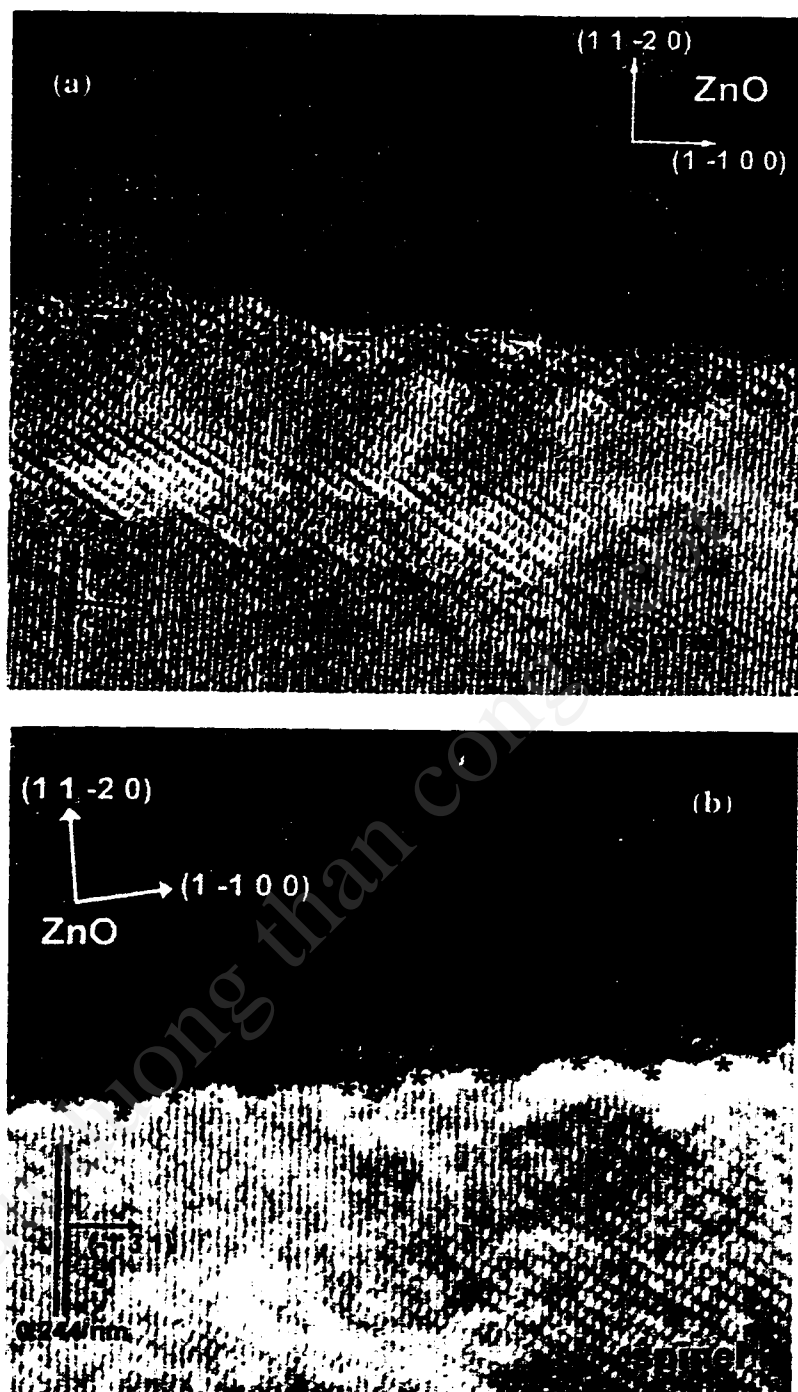


Figure 6-8: Two types of $\text{ZnO}/\text{Al}_2\text{ZnO}_4$ interfaces observed. The position of the extra planes (misfit dislocations) in the spinel are marked with a '*'. In (a) there is a thin (1 nm) spinel layer which is coherent with ZnO. The interface in (b) appears to be locally pinned.

At the same time, the interface is bowed locally as if it is being pinned. While the pinning positions do not necessarily coincide with the misfit dislocations, there is a likelihood that the strained regions observed at the $\text{ZnO}/\text{Al}_2\text{O}_3$ interface act as the pinning sources. In both type of interfaces mentioned above, the large misfit (dislocations) appears to influence the progress of the reaction front. It should be mentioned that Figure 6-8 (b) is from a very thin region and close to the edge of the sample where portions of the ZnO has been ion-milled away. Even though ion milling was carried out using a liquid nitrogen stage, we cannot categorically disregard the influence of any damage occurring during sample preparation.

A few misfit dislocations were also observed at the $\text{ZnAl}_2\text{O}_4/\text{Al}_2\text{O}_3$ interface (from the sample annealed for 150 min), but the average repeat distance could not be estimated as there were far fewer dislocations at this interface. Faceting was observed at the $\text{ZnAl}_2\text{O}_4/\text{Al}_2\text{O}_3$ interface (Figure 6-9) for this particular orientation. As seen in the figure, the facets of larger length were almost perpendicular (tilted by 2° – 3°) to the $(\bar{1}31)$ planes of ZnAl_2O_4 (the (714) plane is perpendicular to the $(\bar{1}31)$ plane and the (513) plane makes an angle of 92.9° to the $(\bar{1}31)$ plane). On the sapphire side of the interface, single steps (corresponding to the d-spacing of the $(01\bar{1}2)$ plane) were observed. It should be noted that single steps in this case actually are made up of an O–Al–O–Al–O arrangement of planes as shown in Figure 6-4.

While the climbing or gliding of the interfacial dislocations controls the reaction at the $\text{ZnO}/\text{ZnAl}_2\text{O}_4$ interface, growth at the $\text{ZnAl}_2\text{O}_4/\text{Al}_2\text{O}_3$ interface is controlled by the reaction at the steps on the sapphire surface. At present, we cannot determine which of these two interfaces is rate determining.

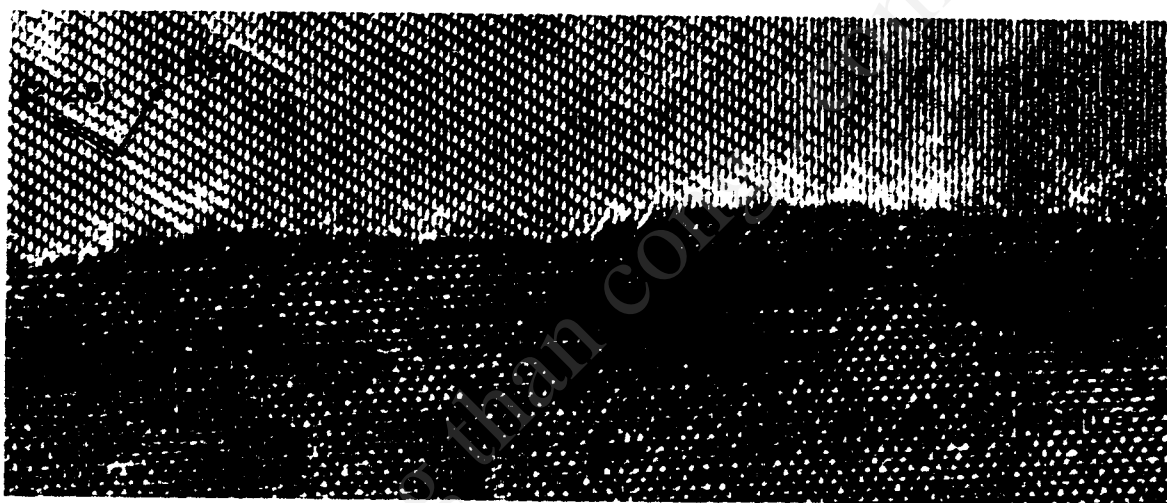


Figure 6-9: High resolution TEM image of the $\text{Al}_2\text{ZnO}_4/\text{Al}_2\text{O}_3$ interface. The spinel layer has the orientation 'A' given in Table 6-1.

6.2.2 THERMAL STABILITY

In our study, we observed the reaction rate at 1000 °C to be linear. Moreover, the rate constants in other systems have been found to follow the Arrhenius law¹³⁰

$$k = A \exp\left(-\frac{E_a}{k_B T}\right) \quad (3)$$

where E_a is the activation energy, and k_B is the Boltzmann's constant. We can extrapolate the data available from samples A and B and calculate the thickness of the spinel layer to be 3.0 to 7.5 nm for annealing between 650 °C to 750 °C for 30 min. Furthermore, nucleation is also expected to be retarded at lower temperatures. The maximum temperature of any process (growth, annealing, etc.,) has to be limited to around 750 °C to prevent the formation of a spinel layer at the interface between ZnO and R-Al₂O₃. For other applications where a thin spinel layer can be tolerated as long as it is confined to the ZnO/R-Al₂O₃ interface, higher temperatures can be used. For example, a ZnO buffer layer of appropriate thickness can be used for applications involving the growth of III-Nitrides by MBE, so that the spinel layer, even if it forms, is confined to the ZnO/Al₂O₃ interface and does not affect the top growth surface.

Chapter 7 : CONCLUSIONS

1. MOCVD technique was successfully used to grow high quality epitaxial ZnO films on $(01\bar{1}2)$ Al_2O_3 (R-plane sapphire). The limitations presented by the vigorous gas-phase reaction between DEZn and O_2 has been circumvented by incorporating separate injectors for DEZn and O_2 in a vertical-flow rotating-disk reactor. The injectors were placed at a short distance from the substrate and were positioned in such a way that DEZn and O_2 entered different zones in the reactor, thereby reducing pre-reactions. An optimum growth temperature of 450°C was obtained. Below 300°C , the quality of the crystals was poor as the temperature is too low for sufficient surface diffusion of the adsorbed species to occur; whereas above 550°C gas phase reactions were dominant resulting in particle like deposition on the substrate.

The epitaxial relationship between ZnO and the R-plane sapphire was evaluated by a combination of x-ray θ - 2θ and ϕ -scan measurements, and cross-sectional electron diffraction. The epitaxial relationship was determined to be:

$$(11\bar{2}0)\text{ZnO} // (01\bar{1}2)\text{Al}_2\text{O}_3 \text{ and } [0001]\text{ZnO} // [0\bar{1}11]\text{Al}_2\text{O}_3.$$

The c-axis of ZnO lies in the plane of the ZnO film. This leads to important device application due to the anisotropy in physical properties perpendicular to and parallel to the c-axis.

For comparison, the epitaxial relationship between ZnO and C-sapphire was determined to be:

$$(0001)\text{ZnO} // (0001)\text{Al}_2\text{O}_3 \text{ and } [10\bar{1}0]\text{ZnO} // [2\bar{1}\bar{1}0]\text{Al}_2\text{O}_3.$$

This orientation relationship corresponds to a 30° rotation about the c-axis of the ZnO unit cell with respect to the Al_2O_3 unit cell, resulting in a continuation of the oxygen sublattices across the $\text{Al}_2\text{O}_3/\text{ZnO}$ interface.

The ZnO films on R- Al_2O_3 had a very smooth surface morphology, and grain boundaries were not observed by TEM. The predominant defects were threading dislocations. On the other hand, columnar growth and grain boundaries were observed in the ZnO films grown on C- Al_2O_3 under similar growth conditions. The as-grown $(11\bar{2}0)$ ZnO / $(01\bar{1}2)$ Al_2O_3 interface was atomically sharp and semi-coherent. The 18.3 % lattice misfit along the $[1\bar{1}00]$ direction of ZnO was relieved by a regular array of misfit dislocations with an average spacing of 1.4 nm.

2. To investigate the surface acoustic wave properties in the ZnO/R- Al_2O_3 system, prototype SAW delay lines were fabricated. The SAW propagation direction was chosen along the c-axis of ZnO. The structures were designed to have SAW wavelengths between $10\text{ }\mu\text{m}$ and $16\text{ }\mu\text{m}$ on $0.5\text{ }\mu\text{m}$ and $1.5\text{ }\mu\text{m}$ thick ZnO films. An effective electromechanical coupling coefficient (k_{eff}^2) of 6 % was obtained for the $10\text{ }\mu\text{m}$ device fabricated on the $1.5\text{ }\mu\text{m}$ thick ZnO film, which is close to the value for bulk single crystal ZnO. A low insertion loss value of 5 dB was observed for the same device. The smooth surface morphology and the absence of grain boundaries (low scattering of the SAW into other acoustic modes), in conjunction with the sharp and semicoherent ZnO/ Al_2O_3 interface provides efficient acoustic energy transfer in SAW devices, resulting in the observed low insertion loss. A maximum SAW velocity of 5800 m/sec was obtained for a $16\text{ }\mu\text{m}$ device fabricated on a $0.5\text{ }\mu\text{m}$ thick ZnO film.

The low temperature (11 K) Photoluminescence spectra showed a sharp donor bound excitonic peak at 3.363 eV with a full width at half maximum of 6 meV. In comparison with the FWHM value of 3 meV (4.2 K) from bulk ZnO and 8.9 meV (4.2 K) from ZnO grown on GaN/SiC by MBE, it clearly indicates the films high quality. The anisotropic absorption characteristics for light polarized parallel to and perpendicular to the c-axis of ZnO were also investigated. Although the shape of the transmission and reflectivity curves are similar for the two polarizations, the curves for $E//c$ are shifted by ~ 20 meV to higher energy with respect to those for $E \perp c$. This phenomenon is primarily related to the anisotropy in absorption associated with the polarization selection rules for different excitons in ZnO.

3. The thermal stability of the ZnO/R-Al₂O₃ films was investigated by annealing them in an O₂+N₂ atmosphere at temperatures above 850°C. The crystalline quality of the ZnO improved on annealing at 850°C for 30 minutes, resulting in a x-ray rocking curve FWHM of 0.25°. Simultaneously, ZnO reacted with Al₂O₃ forming a thin spinel layer (ZnAl₂O₄) at the interface. The thickness of the spinel layer formed after annealing for 30 min at 850°C and 1000°C was 15 nm and 35 nm respectively. Based on an Arrhenius type relationship for the growth, and considering that the nucleation rate decreases exponentially with decreasing temperature, the interface would be stable for annealing temperatures up to 700 - 750 °C. Beyond this temperature range, reaction at the interface is expected. The kinetics of the spinel formation at 1000°C was investigated in detail. A linear growth rate was observed for annealing up to 150 minutes, which suggests an interface-controlled reaction, and the mechanism for growth was established as due to

counter diffusion of Al^{3+} and Zn^{2+} cations in a stationary oxygen anion lattice. The structures of the $\text{ZnO}/\text{ZnAl}_2\text{O}_4$ interface and the $\text{ZnAl}_2\text{O}_4/\text{Al}_2\text{O}_3$ interface were evaluated.

Future Work

In this dissertation, we have solved some of the hurdles for using MOCVD grown ZnO films for low-loss high-frequency SAW applications. Two important research topics for future work are ZnO growth on diamond films, and p-type doping of ZnO films.

In order to further increase the operational frequency of SAW devices, ZnO has to be deposited on to diamond, as diamond has a very high acoustic velocity. Hence, high quality ZnO deposition on diamond is a very important research area for the future.

For practical SAW devices, the temperature coefficient of frequency (TCF) has to be close to zero. By combining ZnO, (which has a negative TCF) with SiO_2 (which has a positive TCF), a system with zero TCF can be obtained. Hence growth and fabrication techniques have to be optimized for ZnO on SiO_2 and quartz.

One of the main technical barriers to using ZnO films in various electronic and optoelectronic devices such as Laser Diodes and UV photodetectors, is the difficulty of obtaining p-type doped films. Limited success has been obtained by doping the ZnO films with nitrogen. The nitrogen source used for doping purposes is usually N_2 or NH_3 . At the present MOCVD growth temperature (400 to 450 °C), the breakdown of these gases, especially that of N_2 , is very difficult. The optimum way to decompose these gases is to create a N_2 or NH_3 Remote Plasma in a quartz tube connected to the MOCVD chamber, followed by the transport of the radical and ionized species to the growth surface, which are then incorporated into the growing film.

APPENDIX A

Elastic, piezoelectric, and dielectric constants of ZnO

Piezoelectricity is a linear interaction between electrical and mechanical systems. The direct piezoelectric effect is that electric polarization is produced by mechanical stress. Closely related to it is the converse effect, whereby a crystal becomes strained when an electric field is applied. Centrosymmetric classes are always inactive in piezoelectricity. Out of the 32 point groups, only crystals belonging to 20 of them can show piezoelectricity. 6mm, the point group of wurtzite, is one of them. Crystals with the diamond cubic structure (Si, diamond, Ge) do not show piezoelectricity. The constitutive equation relating the electric and mechanical variables are:

$$T_{ij} = c_{ijkl} S_{kl} - e_{nij} E_n$$

$$D_n = e_{nkl} S_{kl} + \epsilon_{ni} E_i$$

where T_{ij} is the stress tensor (Nm^{-2}),

S_{kl} is the strain tensor,

c_{ijkl} is the stiffness tensor (Nm^{-2}),

e_{nij} is the piezoelectric coefficient (Cm^{-2})

ϵ_{ni} is the permittivity or dielectric constant (Fm^{-1})

D_n is the electric displacement (Cm^{-2}), and

E_n is the electric field intensity (Vm^{-1})

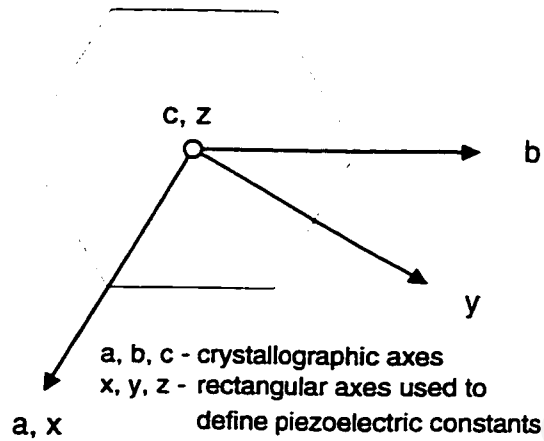


Figure A-1: Relationship between crystallographic axes and axes used in defining physical constants in 6mm crystals.

The relationship between the crystallographic axes of 6mm crystals with respect to those used for defining the piezoelectric and other constants is shown in Figure A-1.⁶² The piezoelectric tensor for a 6mm crystal has three independent constants, and is of the form:

$$\begin{pmatrix} 0 & 0 & 0 & 0 & e_{15} & 0 \\ 0 & 0 & 0 & e_{15} & 0 & 0 \\ e_{31} & e_{31} & e_{33} & 0 & 0 & 0 \end{pmatrix}$$

($e_{il} \equiv e_{ijk}$ in actual tensor notation

$1 \rightarrow 11, 2 \rightarrow 22, 3 \rightarrow 33, 4 \rightarrow 23, 5 \rightarrow 13, 6 \rightarrow 12$)

The piezoelectric stress constants for ZnO are:⁶⁰

$$e_{15} = -0.48 \text{ C/m}^2, e_{31} = -0.573 \text{ C/m}^2, \text{ and } e_{33} = 1.32 \text{ C/m}^2$$

Dielectric permittivity tensor for a 6mm crystal has two independent constants, and is of the form

$$\begin{pmatrix} \epsilon_{11} & 0 & 0 \\ 0 & \epsilon_{11} & 0 \\ 0 & 0 & \epsilon_{33} \end{pmatrix}$$

The permittivity constants (at constant strain) for ZnO are:

$$\epsilon_{11} = 8.55, \text{ and } \epsilon_{33} = 10.2$$

Stiffness tensor for a 6mm crystal has five independent constants

$$\begin{pmatrix} c_{11} & c_{12} & c_{13} & 0 & 0 & 0 \\ c_{12} & c_{11} & c_{13} & 0 & 0 & 0 \\ c_{13} & c_{13} & c_{33} & 0 & 0 & 0 \\ 0 & 0 & 0 & c_{44} & 0 & 0 \\ 0 & 0 & 0 & 0 & c_{44} & 0 \\ 0 & 0 & 0 & 0 & 0 & \frac{1}{2}(c_{11} - c_{12}) \end{pmatrix}$$

($c_{mn} \equiv c_{ijkl}$ in actual tensor notation, same rules as above apply for conversion).

The elastic stiffness constants (10^{10} N/m²) for ZnO are:

$$c_{11} = 20.97, c_{12} = 12.11, c_{13} = 10.51, c_{33} = 21.09, c_{44} = 4.247.$$

APPENDIX B

Basic Microwave Circuit Analysis and S-parameter model

Because of the high frequencies and small wavelengths, standard circuit theory cannot be used directly to solve microwave network problems. In general circuit theory, due to the insignificant phase variation (of a voltage or current signal) across the dimensions of a component (due to large λ), lumped circuit elements are considered. In contrast, microwave circuit analysis¹⁴² involves distributed circuit elements as the phase of a voltage or current signals changes significantly over the physical extent of the device because the device dimensions are on the order of the microwave wavelength. Hence in a strict sense, the theory of electromagnetics as described by the Maxwell's equations should be used for solving such problems. Simplifications can be made by using the transmission line theory, if we are only interested in the fields at the ends or terminals of these components.

For a loss-less transmission line, the voltage and current along its length (z) are given by¹⁴²

$$V(z) = V_0^+ e^{-j\beta z} + V_0^- e^{j\beta z} \quad (\text{B-1})$$

$$I(z) = \frac{V_0^+}{Z_0} e^{-j\beta z} - \frac{V_0^-}{Z_0} e^{j\beta z} \quad (\text{B-2})$$

where

$$Z_0 = \sqrt{\frac{L}{C}} \quad (\text{B-3})$$

$$\beta = \omega \sqrt{LC} \quad (\text{B-4})$$

V_0^+ is the amplitude of the travelling wave (voltage) in the +z direction,

V_0^- is the amplitude of the travelling wave in the $-z$ direction,

ω is the frequency

L is the series inductance per unit length (H/m), and

C is the shunt capacitance per unit length (F/m).

Z_0 is called the characteristic impedance of the transmission line.

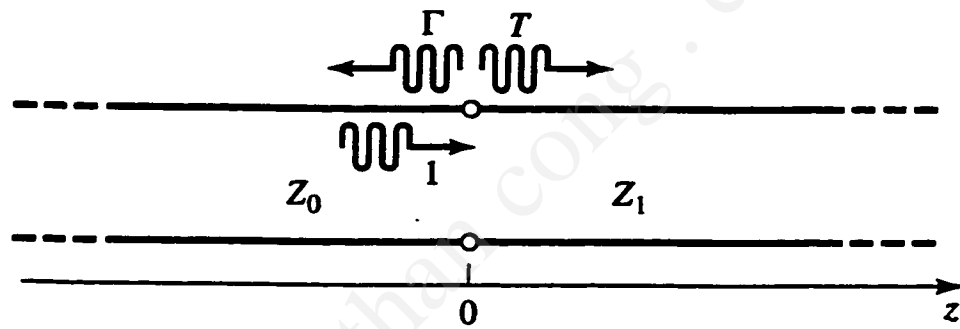


Figure B-1: Reflection and transmission at the junction of two transmission lines with different characteristic impedances. [142]

Let us consider the case of two transmission line with characteristic load impedences Z_0 and Z_1 respectively which are connected to each other. Let us assume a voltage signal

$$V(z) = V_0^+ e^{-\beta z} \quad (\text{B-5})$$

is generated from a source at $z < 0$. If a signal

$$V(z, z > 0) = V_1^+ e^{-\beta_1 z} \quad (\text{B-6})$$

is transmitted into the line on the right, in order to match the voltage and current signals at the junction, a wave of the form

$$V_0^- e^{j\beta z} \quad (\text{B-7})$$

has to be reflected back into transmission line 1 (TL1). Hence the net voltage and current relationships in TL1 Are given by equations (B-1) and (B-2). Matching the voltages and currents at the junction ($z = 0$), we obtain

$$V_0^+ + V_0^- = V_1^+ \quad (\text{B-8})$$

$$\frac{V_0^+}{Z_0} - \frac{V_0^-}{Z_0} = \frac{V_1^+}{Z_1} \quad (\text{B-9})$$

Dividing (23) by (24), we obtain

$$Z_1 = \frac{V_0^+ + V_0^-}{V_0^+ - V_0^-} Z_0 \quad (\text{B-10})$$

From this we obtain, the reflection coefficient (Γ), which is the amplitude of the reflected wave to that of the incident wave

$$\Gamma = \frac{V_0^-}{V_0^+} = \frac{Z_1 - Z_0}{Z_1 + Z_0} \quad (\text{B-11})$$

Equating the voltages at the junction, we obtain

$$V_1^+ = (1 + \Gamma) V_0^+ = T V_0^+ \quad (\text{B-12})$$

where T is the transmission coefficient. Thus at any junction which joins two components with different impedences, a reflected wave is generated, and hence only part of the power is transmitted across. When $Z_1 = Z_0$ i.e. when the load is matched, there is no reflected wave, and all the power is transmitted across the junction. Similar results can be obtained for a load (R_L) terminating the transmission line.

S-Parameter model

The behavior of a SAW device or a microwave network to an input signal is evaluated by measuring certain parameters measured at the network terminals (ports) without regard to the contents of the network. Once the parameters of the network are determined, its behavior in any external environment can be predicted, again without regard to the contents of the network. The behavior of SAW devices are evaluated by modeling them as two port networks: an input port and an output port. Many sets of parameters can be evaluated, but the most common and useful set of parameters for microwave design and analysis are the scattering parameters, also known as the S-parameters.¹⁴³ Each parameter set is related to a set of four variables associated with the two-port model. Two of these represent the excitation of the network (independent variables) and the remaining two represent the response of the network to the excitation (dependent variables).

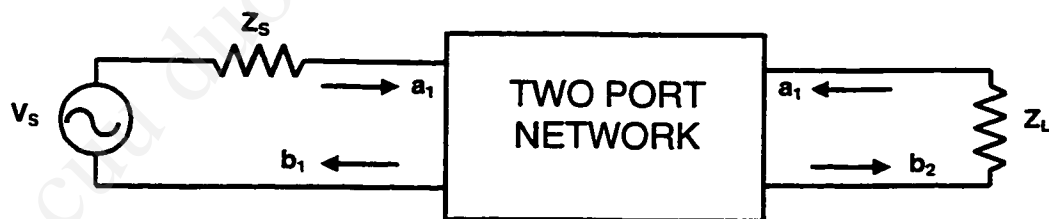


Figure B-2: Two-port network model used to characterize microwave devices and circuits.

In the S-parameter model, the independent or excitation variables are the incident waves (a_1 and a_2) and the dependent variables. The variables a_1 , a_2 , b_1 and b_2 are specified as

$$a_1 = \frac{V_1^+}{\sqrt{Z_0}} = \frac{\text{voltage wave incident on port 1}}{\sqrt{Z_0}} \quad (\text{B-13})$$

$$a_2 = \frac{V_2^+}{\sqrt{Z_0}} = \frac{\text{voltage wave incident on port 2}}{\sqrt{Z_0}} \quad (\text{B-14})$$

$$b_1 = \frac{V_1^-}{\sqrt{Z_0}} = \frac{\text{voltage wave reflected from port 1}}{\sqrt{Z_0}} \quad (\text{B-15})$$

$$b_2 = \frac{V_2^-}{\sqrt{Z_0}} = \frac{\text{voltage wave reflected from port 2}}{\sqrt{Z_0}} \quad (\text{B-16})$$

where Z_0 is an arbitrary reference impedance. The linear equations describing the two-port network are then:

$$b_1 = s_{11} a_1 + s_{12} a_2 \quad (\text{B-17})$$

$$b_2 = s_{21} a_1 + s_{22} a_2 \quad (\text{B-18})$$

which can be written in the matrix form as

$$\begin{pmatrix} V_1^- \\ V_2^- \end{pmatrix} = \begin{pmatrix} s_{11} & s_{12} \\ s_{21} & s_{22} \end{pmatrix} \begin{pmatrix} V_1^+ \\ V_2^+ \end{pmatrix} \quad (\text{B-19})$$

The s-parameters represent

$$s_{11} = \left. \frac{b_1}{a_1} \right|_{a_2=0} = \text{Input reflection coefficient with the output port terminated by a matched load } (Z_L = Z_0 \text{ sets } a_2 = 0)$$

$$s_{12} = \left. \frac{b_1}{a_2} \right|_{a_1=0} = \text{Reverse transmission gain with the input port terminated by a matched load } (Z_S = Z_0 \text{ sets } a_1 = 0)$$

$$s_{21} = \left. \frac{b_2}{a_1} \right|_{a_2=0} = \text{Forward transmission gain with the output port terminated by a matched load}$$

$$s_{22} = \left. \frac{b_2}{a_2} \right|_{a_1=0} = \text{Output reflection coefficient with the input port terminated by a matched load}$$

The physical significance of these parameters are

$$|s_{11}|^2 = \frac{\text{Power reflected from the network input}}{\text{Power incident on the network input}}$$

$$|s_{22}|^2 = \frac{\text{Power reflected from the network output}}{\text{Power incident on the network output}}$$

$$|s_{21}|^2 = \frac{\text{Power delivered to a } Z_0 \text{ load}}{\text{Power available from } Z_0 \text{ source}} = \text{Transducer power gain with } Z_0 \text{ load and source}$$

$$|s_{21}|^2 = \text{Re verse transducer power gain with } Z_0 \text{ load and source}$$

In SAW filters, we will be most interested in the s_{21} parameter, which represents the response of the filter to an input signal. Testing and measurement of the s-parameters is accomplished using a Network Analyzer.

APPENDIX C

X-RAY ϕ -SCAN MEASUREMENTS

While X-ray diffraction θ - 2θ measurements are sufficient to determine the orientation perpendicular to the surface of thin films, ϕ -scans are required to determine the in-plane orientation of single crystals or epitaxial thin films. The basic geometries for measuring θ - 2θ and ϕ scans are shown in Figure C-1. X-rays are scattered most efficiently by crystalline planes with interplanar spacing d_0 when the angle of incidence (θ_{B0} is the Bragg angle) of the x-rays (of wavelength λ) is given by the Braggs law:

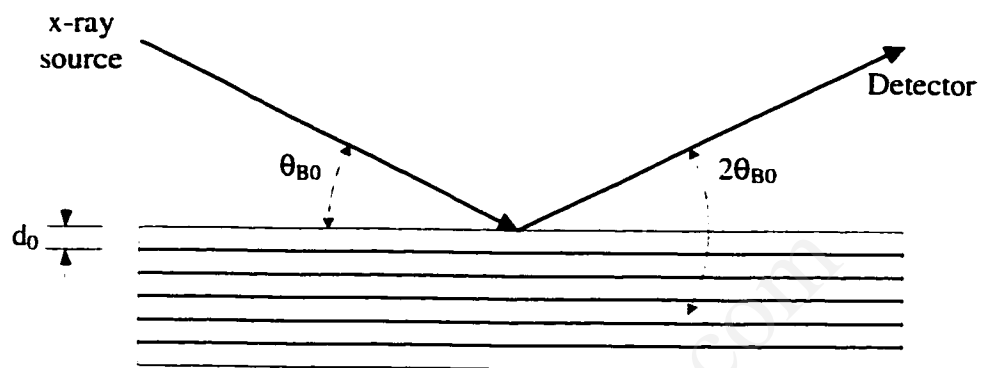
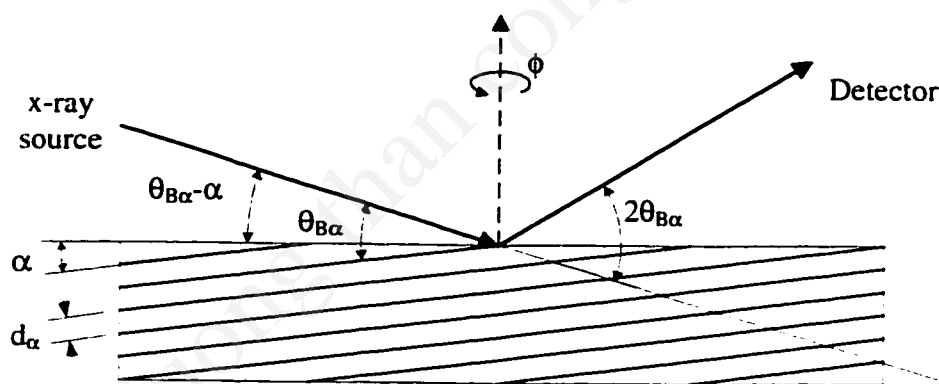
$$\lambda = 2d_0 \sin \theta_{B0} \quad (C-1)$$

In a θ - 2θ scan, the intensity of the scattered beam is collected for varying incident angles. The incidence angle is varied by changing the position of the sample (by $\Delta\theta$), while the position of the detector is simultaneously changed by twice the angle ($2\Delta\theta$). The d-spacing of the reflecting plane is calculated by measuring the bragg angle i.e. the angle at which the diffracted intensity is a maximum. For the crystal structure and the d-spacing value, the plane which is oriented parallel to the surface can be identified.

The condition that has to be satisfied by a plane in order to obtain a ϕ -scan is

$$\alpha < \theta_{B\alpha}, \quad (C-2)$$

where α is the angle between the plane under consideration and the plane parallel to the surface, and $\theta_{B\alpha}$ is the bragg angle of the plane under consideration.

(a) θ - 2θ scan(b) ϕ - scanFigure C-1: The basic geometry for measuring x-ray (a) θ - 2θ and (b) ϕ -scans

In a ϕ -scan, the number of planes of a certain $\{h\ k\ \bullet\ l\}$ family which make the same angle with the plane parallel to the surface of the film is determined. The incident angle is kept constant at $(\theta_{B\alpha}-\alpha)$, while the detector position is kept constant at $2\theta_{B\alpha}$. The sample is rotated (ϕ) about the surface normal, which brings the various planes (of the same family which make the same angle α) into bragg condition sequentially. The diffracted intensity is plotted against the angle of rotation, ϕ , and the number of peaks in this plot and the angular separation between the different peaks will give the required crystallographic information. The separation between the peaks in a ϕ -scan corresponds to the angular separation between the corresponding projections of the normals to the planes onto the plane parallel to the surface of the film.

For calculating angles between planes or directions in hexagonal crystals, it is convenient the ortho-hexagonal unit cell shown in Figure C-2(a). The unit vectors in the ortho-hexagonal lattice in terms of the unit vectors in the hexagonal lattice are

$$\begin{aligned} \mathbf{a}_1' &= \mathbf{a}_1 \\ \mathbf{a}_2' &= \mathbf{a}_1 + 2\mathbf{a}_2 \\ \mathbf{c}' &= \mathbf{c} \end{aligned} \tag{C-3}$$

To convert the indices of a plane, $(h\ k\ l)$, from the hexagonal to the ortho-hexagonal system, the following conversion is used.

$$\begin{pmatrix} h \\ k \\ l \end{pmatrix} = \begin{pmatrix} 1 & 0 & 0 \\ 1 & 2 & 0 \\ 0 & 0 & 1 \end{pmatrix} \begin{pmatrix} h' \\ k' \\ l' \end{pmatrix} \tag{C-4}$$

Hence the indices of the plane in the ortho-hexagonal system are

$$(h', k', l') = (h, h+2k, l)$$

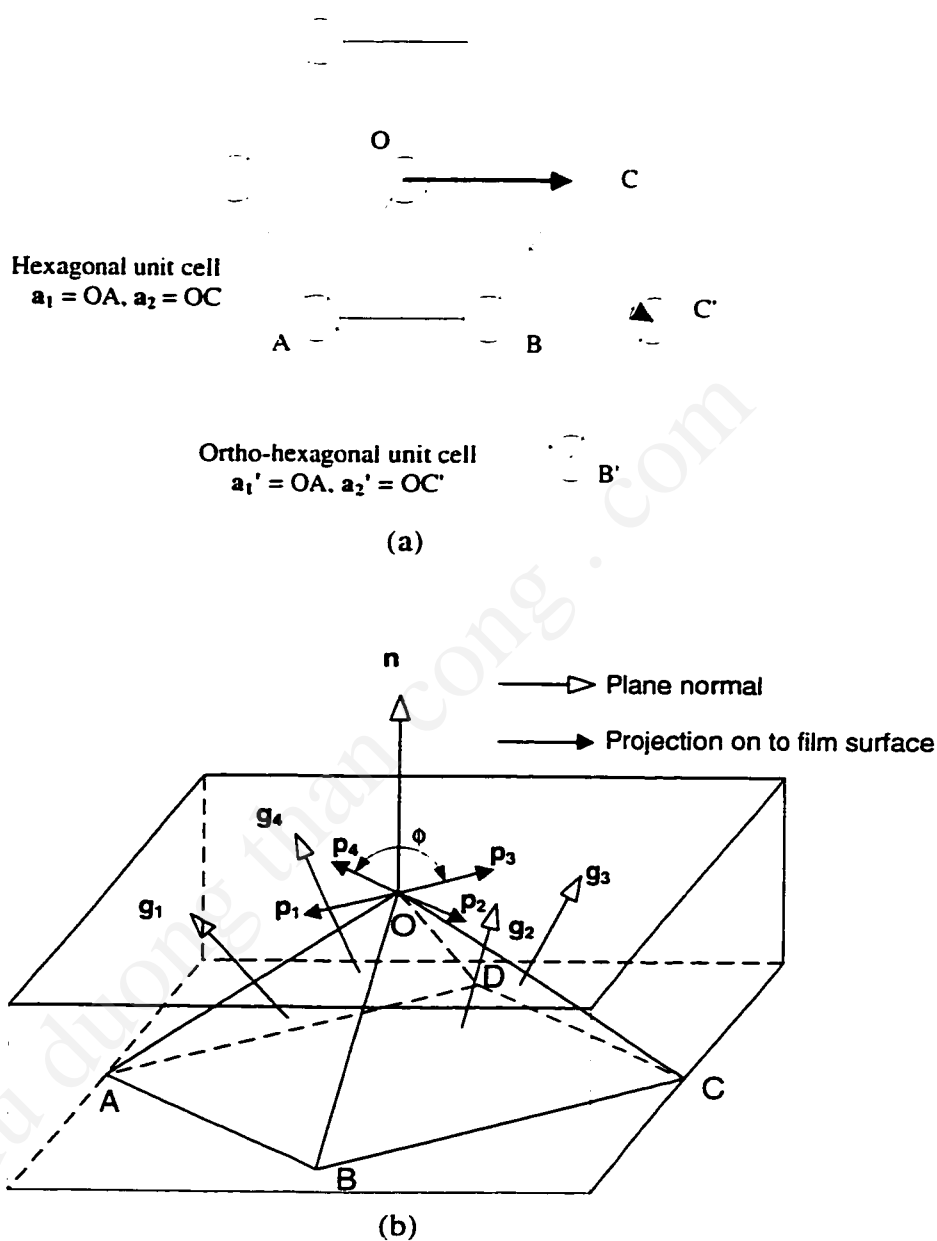


Figure C-2: (a). Unit vectors in the basal plane used to define the hexagonal and ortho-hexagonal unit cells.

(b). Schematic diagram used to explain the $\{21\bar{1}\}$ ϕ -scan of ZnO.

The unit vectors in the ortho-hexagonal system are

$$\mathbf{a}_1' = a \hat{i}, \quad \mathbf{a}_2' = \sqrt{3} a \hat{j}, \quad \mathbf{c}' = c \hat{k}$$

where \hat{i} and \hat{j} are the orthogonal unit vectors along OA and OC' respectively, \hat{k} is the unit vector perpendicular to the basal plane (along the c-axis), and 'a' and 'c' are the lattice parameter of the hexagonal unit cell.

The reciprocal lattice vectors are

$$\begin{aligned} \mathbf{r}_1' &= \frac{\mathbf{a}_2' \times \mathbf{c}'}{\mathbf{a}_1' \bullet (\mathbf{a}_2' \times \mathbf{c}')} = \frac{1}{a} \hat{i} \\ \mathbf{r}_2' &= \frac{\mathbf{a}_1' \times \mathbf{c}'}{\mathbf{a}_2' \bullet (\mathbf{a}_1' \times \mathbf{c}')} = \frac{1}{\sqrt{3} a} \hat{j}, \text{ and} \\ \mathbf{r}_3' &= \frac{\mathbf{a}_1' \times \mathbf{a}_2'}{\mathbf{c}' \bullet (\mathbf{a}_1' \times \mathbf{a}_2')} = \frac{1}{c} \hat{k}. \end{aligned} \quad \text{C-5}$$

Where ' \bullet ' represents vector dot product, and ' \times ' represents vector cross product.

Hence the normal to an ($h k l$) plane (indices referred to the hexagonal cell) is given by

$$\mathbf{g} = h \mathbf{r}_1 + k \mathbf{r}_2 + l \mathbf{r}_3 = h' \mathbf{r}_1' + k' \mathbf{r}_2' + l' \mathbf{r}_3' = \frac{h}{a} \hat{i} + \frac{(h+2k)}{\sqrt{3} a} \hat{j} + \frac{l}{c} \hat{k} \quad \text{C-6}$$

where \mathbf{r}_1 , \mathbf{r}_2 , and \mathbf{r}_3 are the reciprocal lattice vectors in the hexagonal system. Hence the angle (α) between two planes ($h_1 k_1 l_1$) and ($h_2 k_2 l_2$) is given by

$$\cos(\alpha) = \frac{h_1 h_2 + k_1 k_2 + \frac{1}{2}(h_1 k_2 + h_2 k_1) + \frac{3}{4} \frac{a^2}{c^2} l_1 l_2}{\sqrt{\left(h_1^2 + k_1^2 + h_1 k_1 + \frac{3}{4} \frac{a^2}{c^2} l_1^2 \right) \left(h_2^2 + k_2^2 + h_2 k_2 + \frac{3}{4} \frac{a^2}{c^2} l_2^2 \right)}} \quad \text{C-7}$$

The ϕ -scan from the $\{21\bar{3}1\}$ family of planes of a $(11\bar{2}0)$ oriented ZnO crystal is explained using Figure C-2(b). The data was presented in Section 4.1. The bragg angle

for this family of planes is 47.7° . There are 12 planes which belong to this family, out of which we have to find the ones which satisfy condition C-2. The 12 planes and the angles they make with the $(11\bar{2}0)$ plane are given below.

$$\begin{array}{llll}
 (12\bar{3}1) : 15.82^\circ & (12\bar{3}\bar{1}) : 15.82^\circ & (21\bar{3}\bar{1}) : 15.82^\circ & (21\bar{3}1) : 15.82^\circ \\
 (3\bar{1}\bar{2}1) : 50.11^\circ & (3\bar{1}\bar{2}\bar{1}) : 50.11^\circ & (\bar{1}3\bar{2}\bar{1}) : 50.11^\circ & (\bar{1}3\bar{2}1) : 50.11^\circ \\
 (3\bar{2}\bar{1}1) : 71.31^\circ & (3\bar{2}\bar{1}\bar{1}) : 71.31^\circ & (\bar{2}3\bar{1}\bar{1}) : 71.31^\circ & (\bar{2}3\bar{1}1) : 71.31^\circ
 \end{array}$$

Only the first four planes which make a 15.82° angle with the $(11\bar{2}0)$ plane satisfy condition C-2, and hence a $\{21\bar{3}1\}$ ϕ -scan (from a single crystal or epitaxial $(11\bar{2}0)$ oriented ZnO) with an incident angle ($47.7^\circ - 14.82^\circ = 32.88^\circ$) should contain four peaks of equal intensity. Let us represent the normals to these planes (the reciprocal lattice vectors) by \mathbf{g}_1 , \mathbf{g}_2 , \mathbf{g}_3 , and \mathbf{g}_4 respectively (see Figure C-2(b)). As mentioned earlier, separation of the peaks in the ϕ -scan correspond to the angular separation between the projections of the normals to these planes onto the plane parallel to the surface of the film or crystal. Let the corresponding projections of these four planes be represented by \mathbf{p}_1 , \mathbf{p}_2 , \mathbf{p}_3 and \mathbf{p}_4 respectively. If \mathbf{n} is the unit vector normal to the plane parallel to the surface, then the component of a vector \mathbf{g} perpendicular to \mathbf{n} (i.e. component in the plane of the surface) is given by

$$\mathbf{p} = \mathbf{g} - (\mathbf{g} \cdot \mathbf{n})\mathbf{n} \quad \text{C-8}$$

Using equation C-6 and C-8, the projections \mathbf{p}_1 , \mathbf{p}_2 , \mathbf{p}_3 and \mathbf{p}_4 can be calculated. From these, the angle between the projections can be calculated. The angle calculated between the $(12\bar{3}1)$ peak and the $(12\bar{3}\bar{1})$ peak is 94.5° , and that between the $(12\bar{3}\bar{1})$ peak and the $(21\bar{3}\bar{1})$ peak is 85.5° , which are the values observed in the experimental ϕ -

scans obtained from MOCVD grown ZnO films on R-sapphire (Figure 4-2). Hence the films are epitaxial, and as there are only four peaks, no other orientations are present.

cuu duong than cong . com

REFERENCES

- ¹ S. Fujishima, H. Ishiyama, A. Inoue, and H. Ieki, in The Proceedings of the 1976 IEEE International Frequency Control Symposium, p. 119, (1976).
- ² T. W. Grudkowski, J. F. Black, G. W. Drake, and D. E. Cullen, 1982 IEEE Int. Frequency Control Symp. (IEEE, NJ, 1982), p. 537.
- ³ R. Scheer, M. Wilhelm, and L. Stolt, Appl. Phys. Lett., **70**, 1011 (1997).
- ⁴ B-S. Jeon, J. S. Yoo and J. D. Lee, J. Electrochem. Soc., **143**, 3923 (1996).
- ⁵ F. Hamdani, A. Botchkarev, W. Kim, H. Moorkoc, M. Yeadon, J. M. Gibson, S-C. Y. Tsen, D. J. Smith, D. C. Reynolds, D. C. Look, K. Evans, C. W. Mitchel and P. Hemenger, Appl. Phys. Lett., **70**, 467 (1997)
- ⁶ J. P. Suchet, *Chemical Physics of Semiconductors* (Van Nostrand, London, 1965).
- ⁷ W. Ranke, Sol. State Commun. **19**, 685 (1976).
- ⁸ *International Tables for X-ray crystallography*, Volume 1, The International Union of Crystallography, Kynoch Press, England, 1965.
- ⁹ In *Pearson's Handbook of Crystallographic Data for Intermetallic Phases*, Vol. 2., by P. Villars, and L. D. Calvert, American Society for Metals, Ohio, 1985.
- ¹⁰ J.G. Fripiat, A.A. Lucas, J.M. Andre and E.G. Derouane, Chemical Physics, **21**, 101 (1977).
- ¹¹ P.W. Tasker, J. Phys. C: Solid State Phys., **12**, 4977 (1979).
- ¹² O. Ambacher, J. Phys. D, **31**, 2653 (1998).
- ¹³ S. Nakamura, and G. Fasol, *The Blue Laser Diode* (Springer, Heidelberg, 1997).
- ¹⁴ S. Nakamura, M. Senoh, S. Nagahama, N. Iwasa, T. Yamada, T. Matsushita, H. Kiyoku, Y. Sugimoto, T. Kozaki, H. Umemoto, M. Sano, and K. Chocho, Jap. J. Appl. Phys. part 2, **37**, L627 (1998).
- ¹⁵ M. A. L. Johnson, J. D. Brown, N. A. El-Masry, J. W. Cook Jr., J. F. Schetzina, H. S. Kong, and J. A. Edmond, J. Vac. Sci. Technol. B, **16**, 1282 (1998).
- ¹⁶ K. Iwata, H. Asahi, K. Asami, R. Kuroiwa, and S. Gonda, Jap. J. Appl. Phys. part 2, **36**, L661 (1997).
- ¹⁷ S. Nakamura, T. Mukai, and M. Senoh, Appl. Phys. Lett. **64**, 1687 (1994).

- ¹⁸ B. N. Sverdlov, G. A. Martin, H. Morkoc, and D. J. Smith, *Appl. Phys. Lett.* **67**, 2063 (1995).
- ¹⁹ D. J. Smith, D. Chandrasekhar, B. Sverdlov, A. Botchkarev, A. Salvador, and H. Morkoc, *Appl. Phys. Lett.* **67**, 1830 (1995).
- ²⁰ T. Matsuoka, N. Yoshimoto, T. Sasake and A. Katsui, *J. Electron. Mater.* **21**, 157 (1992).
- ²¹ J. Narayan, K. Dovidenko, A. K. Sharma, and S. Oktyabrsky, *J. Appl. Phys.* **84**, 2597 (1998).
- ²² R. D. Vispute, V. Talyansky, S. Choopun, R. P. Sharma, T. Venkatesan, M. He, X. Tang, J. B. Halpern, M. G. Spencer, Y. X. Li, L. G. Salamanca-Riba, A. A. Iliadis, and K. A. Jones. *Appl. Phys. Lett.* **73**, 348 (1998).
- ²³ T. Detchprohm, K. Hiramatsu, H. Amano, and I. Akasaki, *Appl. Phys. Lett.* **61**, 2688 (1992).
- ²⁴ T. Detchprohm, H. Amano, K. Hiramatsu, and I. Akasaki, *J. Crystal Growth*, **128**, 384 (1993).
- ²⁵ R. J. Molnar, P. Maki, R. Aggarwal, Z. L. Liao, E. R. Brown, I. Melngailis, W. Gotz, L. T. Romano, and N. M. Johnson, *Mat. Res. Soc. Symp. Proc. Vol 423*, (MRS, 1996), p. 221.
- ²⁶ L. T. Romano, B. S. Krusor and R. J. Molnar, *Appl. Phys. Lett.* **71**, 2283 (1997).
- ²⁷ X. W. Sun, R. F. Xiao, and H. S. Kwok, *J. App. Phys.* **84**, 5776 (1998).
- ²⁸ R. F. Xiao, H. B. Liao, N. Cue, X. W. Sun, and H. S. Kwok, *J. App. Phys.* **80**, 4226 (1996)
- ²⁹ F. A. Kroger, and H. J. Vink, *Solid State Physics*, **3**, 307 (1956).
- ³⁰ V. A. Nikitenko, S. V. Mukhin, S. P. Pivneva, and I. P. Kuzmina, *Inorganic Materials*, **29**, 1253 (1993).
- ³¹ F. A. Kroger, *The Chemistry of Imperfect Solids*, (North Holland Pub., Amsterdam, 1974).
- ³² E. R. Hutson, *Phys. Rev.*, **108**, 222 (1957).
- ³³ S. E. Harrison, *Phys. Rev.*, **93**, 52 (1954).
- ³⁴ D. G. Thomas, *J. Phys. and Chem. of Solids*, **3**, 229 (1957).
- ³⁵ K. I. Hagemark, *J. Sol. State Chem.*, **16**, 293 (1976).

- ³⁶ W. Hirshwald, in *Current Topics in Materials Science*, Vol. 7, E. Kaldis, editor, (North-Holland, Amsterdam, 1981).
- ³⁷ G. Heiland, E. Mollwo, and F. Stockmann, in *Solid State Physics*, F. Seitz, and D. Turnbull, editors, Vol. 8, 254 (1959).
- ³⁸ V. A. Nikitenko, A. I. Tereshchenko, V. P. Kucheruk, *Inorganic Materials*, **25**, 1425 (1989).
- ³⁹ V. A. Nikitenko, S. V. Mukhin, I. P. Kusmina, and V. G. Galstyan, *Inorganic Materials*, **30**, 963 (1994).
- ⁴⁰ J. J. Lander, *J. Phys. and Chem. Solids*, **15**, 324 (1960).
- ⁴¹ V. M. Basin, A. V. Petrov, G. B. Pranyavichene, and D. Yu. Eidukas, *Sov. Phys. Acoust.* **30**, 160 (1984).
- ⁴² K. Minegishi, Y. Koiwai, Y. Kikuchi, K. Yano, M. Kasuga, and A. Shimizu, *Jap. J. App. Phys. part 2*, **36**, L1453 (1997)
- ⁴³ G. E. Jellison, Jr. And L. A. Boatner, *Phys. Rev. B*. **58**, 3586 (1998).
- ⁴⁴ M.-S. Wu, A. Azuma, T. Shiosake, and A. Kawabata, *J. Appl. Phys.* **62**, 2482 (1987).
- ⁴⁵ S. Dutta, H. E. Jackson, J. T. Boyd, F. S. Hickernell, and R. L. Davis, *Appl. Phys. Lett.* **39**, 206 (1981).
- ⁴⁶ F. S. Hickernell, in *II Int. Symp. on Surface Waves in Solids and Layered Structures*, M. Borissov, L. Spassov, Z. Georgiev, and I. Avramov, editors, (World Scientific, NJ, U.S.A, 1990), p. 42.
- ⁴⁷ C. S. Tsai, *IEEE Trans. Ultrasonics Ferroelectrics and Frequency Control*, **39**, 529 (1992).
- ⁴⁸ M. S. Wu, A. Azuma, T. Shiosake, A. Kawabata, *IEEE Trans. Ultrasonics Ferroelectrics and Frequency Control*, **36**, 442 (1989).
- ⁴⁹ H. Schmidt, M. Weihnacht, and R. Wobst, *1995 IEEE Ultrasonics Symposium*, (IEEE, NJ, 1995), p. 847.
- ⁵⁰ A. M. Matteo, V. M. N. Passaro, and M. N. Armenise, *IEEE Trans. Ultrasonics Ferroelectrics and Frequency Control*, **43**, 270 (1996).
- ⁵¹ M. Wraback, H. Shen, S. Liang, C. R. Gorla, and Y. Lu, to appear in *Appl. Phys. Lett.*
- ⁵² D. C. Reynolds, D. C. Look, and B. Jogal, *Solid State Commun.* **99**, 873 (1996).

- ⁵³ D. M. Bagnall, Y. F. Chen, Z. Zhu, T. Yao, S. Koyama, M. Y. Shen, and T. Goto, *Appl. Phys. Lett.* **70**, 2230 (1997).
- ⁵⁴ D. M. Bagnall, Y. F. Chen, Z. Zhu, T. Yao, M. Y. Shen, and T. Goto, *Appl. Phys. Lett.* **73**, 1038 (1998).
- ⁵⁵ P. Zu, Z. K. Tang, G. K. L. Wong, M. Kawasaki, A. Ohtomo, H. Koinuma, and Y. Segawa, *Solid State Commun.* **103**, 459 (1997).
- ⁵⁶ C. Klingshim, *Phys. Status Solidi B*, **71**, 547 (1975).
- ⁵⁷ T. Ikeda, *Fundamentals of piezoelectricity*, Oxford University Press, London, 1996.
- ⁵⁸ R. M. White, *Proceedings of the IEEE*, **58**, 1238 (1970).
- ⁵⁹ Lord Rayleigh, *Proc. London Math. Soc.*, **17**, 4 (1885)
- ⁶⁰ B. A. Auld, *Acoustic fields and waves in solids, Vol. 2, 2nd Edition*, (Krieger Publishing Co., Florida, 1990).
- ⁶¹ W. P. Mason, *Physical Acoustics and the properties of solids* (Van Nostrnad, New York, 1958).
- ⁶² IEEE Standard on Piezoelectricity, ANSI/IEEE Std. 176-1987; also published in *IEEE Trans. on Ultrasonics, Ferroelectrics and Frequency Control*, **43(5)**, 1996.
- ⁶³ J. J. Campbell and W. R. Jones, *IEEE Trans. Sonics Ultrasonics*, **SU-15**, 209 (1968).
- ⁶⁴ M. Kadota, and M. Minakata, *IEEE Trans. Ultrasonics, Ferroelectrics, and Frequency Control*, **42**, 345 (1995).
- ⁶⁵ N. W. Emanetoglu, S. Liang, C. Gorla, Y. Lu, S. Jen, and R. Subramanian, *Proc. 1997 IEEE Ultrasonics Symp.*, (IEEE, New Jersey, 1997), p. 195.
- ⁶⁶ Y. Kim, W. D. Hunt, F. S. Hickernell, R. J. Higgins, and G.-K. Jen, *IEEE Trans. Ultrasonics, Ferroelectrics, and Frequency Control*, **42**, 351 (1995).
- ⁶⁷ S. J. Chang, Y. K. Su, and Y. P. Shei, *J. Vac. Sci. Technol. A*, **13**, 385 (1995).
- ⁶⁸ N. F. Foster, and S. A. Rozgonyi, *Appl. Phys. Lett.* **8**, 221 (1966).
- ⁶⁹ J. D. Larson, D. K. Winslow, and L. T. Zitelli, *IEEE Trans. Sonics Ultrason.* **SU-19**, 18 (1972).
- ⁷⁰ K. M. Lakin, G. R. Kline, R. S. Ketchum, A.R. Landin, W.A. Burkland, K.T. McCarron S.D. Braymen, and S.G. Burns, 1987 Int. Frequency Control Symp. (IEEE, NJ, 1987), p. 371.
- ⁷¹ S. V. Krishnaswamy, *IEEE MTT-S Newsletter*, p. 21, Fall 1991.

- ⁷² G. W. Farnell, and E. L. Adler, in *Physical Acoustics*, Vol. IX, W. P. Mason, and R. N. Thurston, editors, (Academic Press, NY, 1972), p. 35.
- ⁷³ K. Sezawa, Bull. Earthquake Res. Inst. **3**, 1 (1927).
- ⁷⁴ G. A. Armstrong, Electronics Letters, **9**, 322 (1973).
- ⁷⁵ J. K. Elliott, R. L. Gunshor, R. F. Pierret, and A. R. Day, Appl. Phys. Lett. **32**, 515 (1978).
- ⁷⁶ J. E. Bowers, B. T. Khuri-Yakub, and G. S. Kino, Appl. Phys. Lett, **36**, 806 (1980).
- ⁷⁷ H. Ieki, H. Tanaka, J. Koike, and T. Nishikawa, 1996 IEEE MTT-S Digest, (IEEE, NJ, 1996), p. 409.
- ⁷⁸ T. Mitsuyu, S. Ono, and K. Wasa, J. Appl. Phys. **51**, 2464 (1980).
- ⁷⁹ H. Nakahata, A. Hachigo, S. Shikata, and N. Fujimori, 1992 Ultrason. Symp. (IEEE, NJ 1992), p. 377.
- ⁸⁰ F. S. Hickernell, IEEE Trans. Sonics and Ultrasonics, **SU-32**, 621 (1985).
- ⁸¹ V. I. Anisimkin, and I. M. Kotelyanskii, Sov. Tech. Phys. Lett, **12**, 75 (1985).
- ⁸² V. I. Anisimkin, and I. M. Kotelyanskii, Sov. Phys. Solid State, **30**, 492 (1988).
- ⁸³ V. Craciun, J. Elders, J. G. E. Gardeniers, and I. W. Boyd, Appl. Phys. Lett. **65**, 2963 (1995).
- ⁸⁴ A. Suzuki, T. Matsushita, N. Wada, Y. Sakamoto, and M. Okuda, Jpn. J. Appl. Phys. part 2, **35**, L56 (1996).
- ⁸⁵ S. Hayamizu, H. Tabata, H. Tanaka, and T. Kawai, J. Appl. Phys. **80**, 787 (1996).
- ⁸⁶ V. Srikanth, V. Sergo, and D. R. Clarke, J. Am. Ceram. Soc. **78**, 1931 (1995).
- ⁸⁷ G. L. Dybwad, J. Appl. Phys. **42**, 5192 (1971).
- ⁸⁸ N. Fujimura, T. Nishihara, S. Goto, J. Zu, and T. Ito, J. Crystal Growth, **130**, 269 (1993).
- ⁸⁹ M. Kodata, Jpn. J. Appl. Phys. part 1, **36**, 3076 (1997).
- ⁹⁰ M. Kodata, and M. Minakata, Jpn. J. App. Phys. part 1, **37**, 2923 (1998).
- ⁹¹ K. Tominaga, M. Kume, T. Yuasa, and O. Tada, Jpn. J. App. Phys. **24**, 35 (1985).
- ⁹² J. G. Noltes in, *Zinc Chemicals*, M. Fornsworth and C. H. Kline, Editors, Zinc Institute Inc, New York, 1973.
- ⁹³ M. H. Abraham, J. Chem. Soc. 4130 (1960).
- ⁹⁴ M. A. Rueter, and J. M. Vohs, J. Vac. Sci. Technol. A, **9**, 2916 (1991).

- ⁹⁵ M. A. Rueter, and J. M. Vohs, *Surface Science*, **262**, 42 (1992).
- ⁹⁶ A. P. Roth, and D. F. Williams, *J. Electrochem. Soc.* **128**, 2784 (1981).
- ⁹⁷ C. K. Lau, S. K. Tikku, and K. M. Lakin, *J. Electrochem. Soc.* **127**, 18443 (1980).
- ⁹⁸ S. K. Ghandhi, R. J. Field, and J. R. Shealy, *Appl. Phys. Lett.* **37**, 449 (1980).
- ⁹⁹ K. Tabuchi, W. W. Wenas, A. Yamada, M. Konagai, and K. Takahashi, *Jpn. J. Appl. Phys. part 1*, **32**, 3764 (1993).
- ¹⁰⁰ P. J. Wright, R. J. M. Griffiths, and B. Cockayne, *J. Crystal Growth*, **66**, 26 (1984).
- ¹⁰¹ J. Auld, D. J. Houlton, A. C. Jones, S. A. Rushworth, M. A. Malik, P. O'Brien, and G. W. Critchlow, *J. Mater. Chem.*, **4**, 1249 (1994).
- ¹⁰² R. Solanki, and G. J. Collins, *Appl. Phys. Lett.* **42**, 662 (1983).
- ¹⁰³ M. Shimizu, A. Monma, T. Shiosake, and A. Kawabata, *J. Crystal Growth*, **94**, 895 (1989).
- ¹⁰⁴ M. Shimizu, T. Katayama, Y. Tanaka, T. Shiosaki, and A. Kawabata, *J. Crystal Growth*, **101**, 171 (1990).
- ¹⁰⁵ W. G. Breiland, and G. H. Evans, *J. Electrochem. Soc.*, **138**, 1806 (1991).
- ¹⁰⁶ C. R. Biber, C. A. Wang, and S. Motakef, *J. Cryst. Growth.*, **123**, 545 (1992).
- ¹⁰⁷ D. L. Smith, *Thin-Film Deposition: Principles and Practice*, (McGraw Hill, NY, 1995).
- ¹⁰⁸ R.S. Wagner. In *Whisker Technology*, edited by A.P. Levitt (Wiley Interscience, New York, 1970).
- ¹⁰⁹ *Highly Anisotropic Crystals* by E.I. Givargizov, D. Reidel (Publishing Company, Boston, 1986).
- ¹¹⁰ P. Kung, C. J. Sun, A. Saxler, H. Ohsato, and M. Razeghi, *J. Appl. Phys.* **75**, 4515 (1994).
- ¹¹¹ J. Koike, K. Shimoe, and H. Ieki, *Jpn. J. Appl. Phys. part 1*, **32**, 2337 (1993).
- ¹¹² T. Mitsuyu, S. Ono, and K. Wasa, *J. Appl. Phys.* **51**, 2464 (1980).
- ¹¹³ K. Shindo, A. Morita, and H. Kamimura, *J. Phys. Soc. Japan*, **20**, 2054 (1965).
- ¹¹⁴ J. E. Rowe, M. Cardona, and F. H. Pollak, *Solid State Commun.* **6**, 239 (1968).
- ¹¹⁵ U. Rossler, *Phys. Rev.* **184**, 733 (1969).
- ¹¹⁶ G. F. Koster, J. O. Dimmock, R. G. Wheeler, and H. Statz, *Properties of thirty-two point groups* (MIT Press, Cambridge, U.S.A. 1963).

- ¹¹⁷ J. J. Hopfield, *J. Phys. Chem. Solids* **15**, 97 (1960).
- ¹¹⁸ A. Mang, K. Reimann, and St. Rubenacke, *Solid State Commun.* **94**, 251 (1995).
- ¹¹⁹ K. Hummer, *Physica Status Solidi B*, **56**, 249 (1973).
- ¹²⁰ W.Y. Liang and A.D. Yoffe, *Physical Review Letters*, **20**, 59 (1968).
- ¹²¹ E. Tomzig, and R. Helbig, *J. Luminescence*, **14**, 403 (1976).
- ¹²² D. K. Kolb, and H.-J. Schulz, in *Current Topics in Materials Science*, Vol. 7, E. Kaldis, editor, (North-Holland, Amsterdam, 1981), p. 226.
- ¹²³ S. Takata, T. Minami and H. Nanto, *Jpn. J. Appl. Phys.* **20**, 1759 (1981).
- ¹²⁴ S. Tanaka, K. Takahashi, T. Sekiguchi, K. Sumino, and J. Tanaka, *J. Appl. Phys.* **77**, 4021 (1995).
- ¹²⁵ T. Sekiguchi, N. Ohashi, and Y. Terada, *Jap. J. Appl. Phys*, part 2, **36**, L289 (1997).
- ¹²⁶ M. A. L. Johnson, S. Fujita, W. H. Rowland, Jr., W. C. Huges, J. W. Cook, Jr., and J. F. Schetzina, *Journal of Electronic Materials*, **25**, 855 (1996).
- ¹²⁷ F. Hamdani, A. E. Botchkarev, H. Tang, W. Kim, and H. Morkoc, *Appl. Phys. Lett.* **71**, 3111 (1997.)
- ¹²⁸ C. Wagner, *Z. Anorg. Alg. Chem.*, **236**, 320 (1938).
- ¹²⁹ H. Schmalzried, *Chemical Kinetics of Solids*, (VCH Publishers, NY 1995).
- ¹³⁰ P.G. Kotula, M.T. Johnson, and C.B. Carter, *Z. Fur Physik. Chemie*, **206**, 73 (1998).
- ¹³¹ H. Sieber, D. Hesse, X. Pan, St. Senz, and J. Heydenreich, *Z. Anorg. Allg. Chem.* **622**, 1658 (1996).
- ¹³² K. Nagata, R. Nishiwaki, Y. Nakamura, and T. Maruyama, *Solid State Ionics*, **49**, 161 (1991).
- ¹³³ H. Sieber, P. Werner, D. Hesse, *Philosophical Magazine A*, **75**, 909 (1997).
- ¹³⁴ D. Hesse, P. Werner, R. Mattheis, J. Heydenreich, *Appl. Phys. A*, **57**, 415 (1993)
- ¹³⁵ H. Sieber, D. Hesse, and P. Werner, *Philosophical Magazine A*, **75**, 889 (1997).
- ¹³⁶ C.A. Duckwitz, and H. Schmalzried, *Z. Fur Physik. Chemie Neue Folge*, **76**, 173 (1971).
- ¹³⁷ J.M.F. Colinas, and C.O. Arean, *J. Solid State Chemistry*, **109**, 43 (1994).
- ¹³⁸ J. Frenkel, *Z. Phys.*, **35**, 652 (1926).
- ¹³⁹ C. Wagner, and W. Schottky, *Z. Phys. Chem. (B)*, **11**, 163 (1930).
- ¹⁴⁰ R. E. Howard, and A. B. Lidiard, *Rep. Prog. Phys.*, **27**, 161 (1964).

¹⁴¹ *Atom Movements: Diffusion and Mass Transport in Solids*, by J. Philibert, (Les Editions de Physique, France, 1991).

¹⁴² D. M. Pozar, *Microwave Engineering*, (John Wiley & Sons, New York, 1998).

¹⁴³ R. Anderson, *S-Parameter Techniques*, *Hewlett Packard Test and Measurement Application Note 95-1*, (HP, California, 1997).

cuu duong than cong . com

CURRICULUM VITA

CHANDRASEKHAR R. GORLA

Education

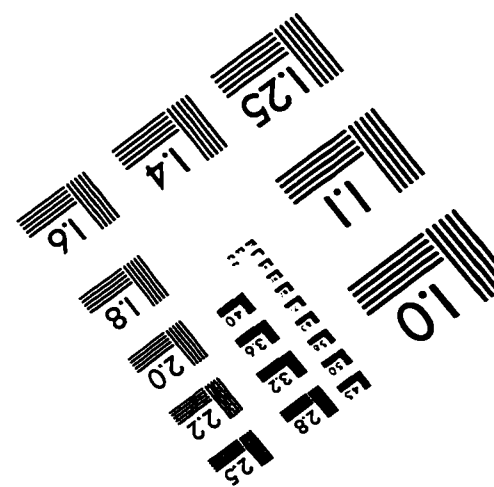
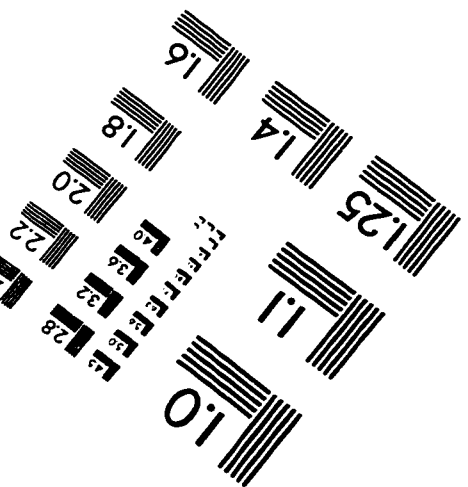
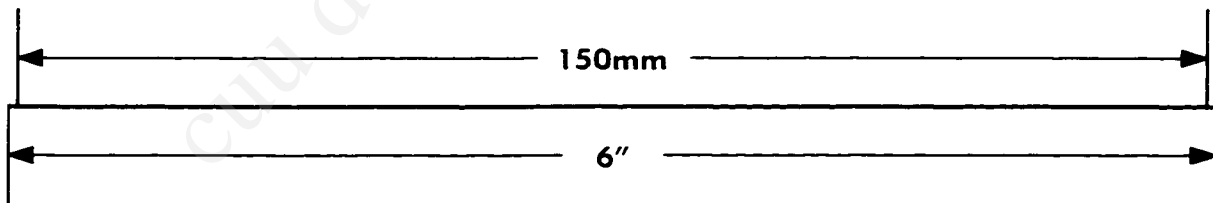
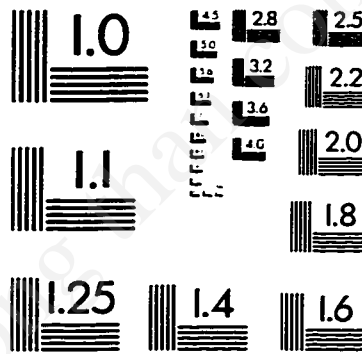
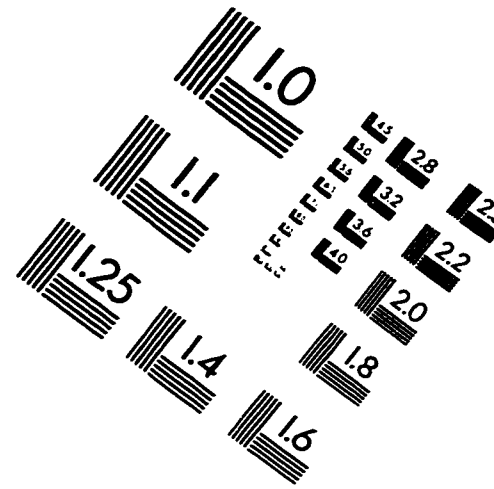
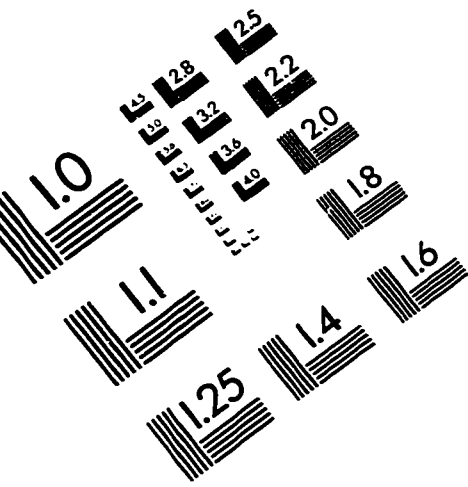
June 1992	Bachelor of Technology in Metallurgical Engineering Indian Institute of Technology, Madras, India.
January 1996	Master of Science in Materials Science and Engineering Rutgers University, New Brunswick, New Jersey
January 1999	Doctor of Philosophy in Materials Science and Engineering Rutgers University, New Brunswick, New Jersey

Publications

1. C. R. Gorla, S. Liang, W. E. Mayo, Y. Lu, M. Wraback, and H. Shen, *Structural, Optical, and Surface Acoustic Wave properties of epitaxial ZnO films grown on (01 $\bar{1}$ 2) sapphire by Metal Organic Chemical Vapor Deposition*, to appear in the February 15th issue of Journal of Applied Physics.
2. C. R. Gorla, S. Liang, Y. Lu, W. E. Mayo, *Reaction kinetics and structure of ZnAl₂O₄ formed at the (11 $\bar{2}$ 0) ZnO/(01 $\bar{1}$ 2) Al₂O₃ interface*, (submitted to Journal of Applied Physics).
3. S. Liang, C. R. Gorla, N. Emanetoglu, Y. Liu, W. E. Mayo, and Y. Lu, *Epitaxial growth of (11 $\bar{2}$ 0) ZnO on (01 $\bar{1}$ 2) Al₂O₃ by metalorganic chemical vapor deposition*, 27, L72 (1998).
4. C. R. Gorla, S. Liang, G.S. Tompa, W.E. Mayo, and Y. Lu, *Silicon and germanium nanoparticle formation in an inductively coupled plasma reactor*, J. Vac. Sci. Technol. A, 15(3), p. 860, May 1997.
5. C.R. Gorla, S. Liang, N. Emanetoglu, W.E. Mayo, and Y. Lu, *Microstructural evaluation of ZnO thin films deposited by MOCVD*, in "Nitride Semiconductors" edited by F.A. Ponce, MRS Fall 1997 Proceedings, Volume 482, p.131-136.

6. N. W. Emanetoglu, S. Liang, C. Gorla, Y. Lu, S. Jen, and R. Subramanian, *Epitaxial Growth and Characterization of High Quality ZnO Films for Surface Acoustic Wave Applications*, Proc. 1997 IEEE Ultrasonics Symposium, p. 195, (1997).
7. M. Wraback, H. Shen, S. Liang, C. R. Gorla, and Y. Lu, *A High Contrast, Ultrafast Optically Addressed Ultraviolet Light Modulator Based Upon Optical Anisotropy in ZnO Films Grown on R-plane Sapphire*, to appear in Applied Physics Letters.
8. N. W. Emanetoglu, C. R. Gorla, Y. Liu, S. Liang, W. E. Mayo, and Y. Lu, *Epitaxial ZnO piezoelectric thin films for SAW filters*, submitted to Solid State Electronics, October 1998.
9. N. W. Emanetoglu, C. R. Gorla, S. Liang, Y. Lu, W. E. Mayo, and Kosinski, *Growth and SAW properties of epitaxial ZnO thin films*, Proc. 1998 IEEE Int. Freq. Control Symp., May 1998, to be published.
10. Y. Li, G. S. Tompa, S. Liang, C. R. Gorla, Y. Lu, and J. Doyle, *Transparent and conductive Ga-doped ZnO films grown by low pressure metal organic chemical vapor deposition*, JVST A, 15(3), p. 1068, May 1997.

IMAGE EVALUATION TEST TARGET (QA-3)



APPLIED IMAGE, Inc.
1653 East Main Street
Rochester, NY 14609 USA
Phone: 716/482-0300
Fax: 716/288-5989

© 1993, Applied Image, Inc., All Rights Reserved